Monthly Notices of the ROYAL ASTRONOMICAL SOCIETY

MNRAS **526,** 5220–5248 (2023) https://doi.org/10.1093/mnras/stad3106
Advance Access publication 2023 October 12

NLTE spectra of kilonovae

Quentin Pognan [1]★ Jon Grumer [2] Anders Jerkstrand[1] and Shinya Wanajo [3]

[1]*The Oskar Klein Centre, Department of Astronomy, Stockholm University, AlbaNova, SE-10691 Stockholm, Sweden*
[2]*Theoretical Astrophysics, Department of Physics and Astronomy, Uppsala University, Box 516, SE-751 20 Uppsala, Sweden*
[3]*Max-Planck-Institut für Gravitationsphysik (Albert-Einstein-Institut), Am Mühlenberg 1, D-14476 Potsdam-Golm, Germany*

Accepted 2023 October 6. Received 2023 October 6; in original form 2023 July 26

ABSTRACT

The electromagnetic transient following a binary neutron star merger is known as a kilonova (KN). Owing to rapid expansion velocities and small ejecta masses, KNe rapidly transition into the non-local thermodynamic equilibrium (NLTE) regime. In this study, we present synthetic NLTE spectra of KNe from 5 to 20 d after merger using the SUMO spectral synthesis code. We study three homogeneous composition, 1D multizone models with characteristic electron fractions of $Y_e \sim 0.35$, 0.25, and 0.15. We find that emission features in the spectra tend to emerge in windows of reduced line blocking, as the ejecta are still only partially transparent even at 20 d. For the $Y_e \sim 0.35$ (lanthanide-free) ejecta, we find that the neutral and singly ionized species of Rb, Sr, Y, and Zr dominate the spectra, all with good potential for identification. We directly test and confirm an impact of Sr on the 10 000 Å spectral region in lanthanide-free ejecta, but also see that its signatures may be complex. We suggest the Rb I $5p^1$–$5s^1$ 7900 Å transition as a candidate for the $\lambda_0 \sim 7500$–7900 Å P-Cygni feature in AT2017gfo. For the $Y_e \sim 0.25$ and 0.15 compositions, lanthanides are dominant in the spectral formation, in particular Nd, Sm, and Dy. We identify key processes in KN spectral formation, notably that scattering and fluorescence play important roles even up to 20 d after merger, implying that the KN ejecta are not yet optically thin at this time.

Key words: radiative transfer – transients: neutron star mergers.

1 INTRODUCTION

Binary neutron star (BNS) mergers are accepted to produce transients known as kilonovae (KNe), powered by the radioactive decay of heavy elements synthesized by rapid neutron capture (r-process) (Symbalisty & Schramm 1982; Eichler et al. 1989; Li & Paczyński 1998; Freiburghaus, Rosswog & Thielemann 1999; Rosswog et al. 1999; Metzger et al. 2010). The properties of BNS merger ejecta, such as mass, velocity, and composition, have been studied in detail with hydrodynamical simulations and nuclear network calculations (e.g. Rosswog et al. 1999, 2018; Martínez-Pinedo et al. 2007; Metzger et al. 2010; Wanajo et al. 2014). Of particular interest is the question as to whether KNe alone can reproduce the measured r-process solar distribution (see e.g. Lodders, Palme & Gail 2009; Rosswog et al. 2018; Prantzos et al. 2020; Lodders 2021; Nedora et al. 2021). The first, and thus far only complete KN observation, of AT2017gfo (see e.g. Abbott et al. 2017; Margutti & Chornock 2021, for a review), has allowed some initial answers to be given to the question of BNS mergers as the dominant source of r-process elements (Rosswog et al. 2018; Côté et al. 2019; Metzger 2019; Arcones & Thielemann 2023).

In order to conclusively answer this question, positive identification of individual elements and determination their abundance in KN ejecta will have to occur. The first strong candidate identification was that of strontium (Sr), as identified from a photospheric phase P-Cygni line (Watson et al. 2019; Domoto et al. 2021), though a possible contribution from helium (He) has also been suggested for this feature (Perego et al. 2022; Tarumi et al. 2023). Subsequently, plausible signatures have been identified for lanthanum (La) and cerium (Ce) (Domoto et al. 2022), yttrium (Y) (Sneppen & Watson 2023), and tellurium (Te) (Gillanders et al. 2023; Hotokezaka et al. 2023). A comprehensive analysis and review of possible candidate species for various spectral features has been carried out by Gillanders et al. (2021, 2022, 2023). Robust element identification is a difficult challenge due to the complex composition and morphology, extensive but in parts not well-known line lists, and high expansion velocities ($\gtrsim$0.1 c) leading to complex radiative transfer and line blending. Identifying the presence or absence of groups of elements based on properties such as expansion opacity is an also an avenue currently being explored (see e.g. Tanaka & Hotokezaka 2013; Tanvir et al. 2017; Banerjee et al. 2020, 2022; Tanaka et al. 2020; Domoto et al. 2022; Carvajal Gallego et al. 2023; Deprince et al. 2023; Fontes et al. 2023).

Spectral identification of species requires knowledge of the atomic properties of that species, notably its level structure and associated radiative transitions. Recent studies in theoretical atomic data for heavy r-process elements have made great advances in the completeness and accuracy of energy levels and transition probabilities (Einstein *A*-values) (see e.g. Kasen, Badnell & Barnes 2013; Gaigalas et al. 2019; Banerjee et al. 2020; Bromley et al. 2020; Fontes et al. 2020; Gaigalas et al. 2020; Radžiūtė et al. 2020; Carvajal Gallego, Palmeri & Quinet 2021; Domoto et al. 2022; McCann et al. 2022; Rynkun et al. 2022;

★ E-mail: quentin.pognan@astro.su.se

Flörs et al. 2023). These advances, and in particular recent efforts to calibrate theoretical data to experimental values, are extremely useful for the spectral modelling of KNe across all epochs.

Almost all light curve (LC) and spectral modelling so far has been conducted for the early epochs during the photospheric phase (see e.g. Tanaka et al. 2018; Wollaeger et al. 2018; Barnes et al. 2021; Kawaguchi et al. 2021; Domoto et al. 2022; Gillanders et al. 2022; Just et al. 2022; Bulla 2023; Vieira et al. 2023). For the most part, the modelling method used in these studies is almost invariably time-dependent Monte Carlo radiative transfer. Although the 3D aspects of the problem have been addressed and modelled from the outset, these first generation of models rely on an LTE assumption for the gas state, and radiative transfer using expansion opacities with thermal resampling. The recent paper by Shingles et al. (2023) is the first one extending the transfer treatment to include also fluorescence which is found to be important in KNe. One should also be aware that fundamental equations used can vary between LTE models. For example, some codes calculate temperature by balancing heating with cooling (Kasen, Badnell & Barnes 2013; Wollaeger et al. 2018, 2021), while others compute a characteristic radiation field temperature and then equate this to the electron temperature (Tanaka & Hotokezaka 2013; Kawaguchi et al. 2021; Bulla 2023). The results can vary quite dramatically; the reader is referred to the supernova (SN) code comparisons in Blondin et al. (2022) for some illustration.

The KN ejecta transition to the non-local thermodynamic equilibrium (NLTE) regime around ∼5 d after the merger (Hotokezaka et al. 2021, 2022; Pognan, Jerkstrand & Grumer 2022b). In NLTE, the ionization and excitation structure of the ejecta are found by solving rate equations, with many different processes, including non-thermal ionization, thermal collisional excitation, photoexcitation, and recombination, all playing a role. As such, modelling of KNe in this regime requires significantly more atomic data than in the LTE phase, in which only energy levels and A-values are needed. For many of these processes, only sparse r-process data are available so far (e.g. McCann et al. 2022, for electron collision strengths), so modelling such processes relies to a large extent on generic formulae. Detailed radiative transfer is needed to properly account for the effects of photoionization (PI) and photoexcitation (PE), with the latter process leading to scattering and fluorescence. In the low-density, fast moving dynamical ejecta, time-dependent effects on recombination and cooling processes may also play a role (Pognan, Jerkstrand & Grumer 2022a), in addition to the time-dependent thermalization of radioactive decay products (Barnes et al. 2016; Waxman et al. 2018; Kasen & Barnes 2019; Hotokezaka & Nakar 2020). Accurate spectral modelling in this regime represents both a physical and computational challenge, with only a few studies making use of NLTE physics to varying degrees existing so far (Hotokezaka et al. 2021, 2022, 2023; Pognan, Jerkstrand & Grumer 2022a, b; Gillanders et al. 2023; Tarumi et al. 2023).

In this study, we present 1D, NLTE KN spectra calculated by the spectral synthesis code SUMO (Jerkstrand 2011; Jerkstrand et al. 2012), adapted to KN simulations as described in Pognan, Jerkstrand & Grumer (2022a). We compute spectra at 5–20 d post-merger; the first epoch reflecting the results found in Pognan, Jerkstrand & Grumer (2022b), which showed that the bulk of the KN ejecta transition to NLTE conditions around 5 d after merger, and the last one reflecting a plausible final optical/near-infrared (NIR) detectability of future events. We construct three ejecta models with varying compositions using the data of Wanajo et al. (2014), all with the same ejecta mass and density profile. The goal of this study is not to identify which species give rise to which specific features in the observed spectrum of AT2017gfo (between 5 and 10 d), as both the simplified ejecta structure, and insufficient wavelength accuracies of our line lists prevent doing this robustly. Instead, our goal is to identify key processes in post-diffusion phase spectral formation (including information on when an 'optically thin' limit is reached), and key elements that play important overall roles in shaping the emergent spectrum. By this, we provide guidance to the hydrodynamic, nuclear, atomic, and radiative transfer communities for the most important diagnostic aspects of KNe at 5–20 d, and in particular which atoms and ions appear to be the most crucial to obtain better atomic and nuclear data for.

The paper is structured as follows. In Section 2, we present the models employed in this study, including the composition and associated energy deposition. We present the spectral synthesis methodology in Section 3. We investigate the resulting thermodynamic state of the ejecta in Section 4 and emergent spectra in Section 5. In Section 6, we discuss the models in the context of AT2017gfo. We discuss the implications of our findings, and summarize future directions, in Section 7.

2 EJECTA MODELS

We study three uniform composition, spherically symmetric multizone models, characterized by light, intermediate, and heavy r-process elements. The compositions of the models can be found in Fig. 1 and are tabulated in Table A1. Each model has a total ejecta mass of $M_{\rm ej} = 0.05$ M$_\odot$, and a density profile of $\rho \propto v^{-4}$, consistent with bulk ejecta from early-time dynamical ejecta, and later viscosity driven disc wind ejecta (see e.g. Kawaguchi et al. 2021). Homologous expansion $v = r/t$ is assumed. The models consist of five radial zones, with the inner boundary at $v_{\rm min} = 0.05$ c and the outer boundary at $v_{\rm max} = 0.3$ c. The zones are spaced linearly with a uniform velocity width $v_{\rm step} = 0.05$ c. With this set-up, the mass distribution in the model zones is 60, 20, 10, 6, and 4 per cent, from the innermost to outermost zone. The models are placed at a distance of 40 Mpc from the observer in order to simplify comparisons to AT2017gfo, which was measured at this distance (e.g. Abbott et al. 2017; Pian et al. 2017; Smartt et al. 2017; Margutti & Chornock 2021).

Wanajo et al. (2014) present composition and radioactive decay power in various channels, versus time, for different $Y_{\rm e}$ values. Using this data, we generate three compositions, and their associated radioactive decays, from Gaussian $Y_{\rm e}$ distributions described by $\mu_{Y_{\rm e}} = 0.35, 0.25, 0.15$, and $\sigma_{Y_{\rm e}} = 0.04$. By using a small range of $Y_{\rm e}$ values we avoid dependence on specifics, while still staying focused on the characteristic $Y_{\rm e}$ values (see also e.g. Tanaka et al. 2020). These are still essentially 'single-component' compositions, and so will not reproduce the solar r-process residual pattern, or the total composition in individual KNe which simulations indicate contain multiple components with different $Y_{\rm e}$ values. We also consider a fourth model equivalent to the $Y_{\rm e} \sim 0.35$ model, but with strontium (Sr) removed, in order to study its effect in the lanthanide-free ejecta case (Section 5.5).

We limit the composition input to SUMO for each model to 30 elements, as shown in Fig. 1, each with four ionization stages from neutral to triply ionized. The included elements are chosen mainly with respect to their abundance in the model, but also from consideration to cover different parts of the periodic table. For example, the composition with $Y_{\rm e} \sim 0.15$ is the only one to have a significant actinide abundance at 5–20 d, and so we include both thorium (Th) and uranium (U) even though their abundances are quite low (0.13 and 0.15 per cent, respectively). We limit ourselves to stable elements due to the lack of atomic data for heavy elements with only

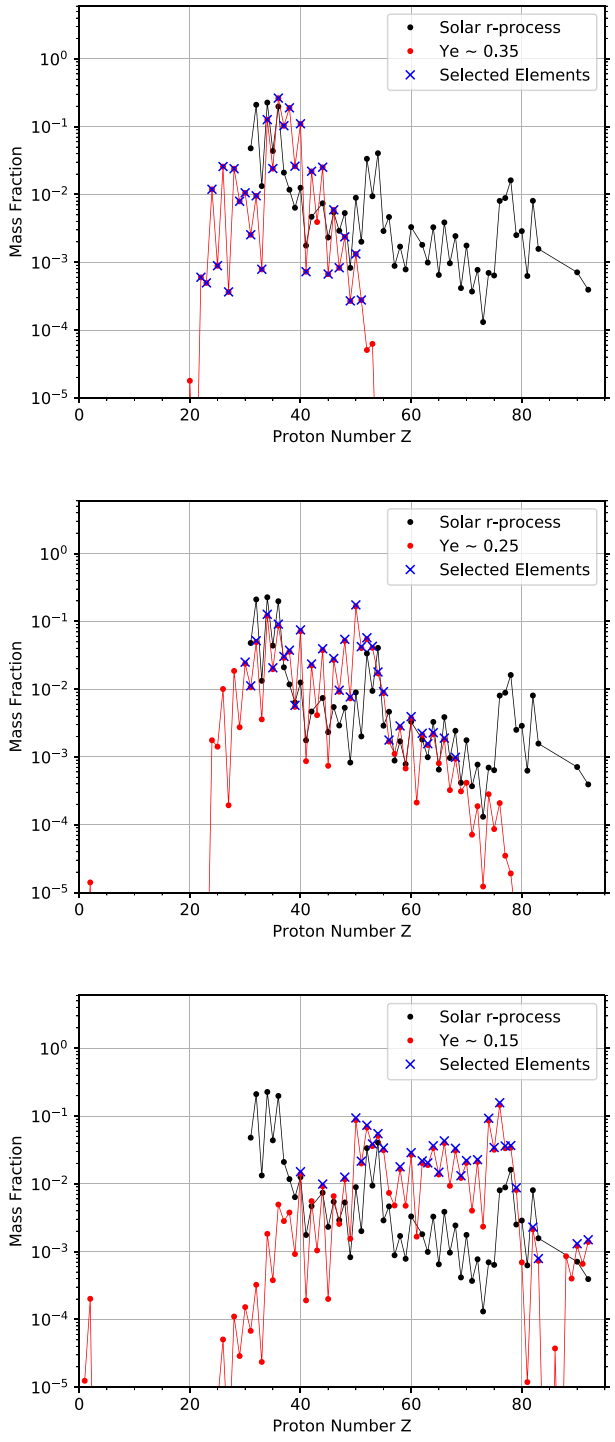

Figure 1. Abundance patterns for the three different Y_e models studied here. The black points represent the normalized solar r-process residual pattern taken from Prantzos et al. (2020). The red points are the outputs resulting from the nuclear network calculations of Wanajo et al. (2014), taken at 10 d after merger, while the blue crosses are the 30 chosen elements by model. Our $Y_e \sim 0.15$ and $Y_e \sim 0.25$ models contain only trans-iron elements, whereas the $Y_e \sim 0.35$ model contains also some lighter elements down to Ti.

unstable isotopes. This omission is expected to only have any impact for our $Y_e \sim 0.15$ model, which synthesizes such heavy elements. In order to avoid changing our model compositions for every epoch, we take the composition of each model to be that of the nuclear network abundance at 10 d, corresponding roughly to the middle of the range of epochs that we study (5–20 d). We note that this does imply a small inconsistency between the energy deposition and the abundances put into SUMO, as the radioactive power is calculated from an evolving composition (Wanajo et al. 2014). However, there is relatively little variation in composition for our models during this time range, so this simplification should not have any significant impact, and certainly much smaller than that arising from uncertainties in the theoretical atomic data, described below. We note that the $Y_e \sim 0.15$ model has 25 per cent of lanthanides by mass fraction, a composition which is too lanthanide-rich to represent the entire KN ejecta. Rather, this composition is more relevant to dynamical ejecta which avoids any neutrino irradiation from disc or remnant winds.

2.1 Atomic data

In order to achieve a consistent and complete set of atomic energy levels and processes, fundamentally bound–bound radiative transitions, for all elements and relevant ions from Fe to U, it is necessary to restrict the complexity of the applied atomic structure method significantly. To this end, in this work, we employ a spectroscopic configuration-interaction (SCI) model where the configuration space is limited to include only those that represent the spectroscopic (physical) states. This can be thought of as a correlation-limited model that only includes the most fundamental many-electron effects beyond the single-configuration Dirac–Hartree–Fock approach, but practically allows for computations of all relevant energy levels and processes in a single calculation for each ion. The accuracy of the data computed with such small-scale ab initio atomic structure models is not good enough for e.g. spectral identifications of individual lines from a given ion, but this approach allows for a statistically complete physical model for each relevant ion in the periodic table.

The SCI calculations were performed with the Flexible Atomic Code (FAC; Gu 2008), which is based on a Dirac–Fock–Slater scheme for the orbital optimizations, and employs a standard Dirac–Coulomb Hamiltonian for the structure calculations. In this work, we also include the Breit interaction in the low-frequency limit and leading quantum-electrodynamical effects (vacuum polarization and electron self-energy). The Dirac–Fock–Slater method works on an average configuration to optimize a common, local central potential. We refer to the code documentation[1] for further details.

The present SCI model includes spectroscopic configurations compiled from comparisons with the NIST Atomic Spectra Database (ASD; Kramida et al. 2020), the Vienna Atomic Line Database (VALD3[2]; Ryabchikova et al. 2015) that, for rare earth elements in particular, includes the data compiled in the Database on Rare Earths at Mons University (DREAM) database (Biémont, Palmeri & Quinet 1999), and with earlier similar works targeting consistent multi-element calculations [most notably the early AUTOSTRUCTURE calculations by Kasen, Badnell & Barnes (2013) and the extensive HULLAC calculations by Tanaka et al. (2018)]. For each ion, we start by optimizing the common central potential on the ground configuration and extend to additional low-energy configurations when deemed necessary to balance screening effects between states of varying subshell structures. This procedure is made possible by comparison to the energy level tables of the NIST ASD. Following

[1]For further information and documentation of the FAC code, consult the open-source GitHub repository: https://github.com/flexible-atomic-code/fac.
[2]VALD is hosted on e.g. http://vald.astro.uu.se/), which contains further information and documentation.

the energy level computations, we remove all states with ab initio energies above the first ionization limit. The remaining set of states is then used in subsequent computations of all relevant radiative bound–bound rates, including allowed electric dipole (E1), and also forbidden magnetic dipole (M1) and electric quadrupole (E2) transitions which, in our investigations, have proved important for the thermodynamic properties of the ejecta. The fundamental parameters defining the model of each ion included in this work are summarized in Table C1.

Following the ab initio calculations described above, the energy levels of Sr II were rescaled to match those found in the NIST data base (Kramida et al. 2020). Since Sr II is a species of key interest in KN modelling due to its claimed detection in previous works (Watson et al. 2019; Domoto et al. 2022), accurate modelling of the spectral features arising from Sr II is of particular importance, specifically the emission and absorption arising from the strong transitions of the 4000 Å doublet, the 6800 Å doublet, and 10 000 Å triplet. In order to do so, six levels from the NIST ASD were added to the theoretical data, bringing the total number up to level 27 when energy ordered, with level 27 corresponding to the highest lying state with available A-value data. The levels were then rescaled to their experimental values, and the transition wavelengths correspondingly adjusted. The theoretical A-values were kept, apart from transitions where NIST A-values were available to a precision of 'B' or better, corresponding to an estimated accuracy of $\leq$10 per cent. We note that the theoretical transition strengths for these were all within an order of magnitude to the values found in NIST, supporting the accuracy of our model atom for Sr II.

The first eight levels of Y I were also rescaled to the values found in the NIST data base (Palmer 1977) in order to improve the wavelength accuracy of low-lying strong transitions found to be important in our models. The higher lying levels above this were not modified. The A-values for Y I were kept to be those of the ab initio calculations as no transition probabilities were found for the relevant transitions from these low-lying states.

3 SPECTRAL SIMULATION METHODS

We use the NLTE spectral synthesis code SUMO (Jerkstrand 2011; Jerkstrand et al. 2012) to generate spectra of KNe in 1D. The majority of the physics used in the code is described in the papers above, and adaptations to KNe in Pognan, Jerkstrand & Grumer (2022a). We summarize here the processes particularly important for this study.

3.1 Energy deposition

The raw radioactive power per unit mass, $\dot{Q}$, for each model is constructed from the relevant weighting of different single Y_e components from the nucleosynthesis calculations of Wanajo et al. (2014), self-consistently with the evolving abundance. The total raw power is a sum of all decay products: neutrinos, α-decay (He nuclei), β-decay (electrons and positrons), γ-decay (gamma-rays), and spontaneous fission (SF) (heavy nuclei). Each of these decay products thermalize differently and depending on the ejecta density as well as the ordering of the magnetic fields. For α, β, and γ-decay, we follow the thermalization prescription of Kasen & Barnes (2019), with additional considerations from Waxman, Ofek & Kushnir (2019) for β-decay. Here, the calculation is conducted for mildly relativistic electrons as opposed to non-relativistic electrons, such that the thermalization efficiency drops off in a steeper manner (see Appendix A), which is found to a better analytical fit to numerical calculations (see e.g. Hotokezaka & Nakar 2020). For spontaneous fission, the formalism of Barnes et al. (2016) is adopted. Neutrinos are assumed to completely escape the ejecta at all times. The details of our thermalization treatment can be found in Appendix A. The thermalization efficiency of charged particles will depend on the geometry of magnetic fields inside the ejecta (Barnes et al. 2016; Waxman, Ofek & Kushnir 2019), and we here assume an arbitrary configuration which gives local particle trapping. The total energy input in a given zone, per unit mass, is given by

$$\dot{q}_{\rm tot}(t) = \sum_i \dot{Q}_i \, f_i(t) \, {\rm erg \, s^{-1} \, g^{-1}}, \quad (1)$$

where the subscript i indicates a decay product and f_i is the corresponding thermalization factor.

The deposited power $\dot{q}_{\rm tot}$ is channelled into heating and ionization by solving the Spencer–Fano equation (Spencer & Fano 1954; Kozma & Fransson 1992) for the cascading of high-energy electrons. By this treatment, we make an assumption that α-particles and fission fragments create a population of high-energy electrons in a similar manner as leptons and gamma-rays. Leptons and atomic nuclei have relatively similar ionization loss rates (Longair 2011), and in addition, the ensuing cascade distribution is almost independent of the initial injection energy, motivating this. Since we currently lack high-energy collisional excitation cross-sections for r-process elements, we do not include non-thermal excitations in the solution. The omission of this channel is expected to have limited impact on the spectral formation, as in the relatively ionized conditions of KN ejecta ($x_e \sim$ 1–2), the vast majority of the energy ($\gtrsim$99 per cent) goes towards heating. The treatment of non-thermal collisional ionization is addressed below in Section 3.3. The energy deposition for each model versus time can be visualized in Fig. A1.

For the $Y_e \sim 0.35$ and $Y_e \sim 0.25$ compositions, β-decay is the only important channel at 5–20 d, whereas for the $Y_e \sim 0.15$ model α-decay and spontaneous fission also contribute, with fission becoming as important as β-decay at 20 d. The total deposition varies quite significantly between the models, e.g. at 10 d it is $\sim 4 \times 10^{39}$ erg s^{-1} in the $Y_e \sim 0.35$ model, 1×10^{40} erg s^{-1} in the $Y_e \sim 0.25$ model, and 2.4×10^{40} erg s^{-1} in the $Y_e \sim 0.15$ model (see Fig. A1).

3.2 Temperature calculation

The temperature in each zone is found from solving the time-dependent first law of thermodynamics, with heating due to radioactivity, free–free absorption, and photoionization, and cooling due to net thermal electron bound–bound deposition (giving line emission), free–free, free–bound, and bound–free (collisional) cooling, and (in time-dependent mode) adiabatic cooling. For $t \leq 10$ d, we use the steady-state approximation instead of solving the full time-dependent equation. The continuum-involving cooling channels are found to be unimportant ($\lesssim$0.1 per cent), while adiabatic cooling may start to play a role for low-density zones at late times, following the results found in Pognan, Jerkstrand & Grumer (2022a).

The evolution of KN temperatures in the post-diffusion phase has previously been studied by Hotokezaka & Nakar (2020) and Pognan, Jerkstrand & Grumer (2022a), who showed that temperatures in the NLTE regime generally increase with time, at least as long as steady-state conditions hold. This is qualitatively different to LTE-model temperatures, in which both thermal balance (e.g. Wollaeger et al. 2018, 2021) and $T_e = T_r$ (e.g. Tanaka & Hotokezaka 2013; Gillanders et al. 2021; Bulla 2023; Collins et al. 2023) approaches typically give monotonic temperature decreases with time.

3.3 Ionization structure

The NLTE ionization structure of the ejecta is calculated by solving the rate equations for each ionization state. The ionization processes considered are non-thermal (NT) collisional ionization, thermal collisional ionization (TI), and photoionization (PI), such that $\Gamma_{\rm tot} = \Gamma_{\rm NT} + \Gamma_{\rm TI} + \Gamma_{\rm PI}$, where thermal collisional ionization has been added for this study. We treat this by the formalism of Shull & van Steenberg (1982):

$$\Gamma_{\rm TI} = 1.3 \times 10^{-8} F \xi I_{\rm ev}^{-2} T^{1/2} \left(1 + a\frac{kT}{I}\right)^{-1} \times \exp\left(-I/kT\right) {\rm cm}^3\ {\rm s}^{-1}, \quad (2)$$

where I is the ionization potential, and we take $F = 1$, $\xi = 1$, and $a = 0.1$ (see Shull & van Steenberg 1982, for a discussion of these parameters). PI and NT ionizations are treated as in Pognan, Jerkstrand & Grumer (2022a). Due to lack of atomic data for these processes, we use a hydrogenic cross-section for PI (Rybicki & Lightman 1979), and the Lotz (1967) formalism for NT cross-sections. We only apply the NT cross-section to the valence shell, as treatment of inner shell ionization requires modelling of Auger processes and X-ray fluorescence not currently included for r-process elements. Though these contributions to ionization should be smaller than that of the valence shell, they may add up to be non-negligible. As such, it is possible that our NT ionization rates are somewhat underestimated.

We find that PI typically dominates ionization rates for neutral and single ionized species, while NT ionization dominates for doubly ionized species. This is largely due to the higher ionization potentials for more highly ionized ions, making PI by the moderate-energy radiation field less effective. Thermal collisional ionization is never found to dominate, consistent with the analytical estimates of Pognan, Jerkstrand & Grumer (2022a).

For recombination, we use a constant recombination rate $\alpha = 10^{-11}$ cm^3 s^{-1}, as in Pognan, Jerkstrand & Grumer (2022a, b). As there is a critical lack of data for total (radiative and dielectronic) rates for r-process elements, the usage of a constant value for recombination is an assumption that was made by comparing known rates of light elements (see appendix C of Pognan, Jerkstrand & Grumer 2022a), alongside a limited calculation for Nd (Hotokezaka et al. 2021). The total recombination rates for Nd for temperatures of $T \gtrsim 10^3$ K relevant to this study were found to be $\alpha \lesssim 5 \times 10^{-10}$ cm^3 s^{-1}, with values decreasing as temperature increases. As such, for the temperatures we find ($T \sim$ 3000–35 000 K), our fiducial rate is typically within an order of magnitude of calculated rates.

Time-dependent effects (steady-state breakdown) may begin to affect the ionization solution when the recombination time, $t_{\rm rec} = 1/(\alpha n_{\rm e})$, becomes a significant fraction of the evolutionary time (Pognan, Jerkstrand & Grumer 2022a). Analytical considerations indicate that the low-density outer ejecta layers may become prone to time-dependent effects at $t \gtrsim 10$ d for our model. As such, we run SUMO in time-dependent mode from 10 d onwards.

3.4 Excitation structure and radiation field

The NLTE excitation structure within the ejecta is calculated by solving the rate equations for ground and excited states. Certain (de)-excitation processes, such as collisional processes and spontaneous radiative de-excitation by allowed channels, will always be faster than the evolutionary time-scale. As such, the excitation structure of the ejecta is always calculated under the steady-state assumption.

Since KNe are expected to mainly cool by spontaneous line emission, thermal collision strengths have a direct impact on the ejecta temperature. The effective collision strength from lower level l to upper level u, $\Upsilon_{l,u}$, is treated differently depending on whether the transition is allowed or forbidden, distinguished by the (dimensionless) oscillator strength $f_{\rm osc}$ (e.g. equation 2.68 of Rutten 2003). Allowed transitions are taken to have $f_{\rm osc} \geq 10^{-3}$, for which the effective collision strength is found using the formula derived by van Regemorter (1962), while forbidden transitions with $f_{\rm osc} < 10^{-3}$ are instead calculated using the formula from Axelrod (1980). Values calculated by this formula typically range between 0.01 and 1 depending on the transition. Both of the above equations are commonly used in NLTE radiative transfer codes (see e.g. Botyánszki & Kasen 2017; Shingles et al. 2020; Hotokezaka et al. 2021), though some KN studies have taken transition strengths for forbidden transitions instead to be fixed (e.g. Hotokezaka et al. 2021).

The radiative transfer used by SUMO is described in great detail in Jerkstrand, Fransson & Kozma (2011) and Jerkstrand et al. (2012), and has not been significantly modified since. We describe here some details particularly relevant for this study. The radiation field is likewise not treated in a time-dependent fashion, but the assumption of $c = \infty$ is made (except for in Doppler shift terms). This steady-state assumption for the radiation field is sometimes called the stationarity approximation. This approximation is formally only valid when the photon transport time is short compared to the evolutionary time, which may not necessarily be the case for KNe in the range of epochs studied here. Quantification of the diffusion phase from theory is difficult as it is influenced by fluorescence which has so far not been included in KN modelling, except for in the recent model presented by Shingles et al. (2023). Diffusion effects in general lead to the emergent bolometric luminosity not tracking the instantaneous energy deposition (after thermalization). As the optical depth of the ejecta drops in post-peak times, the radiation transport time approaches the free-streaming limit $v_{\rm ej}t/c$, extended by path enhancements due to scattering caused by remaining line opacity (see Jerkstrand, Smartt & Heger 2016, for a discussion). The effect of a steady-state radiation field approximation has been previously conducted in the context of Type Ia supernovae (SNe), where it was found that while flux levels are naturally not reproduced over the diffusion phase, the spectrum remains accurate (Kasen, Thomas & Nugent 2006; Shen et al. 2021). We will return to a discussion of possible diffusion effects when comparing our models to AT2017gfo in Section 6.1.

Since our photon packets do not track time, we also do not capture the effects of different traveltimes from last interaction point to the observer. That time-scale is given by $t_{\rm travel} \sim 2v_{\rm ej}t/c$, where $v_{\rm ej}$ is the characteristic ejecta expansion velocity. For our model, the mass-weighted mean velocity is 0.11 c, so $t_{\rm travel} \sim 0.22t$. As long as radioactive power follows the canonical $t^{-1.3}$, power levels change on a time-scale $t_{\rm power} = t/1.3 \approx 0.8t$ (or somewhat shorter if the decreasing thermalization efficiency is also considered). Density changes on the homology time-scale $0.33t$. Thus, $t_{\rm travel} < t_{\rm power}, t_{\rm density}$, though it is not much smaller, so some mild/moderate effects can be expected. This however, mostly pertains to the specific shape of individual line profiles which is not the focus of study here.

Processes like fluorescence and scattering may play important roles in the spectral formation of KN in the 5–20 d period (Shingles et al. 2023). We treat these processes in full detail using the standard SUMO line-by-line transfer method with full fluorescence. This is a hybrid Monte Carlo/ray tracing method, in which packets

can be either fully or partially absorbed depending on the nature of the opacity. Lines are divided into the groups of coupled or uncoupled to the NLTE solutions, with an adjustable cut-off for each ion. Here, we compute all models with all lines fully coupled, such that all are available as (de)excitation channels, therefore allowing all fluorescence and resonance transitions. In these line interactions, photon packets are attenuated upon passing a line, with the corresponding power increasing the PE estimators. Radiative de-excitation following a PE is resonance scattering if it is by the same transition, and fluorescence if by other transitions. For continuum interactions, a random draw determines whether the packet Thomson scatters or not; if not the packet is attenuated by all continuum opacities and the corresponding PI estimators (and PI heating) are updated.

4 THERMODYNAMIC EVOLUTION

The three models, with $Y_e \sim 0.35$, 0.25, and 0.15, respectively, are evolved from 5 to 20 d following the methodology described in Section 3. The models are initially computed with a steady-state approximation for all epochs, and then again from 10 d onwards using the full time-dependent equations for temperature and ionization. We begin by considering the structure of the thermodynamic properties of the ejecta, and the evolution with time. The evolution of temperature and electron fraction (x_e indicating degree of ionization) are shown in Fig. 2, where the solid lines represent the steady-state solutions, and the dashed lines represent the time-dependent solutions (computed from 10 d onwards).

Beginning with the evolution of temperature as shown in the left-side panels of Fig. 2, the zone temperatures increase in each model with time, consistent with calculations from previous studies (Hotokezaka et al. 2021; Pognan, Jerkstrand & Grumer 2022a). From 10 d onwards, we see slightly lower temperatures for the time-dependent solutions than for the steady-state ones, with the effect being more significant for the outer ejecta layers. The effect is maximized at our final epoch of 20 d, where for the outermost layer, we find a temperature drop from ∼9000 K down to ∼8000 K in the $Y_e \sim 0.35$ model, and an adiabatic cooling contribution of ∼4 per cent. This contribution is too small to solely account for a change in temperature of ∼11 per cent, implying that effects arising from an altered ionization solution are also occurring (see below).

Regarding the spatial gradient of temperatures (Fig. B1), at early times the outer layers of the ejecta are systematically hotter than the inner layers, consistent with reduced line cooling efficiency due to lower densities, while thermalization is still largely effective and thus not density dependent. This general trend is not ubiquitous, however, and we see a more complex temperature structure from ∼10 d onwards in the $Y_e \sim 0.35$ and 0.25 models, where the hottest ejecta layer is not always the outermost layer. When thermalization starts to become inefficient, decreasing density leads to a competing effect between reduced thermalization efficiency, which will lower the heating, and reduced line cooling efficiency.

Looking at the ionization structures in the right-side panels of Figs 2 and B1, we see a similar trend as for temperature. There is a stratification, with the inner layers of the ejecta being less ionized than the outer ones, consistent with more efficient recombination at higher densities. For the $Y_e \sim 0.35$ and 0.25 models, the ionization degree in the outer layers approach each other at late times, with the second outermost layer becoming the most ionized one at 20 d. As for temperature, density variation gives a competing effect between ionization and recombination, as lower density will mitigate both processes. In general, the overall ionization state increases with time, just as temperature does. Ultimately, this has its origin in the slower decline of the input power [$\sim t^{-(1.3-2.8)}$] compared to the density evolution ($\sim t^{-3}$).

As for temperature, the $Y_e \sim 0.35$ model experiences significant time-dependent effects in the degree of ionization, the maximal deviation occurring in the outermost layer at our last epoch of 20 d, where the ionization fraction is $x_e \sim 1.8$ compared to the steady-state value of $x_e \sim 2.0$. This change in ionization structure also affects the temperature solution, as different ions have different line-cooling capacities (Pognan, Jerkstrand & Grumer 2022a). The ionization structure 'freezes out' at around 10 d in the outer ejecta layers. This freeze-out effect occurs when the time-scales for both ionization (by all processes), and recombination become comparable to the evolutionary time (Pognan, Jerkstrand & Grumer 2022a).

Comparing the models to each other, we see that the lower the electron fraction Y_e, the hotter and more ionized the ejecta typically are at all epochs. This is consistent with a larger energy deposition, notably in the case of the $Y_e \sim 0.15$ model which also has contributions from α-decay and spontaneous fission, and has a factor 2–5 times more energy deposition than the $Y_e \sim 0.35$ model at every epoch (see Fig. A1). Since the thermalization by decay product is the same for each model (the zone densities are identical), this larger energy deposition arises from the inclusion of α-decay and fission, the products of which thermalize more effectively than β-decay electrons in the 5–20 d range. The gradients of temperature and ionization throughout the ejecta are likewise more significant for the models with heavier compositions and enhanced energy deposition. For example, at 20 d, the innermost layer of the $Y_e \sim 0.15$ model has a temperature of ∼6000 K, while the outermost layer reaches ∼35 000 K. Conversely, the values for the $Y_e \sim 0.35$ model only range from ∼5000 K (inner boundary) to ∼8000 K (outer boundary). The ionization gradient follows the same trend as the temperature gradient, with the $Y_e \sim 0.15$ model having $x_e = 2.3$–2.9 at 20 d and the $\sim Y_e \sim 0.35$ model a significantly lower $x_e = 1.4$–1.8.

5 SPECTRAL FEATURES

In this section, we examine our emergent spectra and determine which species are the main drivers of spectral formation in our models, focusing on the 5, 10, and 20 d epochs, shown in Figs 3, 5, and 7 for the $Y_e \sim 0.35$, 0.25, and 0.15 models, respectively. The colours in the spectra tag the last element with which the photon packet interacted, including by scattering/fluorescence. The spectra have all been smoothed by a Gaussian with a full width at half-maximum velocity of 3500 km s^{-1} in order to reduce Monte Carlo noise. To aid in the analysis, we show the optically thick lines in each model at the aforementioned epochs in Figs 4, 6, and 8. In order to clarify whether emission features arise from cooling (i.e. spontaneous radiative de-excitation following a collisional excitation by a thermal electron), or from processes such as scattering and fluorescence, we show the contribution of key elements to the total cooling compared to their total flux contribution in the emergent spectra in Fig. 9. We note here that the purpose of this section is not to conclusively identify potential features observed in AT2017gfo, but rather to understand which species play key roles in the spectral formation, and which processes are important. We add that every element's contribution to both emission and absorption has been checked, and the species presented in the following section are found to be the most significant in our models.

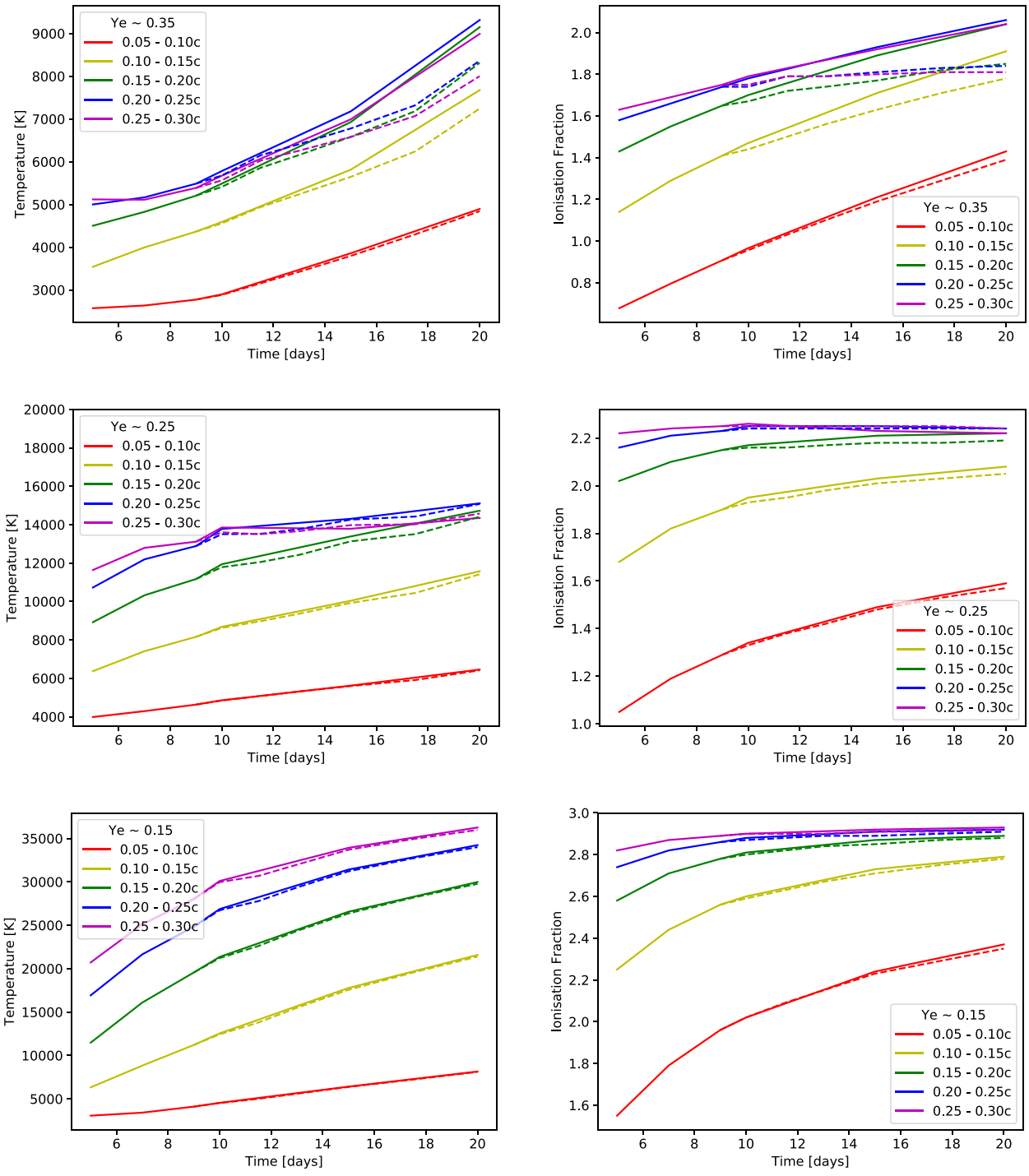

Figure 2. The evolution of temperature (left-hand panels) and ionization degree (electron fraction x_e, right-hand panels) by zone of the models. The solutions with time-dependent ionization and temperature physics are indicated by the dashed lines, steady-state solutions with solid. Note that time-dependent mode is only run from 10 d onwards.

5.1 The $Y_e \sim 0.35$ model

We first take a closer look the key species in the $Y_e \sim 0.35$ model, shown at 5, 10, and 20 d in Fig. 3. We find that the spectral features are dominated by only a few first r-process peak elements from groups I–IV of the periodic table: Rb, Sr, Y, and Zr. These first r-process peak elements are quite abundant in the model composition (see Fig. 1 and Table A1), but their atomic structure also plays an important role in their domination. These elements all have relatively few valence electrons, providing them with strong, allowed transitions between thermally accessible low-lying states, enabling both powerful absorption and emission channels, as was previously found for the neutral and singly ionized species by Domoto et al. (2022).

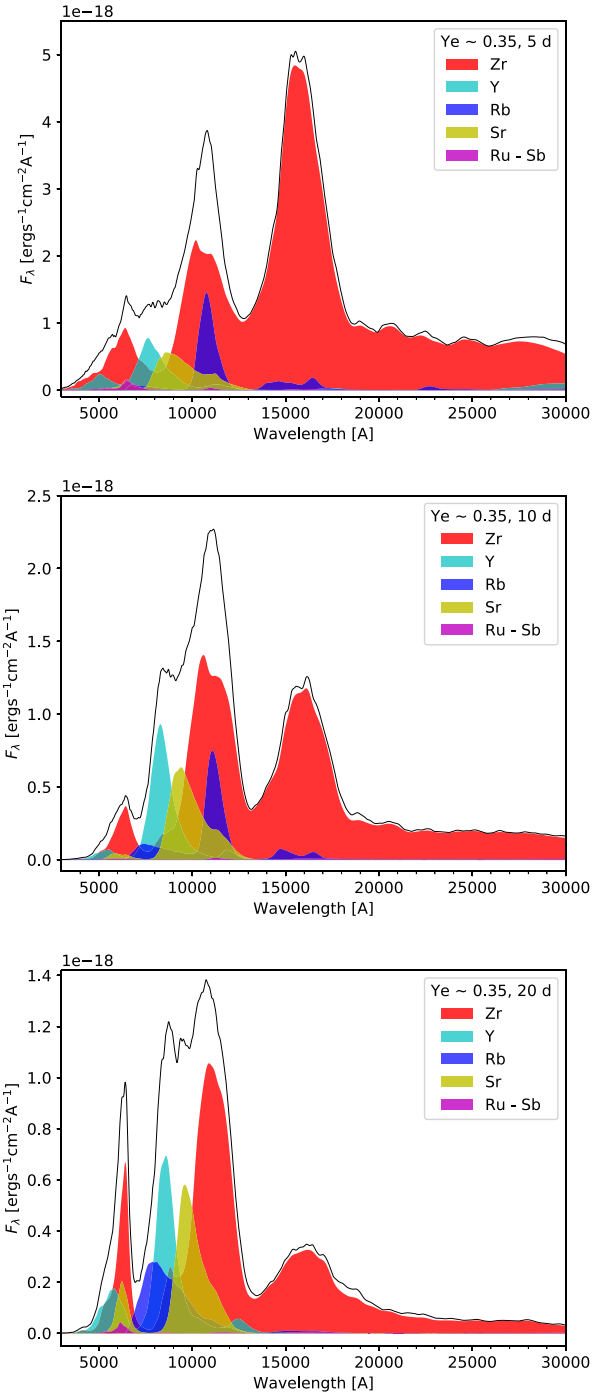

Figure 3. The spectrum of the $Y_e \sim 0.35$ model at 5, 10, and 20 d, with key emitting species marked. The magenta filled area represents total second r-process peak element contribution in this model (Ru–Sb), which is seen to be small.

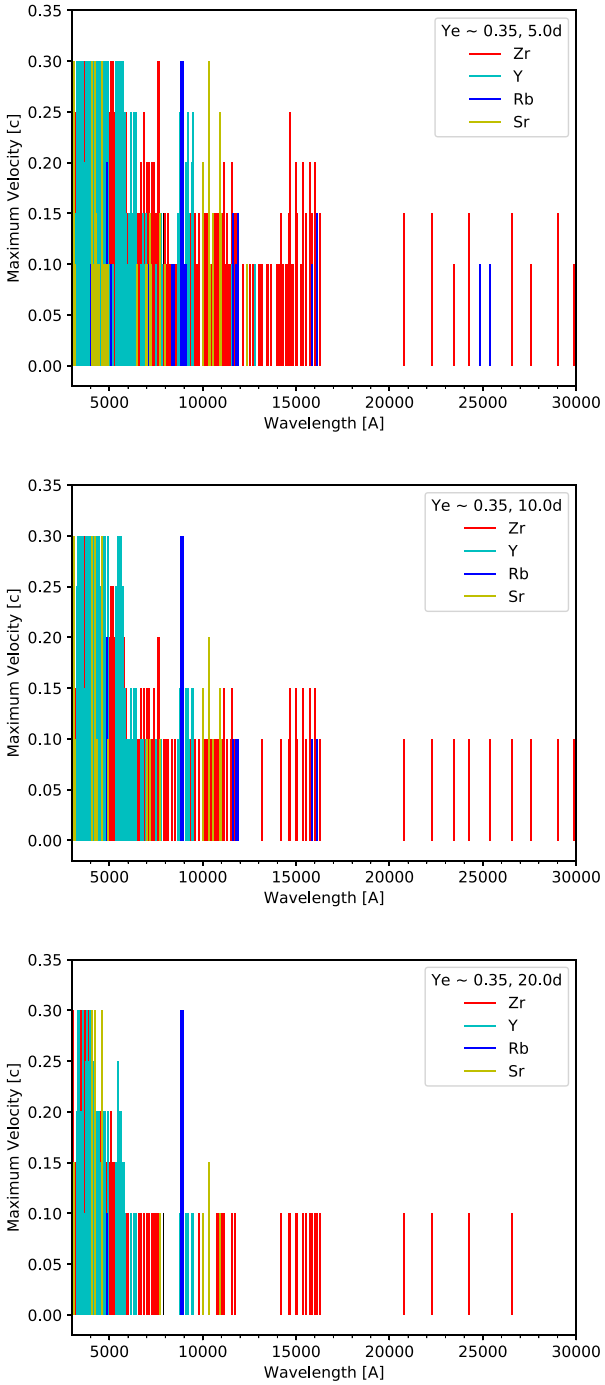

Figure 4. Optically thick lines in the $Y_e \sim 0.35$ model at 5, 10, and 20 d. The velocity up to which the line is optically thick is shown. Line wavelengths are plotted as rest wavelengths. Major contributing elements are marked in colours. Contributions from other elements are also plotted, but are typically minimal compared to the marked elements.

Of particular interest are the Zr I and Zr II ions, which have closely packed low-lying multiplets, all of the same parity (see e.g. Moore 1971; Kramida et al. 2020; Lawler, Schmidt & Hartog 2022). Due to this structure, the transitions between these low-lying states are (semi)-forbidden transitions often with relatively low energies, providing blanket features across the NIR at late times when densities are low enough. However, the first excited states of opposite parity, and therefore with strong allowed transitions, are still well within range of thermal excitation and/or optical/NIR scattering, and so while Zr I and Zr II have many weak NIR transitions, they also possess some strong allowed transitions like Rb–Y. We find domination of Zr I past 1.8 μm, both in terms of emission and absorption.

We find that the Zr emission is mostly from neutral Zr I at early times, with some contribution by Zr II to the ∼6000 Å feature and at ∼1.7 μm at 20 d. The three Zr emission peaks seen in the top panel of Fig. 3 arise from the blending of many allowed transitions,

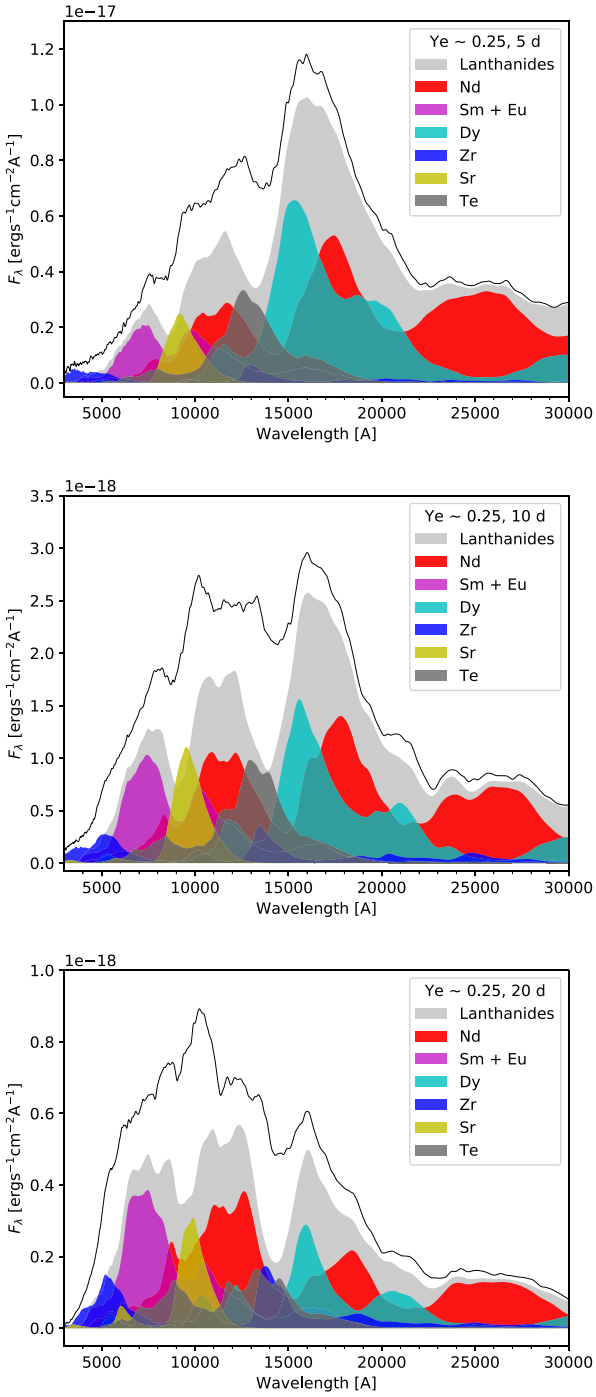

Figure 5. The spectrum of the $Y_e \sim 0.25$ model at 5, 10, and 20 d, with key emitting species marked. The light grey filled area represents the total lanthanide element contribution in this model (note that this also contains also the individually marked lanthanides Nd, Sm, Eu, and Dy).

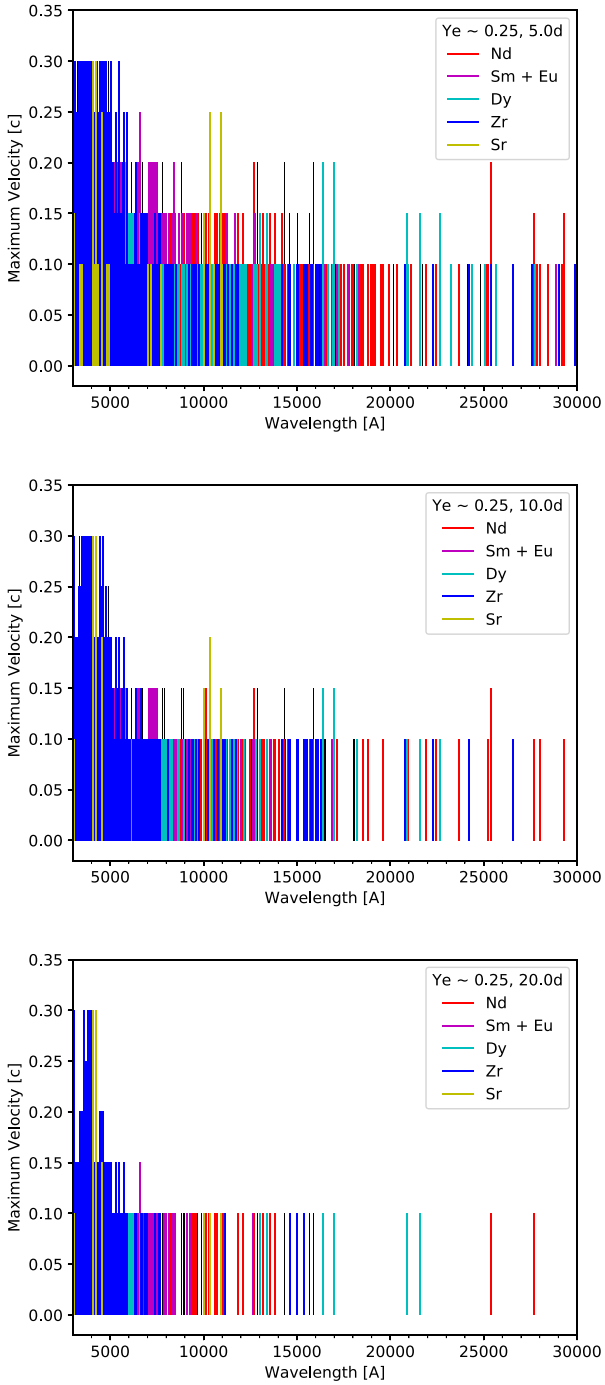

Figure 6. Optically thick lines in the $Y_e \sim 0.25$ model at 5, 10, and 20 d. The velocity up to which the line is optically thick is shown. Line wavelengths are plotted as rest wavelengths. Major contributing elements are marked in colours. Remaining contributions from other elements are also plotted, but are typically minimal compared to the marked elements.

occurring from the higher lying odd parity multiplets down to the many even parity low-lying multiplets. Owing to the closely packed nature of these multiplets, this yields many similar strength lines of similar wavelengths, which were found to play an important role also in the context of photospheric absorption and opacity (Tanaka et al. 2020; Domoto et al. 2022). As such, the widths of the Zr emission features are determined both from velocity broadening as well as line blending. At 5 d, the Zr emission past ∼1.8 μm is due to allowed transitions, with P-Cygni formation arising from the optically thick lines seen in Fig. 4. At 20 d, we no longer see these small absorption features, and the few optically thick lines are only in the innermost ejecta layer. The emission at this epoch is likely a combination of these now optically thin allowed transitions alongside some contribution from the (semi)-forbidden transitions between the lowest lying states.

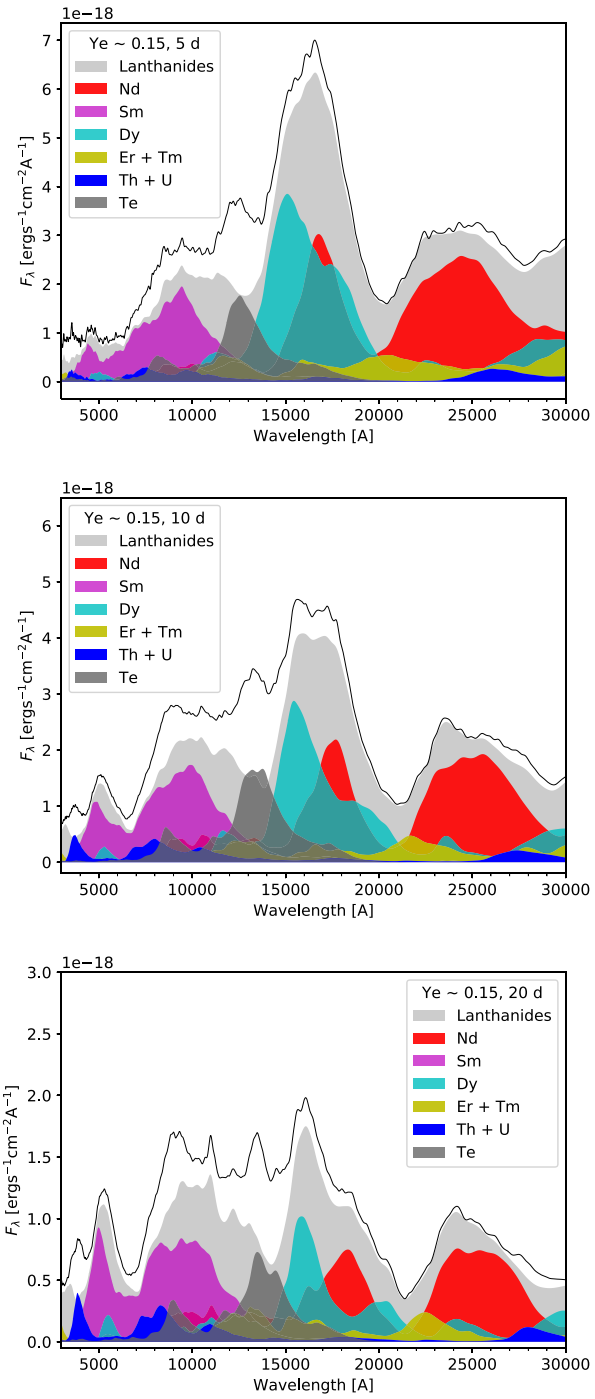

Figure 7. The spectrum of the $Y_e \sim 0.15$ model at 5, 10, and 20 d, with key emitting species marked. The light grey shaded area represents the total lanthanide emission (note that this contains also marked individual lanthanide contributions of Nd, Sm, Dy, Er, Tm), while key individual elements are marked out in colours.

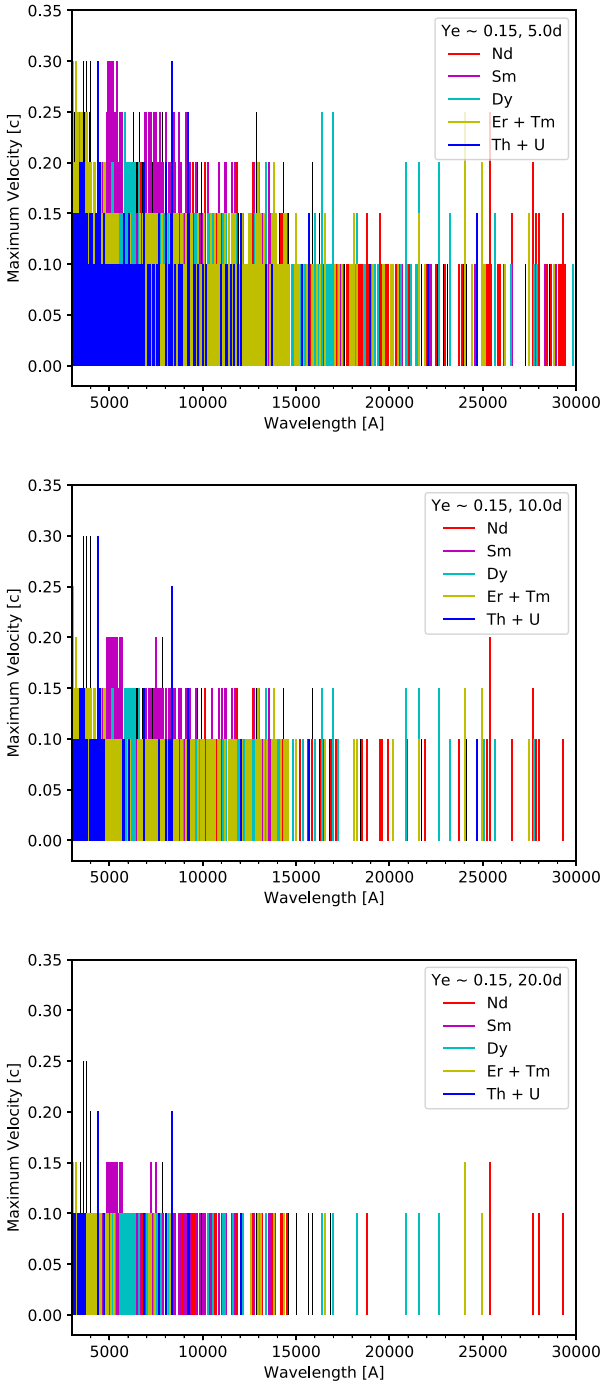

Figure 8. Optically thick lines in the $Y_e \sim 0.15$ model at 5, 10, and 20 d. The velocity up to which the line is optically thick is shown. Line wavelengths are plotted as rest wavelengths. Major contributing elements are marked in colours. Remaining contributions from other elements are also plotted, but are typically minimal compared to the marked elements.

The emission from the other species (Rb, Y, Sr) arises from strong transitions. At all epochs, we see emission from the Sr II triplet around 10 000 Å ($\lambda_0 = 10\,039, 10\,330, 10\,918$ Å), and at 20 d, the appearance of emission also from the ∼6800 Å doublet ($\lambda_0 = 6740, 6870$ Å). We discuss Sr line formation in more detail in Section 5.5.

The Y emission is initially from Y I, with contributions from Y II at later epochs. The persistent emission at ∼8500 Å arises from several strong transitions to the ground doublet from low-lying states in Y I, and is wavelength accurate. The bluer feature at ∼5500 Å arises from a strong transition in Y II between the first opposite parity state and the ground state, but is slightly too red in our model atom and should be located at ∼4400 Å. We note that this feature arises from different transitions than those identified as possibly responsible for a ∼7600 Å P-Cygni feature in AT2017gfo (Sneppen & Watson 2023).

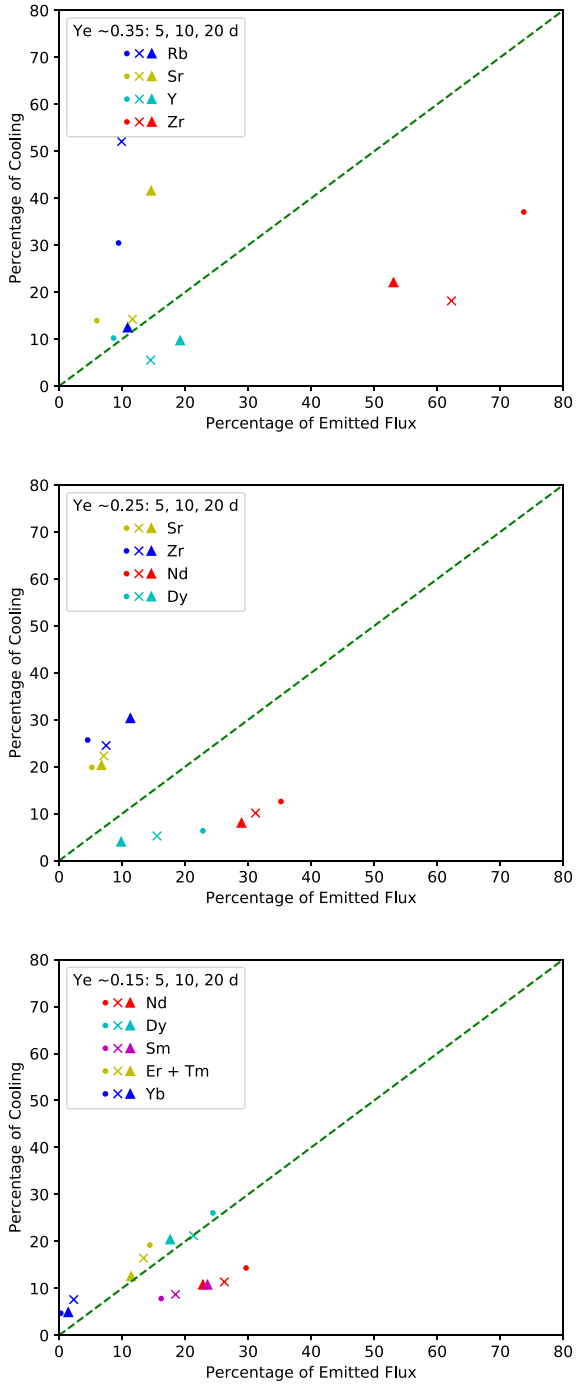

Figure 9. Comparison of the cooling (*y*-axis) versus emergent flux contribution (*x*-axis) for key elements at 5 d (points), 10 d (crosses), and 20 d (triangles). The diagonal dashed line represents equal contribution to both. Points below the diagonal indicate the emission by that element is dominated by scattering/fluorescence.

The Rb emission originates from various strong transitions in the low-lying multiplets of Rb I. Rb II is a closed-shell noble ion and therefore participates negligibly in the spectral formation. Notably, the Rb I emission at 20 d is found to be associated with the strong transition from the first excited doublet down to the ground state ($4p^6 5p$ to $4p^6 5s$), located at $\lambda_0 = 8827$, 8920 Å in our model atom, slightly redder than the measured $\lambda_0 = 7802$, 7950 Å (Volz & Schmoranzer 1996; Simsarian et al. 1998). This line remains optically thick throughout the whole ejecta at all epochs here, therefore contributing to producing an absorption trough of width ~0.3 c bluewards of ~8900 Å (~7900 Å if wavelength corrected). This trough is most distinctly seen in the model spectrum at 20 d, the reason being that at this epoch there is no other optically thick line within ~0.3 c bluewards of the Rb I line that can link in further absorption troughs, as happens at earlier epochs. This line remains important even at this late epoch when the abundance of Rb I is only ~0.04 per cent of the model by mass fraction.

The Rb I doublet has experimentally determined rest wavelengths of $\lambda_0 = 7802$, 7950 Å, quite close to the P-Cygni feature identified in AT2017gfo at rest wavelength of ~7500–7900 Å, and proposed by Sneppen & Watson (2023) to be due to Y II $4d5p$–$4d^2$ transitions, the most prominent of which has rest wavelength $\lambda_0 = 7882$ Å. Our model atom for Y II includes these lines with transition strengths of similar values, albeit at inaccurate wavelengths (~11 000 Å). We see little activity in these lines, with the transitions being optically thin ($\tau_s \leq 0.1$) in the entire ejecta, at all epochs, implying that in our model these lines are unable to produce features by P-Cygni formation. The Rb I doublet could be an alternative candidate for the ~7500–7900 Å P-Cygni feature found in the early AT2017gfo epochs, as we see strong scattering in this transition at all epochs.

Some more clues to the spectral formation processes can be found from Fig. 9 (top panel), showing the contribution to cooling and to the total emergent flux, for different elements. Rb is an important coolant, especially at 5 and 10 d, doing 30–55 per cent of the cooling, almost entirely by the collisional excitation of the $4d^2$ to $4d5p$ doublet transition mentioned above. However, we only see emission from this transition emerging as time progresses, implying that the ~10 per cent contribution of Rb to the emergent flux initially arises from other lines by scattering/fluorescence processes. At 20 d, we see clear emission from this doublet, and find that Rb lies along the diagonal in Fig. 9, implying that the 20 d emission feature is a combination of scattering (e.g. P-Cygni formation), and cooling emission following collisional excitation. Y is less important for cooling (5–10 per cent) but contributes somewhat more to emergent flux (10–20 per cent). Sr becomes the dominating source of cooling at late times (40 per cent at 20 d), which we find to be driven almost entirely by collisional excitation of the ~4000 Å ($\lambda_0 =$ 4078, 4216 Å) doublet. We find that while Zr dominates in terms of emitted flux (55–75 per cent of total), its contribution to cooling is much less (20–35 per cent), implying that most of its emission arises from scattering/fluorescence rather than cooling (assuming that recombination cannot reach such levels of emission[3]). The Zr I, II structures of closely packed multiplets with many transitions of similar strength over a wide range of wavelengths allow for effective scattering/fluorescence, as many different channels of approximately equal probabilities are available.

In terms of absorption, we see in Fig. 4 that there are many optically thick lines throughout the whole ejecta at $\lambda \lesssim 7000$ Å even up to 20 d. Initially at 5 d, we see that the majority of the ejecta are line blocked up to $\lambda \sim 1$ μm. With time, the ejecta layers gradually become more transparent for $\lambda \gtrsim 7000$ Å. However, the innermost core region at ≤0.1 c (which contains 60 per cent of the ejecta mass), remains largely blocked even at 20 d, due to many optically lines from Y and Zr, and to a lesser extent Sr.

[3]The recombination emission from element *i*, ion *j*, in zone *k*, is, roughly, $V_k n_e n_{k,i,j} \alpha(\chi + kT)$. If we look at the innermost zone (with the highest recombination rate), this becomes about 10^{37} erg s^{-1} at 10 d which is less than 1 per cent of the bolometric luminosity.

At 5 d, the figure shows that two escape windows in the line blocking exist at rest wavelengths $\lambda_0 \sim$ 1.2–1.4 and ∼1.6 μm. The first one is partial, in the sense that the ≤0.1 c core is still absorbing, whereas the second window is fully transparent. It is in these windows that much of the radiation that has been scattering and fluorescing from line to line can finally escape, producing the two distinct peaks in the spectrum at 1.1 and 1.6 μm. We find that the emission at 1.6 μm also coincides with the strongest cooling channels of Zr I, which contribute ∼5 per cent to the total Zr cooling of ∼40 per cent at 5 d (top panel of Fig. 9). However, since Zr emission in this model is overwhelmingly produced by scattering/fluorescence, it is likely that the 1.6 μm feature is partially a P-Cygni feature, even at 20 d after merger. As the line blocking in the λ_0 =6000–9000 Å range is reduced with time, a larger fraction of the flux starts to escape at these wavelengths, with Y I and Sr II being dominant emitters. Eventually, at 20 d, a window becomes fully open also at 6000 Å, giving a third peak.

The Sr II 10 000 Å triplet is optically thick throughout most of the ejecta at 5 d, and remains thick up to 0.2c at 10 d and 0.15c at 20 d. Fig. 4 does reveal several other absorption lines in that regime, however, which may complicate definitive association of an observed feature in that wavelength range to Sr II alone. In the model here, we find that Sr is an important coolant at late times (see Fig. 9), mainly by the ∼4000 Å doublet transition. Photons in that transition are however strongly resonance trapped, and the ∼10 000 Å branching triplet (same parent multiplet) provides an alternate de-excitation channel. Considering the radiative de-excitation flows ($A \times \beta_{\rm Sob} \times h\nu$), we estimate that at 5 d, ∼95 per cent of cooling excitations along the 4000 Å doublet channel radiatively de-excite in the ∼10 000 Å triplet channel. However, the Sr emergent flux contribution at 5 d is only about 1/3 of this, so a significant fraction of the photons emitted by the 10 000 Å triplet (∼2/3) are then reprocessed by other species via scattering/fluorescence. At 20 d, we find that ∼50 per cent of cooling excitations of the 4000 Å doublet are radiated away by the 10 000 Å triplet, and at this epoch a larger fraction of this directly escapes. The other ∼50 per cent (emitted by the 4000 Å lines) are likely reprocessed by the many thick lines of Y and Zr at ∼4000 Å, and re-emitted redwards. These findings suggest that the ∼10 000 Å Sr II feature in this model likely arises from a combination of scattering and cooling emission, and as such is not a pure P-Cygni feature. We discuss further the impact of Sr on lanthanide-free ejecta in more detail in Section 5.5.

The most abundant and third-most abundant elements in the $Y_{\rm e} \sim 0.35$ model are krypton (Kr) and selenium (Se) (see Fig. 1 and Table A1). Despite their high abundances, neither of them give any significant contribution to the emergent spectra here. This is due to the atomic structure of their ions, where the first excited states of opposite parity to the ground multiplet lie at relatively high energies difficult to reach by thermal collisional excitation. As such, the transitions between the lowest lying states are typically (semi)-forbidden lines, and either extremely weak, or far into the mid-infrared (e.g. the Se III 4.5 μm line studied in Hotokezaka et al. 2022). We note that calcium (Ca) has been previously suggested as important due to its co-production alongside Sr (Domoto et al. 2021), but it is not included here as its mass fraction is below our cut-off limit of 10^{-4} (see Fig. 1).

The general view is that prominent emission features can arise from both cooling and from scattering/fluorescence, emerging within limited escape windows in the optical/NIR. We tend to see emission peaks associated with optically thick lines (e.g. the Rb I feature at rest wavelength ∼8900 Å, and partially the ∼10 000 Å Sr II triplet), even up to 20 d, suggesting a continued important role of P-Cygni like line formation well after the diffusion phase has ended. Fluorescence is also important, e.g. for the Zr contributions. The importance of radiative transfer processes, also at 20 d, implies that the KN is not yet in a purely optically thin ('nebular') phase by this time for its optical/NIR emission, even for our lightest model which does not include high opacity elements like lanthanides or actinides.

5.2 The $Y_{\rm e} \sim 0.25$ model

The elemental contributions to the spectra of the $Y_{\rm e} \sim 0.25$ model are shown in Fig. 5 at 5, 10, and 20 d after merger. Consistently across every epoch, we see strong lanthanide contributions (light grey shading) to the spectral emission across all wavelengths. The lanthanides achieve this prominence despite having a mass fraction of only 0.015 in the model composition. Of the lanthanides, the most prominent specific elements are Nd (neodymium), Sm (samarium), Eu (europium), and Dy (dysprosium), marked out with individual colours. The ∼1.6–1.7 μm feature seen in this model is produced by a mix of Nd and Dy, with Zr (which produced a strong feature at this wavelength in the $Y_{\rm e} \sim 0.35$ model) now being negligible. Past 1.5 μm, the IR emission is entirely dominated by Nd and Dy.

From the plot of optically thick lines at 5 d, one may identify an escape window at λ_0 ∼1.8 μm (the innermost zone at ≤0.1 c remains opaque but cannot stop all radiation); the formation of a peak at this wavelength may thus be explained in a similar manner as the 1.1 and 1.6 μm peaks in the $Y_{\rm e} \sim 0.35$ model. It is Dy which provides the last optically thick lines before the window, which explains its prominent emission at those wavelengths. Indeed, Dy lies well down below the diagonal in the cooling versus flux contribution plot (Fig. 9), which shows that this is scattering/fluorescence emission. The windows in this model are, however, less pronounced, which gives a smoother overall spectrum with less dramatic peaks and troughs.

Neodymium is even more extreme in its dominance by scattering/fluorescence (Fig. 9). It provides a rich set of optically thick lines throughout the optical/NIR range at all epochs (Fig. 6), enabling it to absorb and reprocess a significant amount of radiation, playing a similar role here to the one of Zr in the $Y_{\rm e} \sim 0.35$ model.

The landscape below 1.5 μm is more complex, with several different species contributing to the emission and absorption. The dominating lanthanides in this range are Nd, Sm, and Eu. Around 10 000 Å we recover the Sr II triplet feature with the corresponding absorption at ∼8000 Å, with Fig. 6 showing that in this model Sr II is the only ion that provides optically thick lines in the outermost layers, at 5 and 10 d. A partial escape window can be seen between $\lambda_0 \sim$ 8000–10 000 Å at 5 and 10 d, which allows for formation of a feature approaching that of a classical P-Cygni profile by Sr II. Thus, for epochs up to 10 d or so, an absorption trough by the Sr II triplet becomes distinct in the overall spectrum, even though the Sr mass-fraction abundance at this $Y_{\rm e}$ is only 0.03, compared to 0.19 in the $Y_{\rm e} \sim 0.35$ model.

Bluewards of $\lambda \sim$ 7000 Å, emission is dominated by Zr. As such, while the optical red and NIR emission is dominated by the lanthanides, the bluer optical regime does retain important contributions from first r-process peak elements. The abundant elements Sn (0.17), Se (0.13), Kr (0.091), Cd (0.054), and Ge (0.052) produce no significant emission or absorption. The reasons discussed above for Kr and Se also apply to the other elements listed here, which have similar atomic structures, i.e. a ground multiplet followed by low-lying states of the same parity, with opposite parity states at thermally inaccessible energies.

In Fig. 9, we see that Sr and Zr play important cooling roles, as for the $Y_e \sim 0.35$ model. However, Zr is now outdone by the lanthanides for scattering and fluorescence, having the last interaction for a minority of the photons, and moving left in the diagram. As discussed above, the dominating lanthanides Nd and Dy are firmly within the scattering/fluorescence regime. This suggests that species with particularly strong transitions in optical wavelengths, corresponding to the more energetic thermal electrons, are key for cooling. Species with many closely packed multiplets providing weaker, but still allowed transitions at redder optical and NIR wavelengths represent ideal scattering/fluorescence conditions, as photons are able to be absorbed and re-emitted over a broad range of wavelengths. In both Nd and Dy, we see their contribution to the overall emitted flux decreasing with time, which is consistent with expectations for the evolution of scattering/fluorescence processes. It is possible that the KN will transition to a fully optically thin thermal nebular phase, which for these models would occur later than 20 d after merger. However, increasing temperatures may bolster emission of photons in the UV where line blocking may still be effective, thus leading to a 'fluorescence' nebular phase similar to SNe after many years (Jerkstrand 2017).

5.3 The $Y_e \sim 0.15$ model

Looking now at the $Y_e \sim 0.15$ model shown in Fig. 7, we see that the emergent spectra are almost entirely dominated by lanthanide emission across the entire wavelength range. The shape of the emergent spectra of this model remains relatively similar across all epochs, with the amplitude of individual features varying in different ways. In particular, we recover also here the distinct Nd and Dy feature at 1.7 μm, which is the dominant emission feature at all epochs. As for the $Y_e \sim 0.25$ model, the emission past 1.5 μm is dominated by Nd and Dy, with some additional contributions from Er and Tm. The actinides Th and U, with a small abundance of ∼0.001 each, contribute a little bit of emission between 2.5 and 3 μm.

The strong Nd feature at 2.5 μm is persistent across all epochs, as well as the apparent trough on its blue side. Combining the information that Nd is strongly scattering/fluorescence dominated (Fig. 9) and that there is a thick Nd line at λ_0 ∼2.55 μm in many ejecta layers at all epochs (Fig. 8), we conclude that this line is probably formed primarily by the P-Cygni mechanism.

We also see the emergence of a prominent Te feature at ∼1.3 μm, which is distinct in the spectra across all epochs. Looking closer at the levels and transitions responsible for this emission we cannot, however, clearly link these to experimentally validated levels, and so choose not to analyse this feature in more detail due to its unreliability.

In the optical, the lanthanide samarium (Sm) is the element contributing most of the flux. The reason for this is its dominant line blanketing in the optical (Fig. 8), and indeed this yields scattering/fluorescence emission (Fig. 9). Dy, Th, and U also provide some contributions to the optical flux. Conversely, Zr, which was significant in the $Y_e \sim 0.25$ model, is only at 0.015 abundance here, and does not contribute much to the spectral formation. From Fig. 8, we see a large amount of line blocking at 5 d, with a partial escape window around $\lambda_0 \sim 1.7$–2.1 μm, which allows the emergence of the large 1.7 μm peak. At 10 d, we also identify a partial escape window at $\lambda_0 \sim 7000$ Å, which leads to the Sm peak at ∼5000 Å. We also see a strong U IV absorption line at rest wavelength $\lambda_0 = 8400$ Å, which drives the trough formation at $\lambda \sim 7000$ Å, most noticeable at 10 and 20 d. Given the U emission just redwards of this feature, and finding that this transition does negligible cooling, we suggest this to be a P-Cygni like feature. However, due to the lack of atomic data for U IV, we cannot verify the accuracy of this particular transition. As in previous models, we see how spectral peaks arise within escape windows in the line blocking, rather than corresponding to any particular transition.

Hotokezaka et al. (2023) identify [Te III] 2.1 μm as a candidate for the observed emission-like line in AT2017gfo at epochs 7.5–10 d. Our $Y_e \sim 0.15$ model here has a similar composition as their $A > 88$ model, both with little to no material from the first r-process peak, and a large Te mass fraction (0.07 in our model). Our model atom has the transition at theoretical wavelength $\lambda = 2.21$ μm and with transition rate $A = 1.6\ \mathrm{s}^{-1}$, both close to the values calculated by Madonna et al. (2018). However, our effective collision strength for this transition follows the prescription for forbidden transitions from Axelrod (1980): $\Upsilon = 0.004 g_i g_j = 0.012$, for upper level i and lower level j, respectively. This value is much lower than the value calculated by Madonna et al. (2018) of $\Upsilon \gtrsim 5$ (for $T \lesssim 5000$ K). The significance of this depends on whether the line is close to LTE or not. In our model, we find that the population of the upper level of this transition has a departure coefficient of $\sim 10^{-2}$ (see also fig. A2 in Pognan, Jerkstrand & Grumer 2022b), implying that this line is far from LTE, and as such our smaller collision strength has a direct impact. On the other hand, for our model at 10 d, we have higher temperature solutions ($T = 4000$–$24\,000$ K) than that assumed by Hotokezaka et al. (2023) of 2000 K, which gives a higher emissivity for a given departure coefficient. These two differences in physical conditions, combined, give a total (angle-integrated) emissivity from this line of 2.2×10^{38} erg s^{-1}, about an order of magnitude smaller than the observed value of $\sim 2 \times 10^{39}$ erg s^{-1} (Hotokezaka et al. 2023). As such, it is possible that a too low intrinsic emissivity of the [Te III] 2.1 μm line is at least partially responsible for its lack of emergence in our model.

Another aspect to consider is to what extent an emission line at 2.1 μm is free to directly escape at 5–10 d. In our model, the inner 2–3 zones (corresponding to 90 per cent of the ejecta mass) still have some line blocking at these epochs, such that any [Te III] emission at that wavelength will be at least partially absorbed and re-emitted at longer wavelengths. However, in contrast to the 'forest' of blocking lines below ∼1.5 μm, the opacity here is provided by relatively few lines. Given the current limitations to the accuracy of wavelengths and A-values, one cannot yet make any real robust statements about the degree of optical thinness around 2.1 μm in the 5–10 d epochs.

Looking at the bottom panel of Fig. 9, we see that the dominating species, all of which are lanthanides, typically lie close to the dividing line between cooling driven and scattering/fluorescence driven emission, with Nd and Sm being more on the latter side. Since most of these species have similar structure with open f-shells, it is somewhat expected that they would behave similarly. As such, the competition between these elements with respect to domination of scattering/fluorescence or cooling likely comes down to details in their atomic structure. Overall, this very lanthanide-rich model showcases how difficult it may be to identify single species in a composition representative of low Y_e ejecta. The atomic nature of the lanthanides, and typical lack of stand-out strong transitions, yields spectra with broad, blended absorption and emission features that often arise from many different species. The peaks formed, even at 20 d, tend to arise in escape windows within the line blocking, rather than corresponding to any intrinsically important emission lines.

5.4 Time-dependent effects on spectra

We now take a closer look at the effects of using the full time-dependent equations on the emergent spectra. As shown previously in Section 4, only the $Y_e \sim 0.35$ model appears to show significant effects in the thermodynamic quantities, and this is also reflected in the spectral output. Conversely, the $Y_e \sim 0.25$ and 0.15 models show little to no difference in their emergent spectra. The comparison of the total spectral output in steady-state and time-dependent modes from 10 to 20 d for the $Y_e \sim 0.35$ model are shown in Fig. 10 along with the elemental contributions of the same key elements as identified above.

As expected, we find that time-dependent effects increase as time goes on, following the same trend as seen in Section 4. These changes are too small to affect the emergent spectrum at 10 d after merger, but differences become noticeable from 15 d onwards. The time-dependent solution has a smaller emission peak at ∼6000 Å, and at 20 d, more emission around 1.7 μm. As the main effects of the time-dependent results are to lower temperature and the degree of ionization, we must consider both in tandem to explain the effects on the emergent spectrum. Since the strongest emitting species in the model are neutral and singly ionized species, a lower ionization degree will increase the abundance of these species, which would, to first order, imply increasing their emission.

However, the ejecta temperature is also cooler, such that transitions excited by thermal collisions are weaker. For many of the emission lines, we therefore have a competing effect, where although we have a higher abundance of an emitting species, the total emission may actually decrease due to lower emissivity from cooler temperatures (see Fig. B2 for a detailed look of time-dependent effects on the key species). These competing effects leading to changes in the emergent spectrum, highlight the complex nature of time-dependent effects not only on the thermodynamic state of the ejecta, but also on the emergent spectra. These results suggest that accurate spectral analysis of low-density, lanthanide-free ejecta may require time-dependent, NLTE modelling in order to be properly interpreted.

5.5 The effects of strontium on lanthanide-free ejecta

Sr has been proposed as responsible for a spectral feature in AT2017gfo seen up to about a week after merger (Watson et al. 2019; Domoto et al. 2022), though an alternative He origin has also been suggested (see e.g. Perego et al. 2022; Tarumi et al. 2023). To study in more detail how our models are affected by Sr, we run again the $Y_e \sim 0.35$ model with Sr removed. In order to maintain a constant total ejecta mass, the mass fractions of the other elements were correspondingly adjusted (see Table A1), while the energy deposition remained as before.

Considering first the thermodynamic state of the ejecta, we generally find higher temperatures when removing Sr from the model, in the range of ∼100–1500 K from the innermost to outermost ejecta layers, respectively, the difference typically becoming more important as time progresses. Sr has a particularly strong effect on the ejecta's temperature due to the efficient cooling in the Sr II ∼4000 Å channel. This transition is found to provide up to ∼40 per cent of the total cooling for ejecta layers where Sr II is highly abundant (e.g. Fig. 9). As such, removing Sr from the model significantly reduces the cooling capacity of the ejecta, thereby increasing the temperature.

Although most individual species become slightly more ionized, the overall electron fraction x_e of the medium decreases. This is because Sr I and II are quite easily ionized, and the typically dominant species is therefore Sr III. Conversely, most other species in the ejecta are more abundant in their singly ionized states. As such, removing

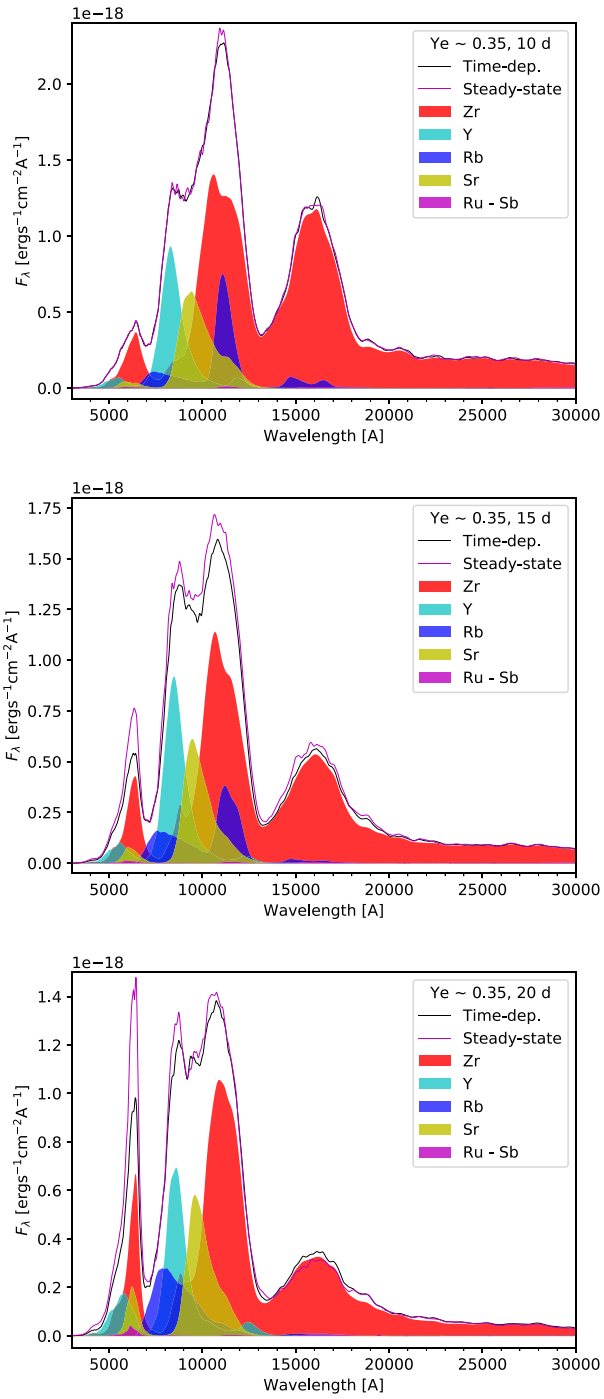

Figure 10. The key emitting species in the $Y_e \sim 0.35$ model at 10, 15, and 20 d. The black spectra are the time-dependent solutions, while the magenta spectra are the steady-state solutions. The filled area showing elemental contributions are with respect to the time-dependent solution.

Sr from the model leads to an overall decrease of electron fraction x_e, although other elements are slightly more ionized. A smaller number of free electrons in the ejecta further aids in increasing the temperature.

The emergent spectra of the $Y_e \sim 0.35$ model with and without Sr are shown in Fig. 11. We focus on the changes arising from Y and Zr, as we find that the spectral features of the other elements in the model do not appear to be strongly affected. The presence of Sr in

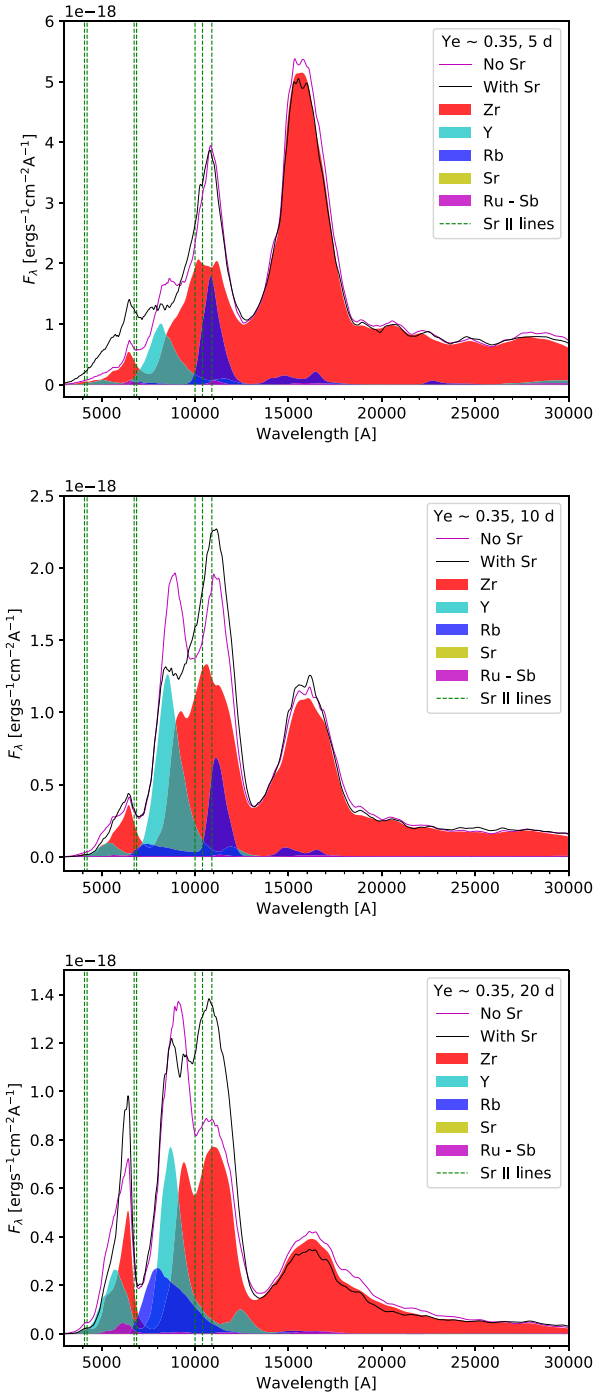

Figure 11. The effect of including (black) and excluding (yellow) Sr on the $Y_e \sim 0.35$ model spectrum. The elemental contributions of Rb, Y, and Zr are marked out by the fills, and correspond to the Sr-free model. The vertical dashed green lines mark out the rest wavelengths of the Sr II 4000, 6800 Å doublets and the 10 000 Å triplet, respectively.

the ejecta mainly causes changes in the wavelength range $\lambda \sim 8000$–12 000 Å by effect of the 10 000 Å triplet. Certain effects can also be seen at shorter wavelengths, but line formation there is extremely complex, while there is also an effect at longer wavelengths, though it is relatively minor. Thus, we focus on the 8000–12 000 Å range in our analysis.

At 5 and 10 d, the presence of Sr gives a more extended and deeper absorption trough at ∼8500 Å in the spectrum compared to a composition without it, suppressing flux levels specifically around this wavelength. The effect on the 1.1 μm peak is small however, with Sr slightly decreasing flux levels at 5 d and slightly increasing them at 10 d. Thus, the situation appears far from a single-line P-Cygni limit within 10 d after merger. Only at 20 d does Sr noticeably increase the strength of that feature, then by a factor of roughly 1.4, while slightly decreasing the flux levels at ∼8500 Å by absorption from the 10 000 Å triplet.

In Section 5.1, we identified the 1.1 μm spectral peak as arising due to an escape window opening up around this wavelength. Its persistence also for compositions without Sr would then be explained by several other lines from Y, Zr, and Rb also providing optically thick lines up to, and around this wavelength. Sr helps out in this chain of reprocessing radiation towards the escape window, but it is not crucial. However, we see a marked change in the spectral shape around 10 000 Å from 10 d onwards when Sr is added. Therefore, these models support Sr as being active in KN spectral formation, in particular through its 10 000 Å triplet. However, the specific impact of Sr may be complex, with the effect of the 10 000 Å feature being not easily distinguishable from other line scattering processes. We note again that our analysis here is limited to epochs ≥5 d, so the situation may be different at earlier phases.

6 COMPARISON TO AT2017GFO

In this section, we compare the evolution of our models to that of AT2017gfo with respect to bolometric luminosity (Fig. 12) and colour evolution in *grizJHK* colours (Fig. 13). Given the limited accuracy of wavelengths in our data set, the models generally do not yield accurate predictions for specific features. However, we expect that the models are able to reasonably capture the general SED. For these reasons, we here focus our comparison with AT2017gfo mostly to colours, which test the general shape and evolution of the SED.

6.1 Bolometric and optical light curves

Considering first the bolometric LC in Fig. 12, we see that our models are typically fainter than AT2017gfo at early times, until about 10 d after, with only the $Y_e \sim 0.15$ model reaching comparable and greater luminosities past 10 d. The disparity is worse at earlier times, with the $Y_e \sim 0.35$ model being more than an order of magnitude dimmer than AT2017gfo at 5 d after merger. Conversely, the $Y_e \sim 0.15$ model has a bolometric luminosity mostly consistent with AT2017gfo from 10 d onwards, though it should be noted from the error bars that the observed luminosity is poorly constrained at these late epochs. This higher luminosity is consistent with the greater power of the model, which can be seen in Fig. A1. There, we see that at these epochs, this model has a spontaneous fission contribution to the energy deposition that is roughly equal to the β-decay contribution, with α-decay also adding a further ∼20 per cent.

There are several possible reasons for such a dim bolometric luminosity at early times. These include too little ejecta mass, particularities in the raw decay power for the chosen Y_e, or too inefficient thermalization, leading to reduced energy deposition to the ejecta. Another significant factor may be time-dependent photon diffusion effects, which are not taken into account by SUMO. Diffusion was previously discussed in Section 3.4, where previous LC studies including diffusion effects have found that these play a role until 5–20 d, depending on composition (e.g. Tanaka et al. 2020; Bulla 2023).

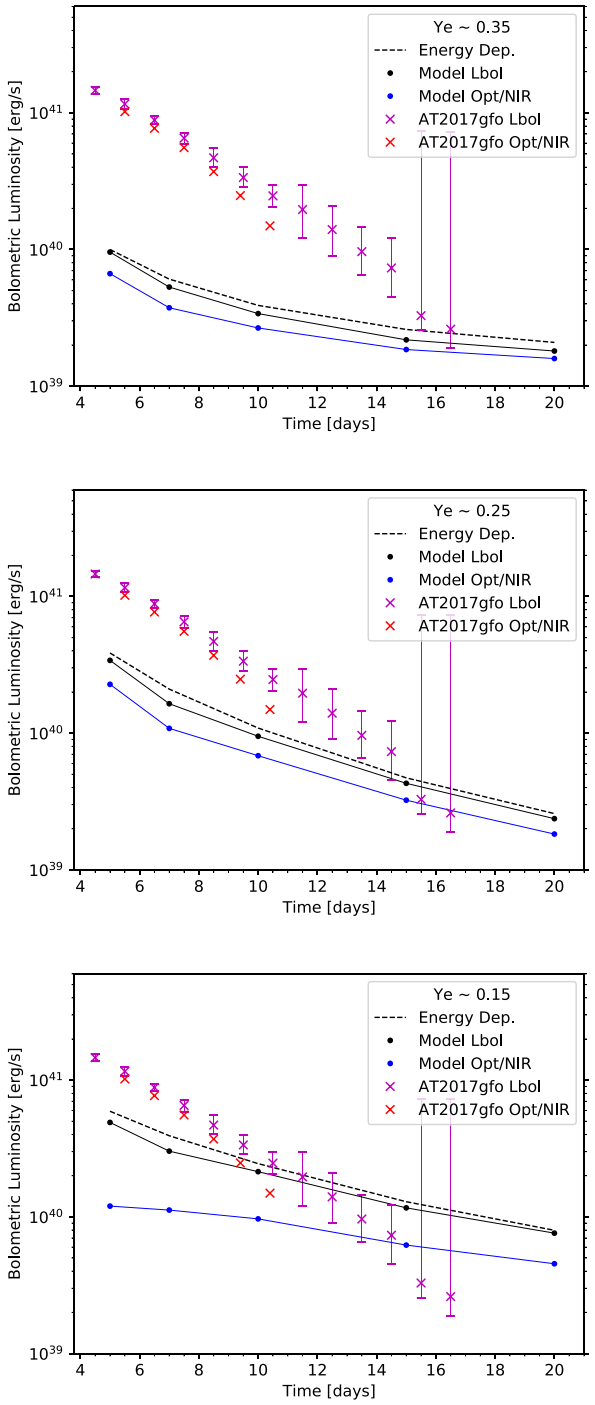

Figure 12. The bolometric light curves of each model compared to those of AT2017gfo as calculated by Waxman et al. (2018). The magneta crosses arise from integration of photometric data, while the red crosses are luminosity estimates in the 0.3–2.4 μm range calculated by integrating a blackbody fit. We compare our model to the latter by integrating our spectra in the same range (points), corresponding to the wavelengths of the X-shooter spectra of AT2017gfo. We note that no uncertainties are provided for the luminosity calculated from the blackbody fit. The energy deposition in our models (including thermalization effects) are shown by dashed black lines; the emergent bolometric luminosity is somewhat lower than this due to adiabatic losses as photons scatter.

As our ejecta mass of 0.05 $M_\odot$ lies well within the range of most estimates for AT2017gfo (e.g. Kasen et al. 2017; Pian et al. 2017; Smartt et al. 2017; Tanaka et al. 2017; Waxman et al. 2018), and our thermalization physics comes from well-accepted semi-analytical fits (Barnes et al. 2016; Kasen & Barnes 2019; Waxman, Ofek & Kushnir 2019), which were also well reproduced numerically by Hotokezaka & Nakar (2020), we do not believe these two explanations to be the main cause. With respect to the raw radioactive power arising from the composition, we can see from the top panel of Fig. 12 that our $Y_e \sim 0.35$ model is naturally a low-power model. This is a particularity of this Y_e, as the nuclear power of this model between 1 and 20 d is quite small owing to the relatively few isotopes that substantially contribute to radioactive heating (see fig. 5 in Wanajo et al. 2014). It should be noted however, that nuclear power at slightly higher $Y_e \sim 0.4$ is larger due to the important contributions from the β-decay chains of ^{66}Ni and ^{72}Zn (Wanajo 2018). Furthermore, AT2017gfo is expected to synthesize heavier elements past the second r-process peak (e.g. Kasen et al. 2017; Tanaka et al. 2017; Rosswog et al. 2018; Waxman et al. 2018), and potentially trans-lead elements which may provide additional power by efficiently thermalizing α-decay particles (e.g. Wanajo et al. 2014; Wanajo 2018). As such, it is expected that the bolometric luminosity of this light composition model be lower than that of AT2017gfo.

The other two models, with heavier elemental compositions, do not have intrinsically low power, and their dimmer luminosity for $\lesssim$10 d thus likely arises from the omission of time-dependent photon diffusion in SUMO. In Tanaka et al. (2020) and Hotokezaka & Nakar (2020), emergent bolometric LCs are plotted compared to the instantaneous deposition after thermalization. It is seen there that diffusion is going on in the models up to 10–30 d, depending on the ejecta. On the other hand, the bolometric LC is never more than a factor $\sim$2 brighter than the deposition. Bulla (2023) shows that the ratio can depend strongly on viewing angle in multi-D model, obtaining up to a factor 3 difference for polar viewing angles, at 5 d, but a negligible ($\lesssim$10 per cent) effect for equatorial angles. For the angle inferred for AT2017fgo of $\theta \sim 30^\circ$ (e.g. Pian et al. 2017; Troja et al. 2017; Finstad et al. 2018; Bulla 2019), the factor is about 2, similar to the 1D results. One should note that LTE models with complete thermalization of photon absorptions, such as these, may overestimate the duration of the diffusion phase as fluorescence to longer, more optically thin wavelength regions is not allowed to occur. However, by what extent cannot currently be addressed, and the AT2017gfo data itself also does not allow this to be determined. In contrast to observed SN LCs, for which the diffusion phase is clearly identifiable, the fact that all KN ejecta are radioactive produces a rather indistinct difference between diffusion and steady-state LCs. As such, we may take a factor 2 as an upper limit to the luminosity factor.

Additionally, the factor between emergent luminosity and deposited energy is not exactly unity in models with stationary radiation fields such as ours. This is due to adiabatic degradation of the radiation field (note distinction to the adiabatic cooling of the thermal electrons as the ejecta expand) as photons interact on their way out. We find in our models that this adiabatic loss factor is $\sim$5–25 per cent, depending on model and epoch. As such, the factor 2 discussed above gets compounded due to adiabatic degradation, giving a total factor $\lesssim$3. We assess this is likely the driving factor behind the significantly too low luminosities of our $Y_e \sim 0.25$ and $Y_e \sim 0.15$ models between 5 and 10 d. Studies of the effects of photon diffusion in the context of Type Ia SN have found that while the bolometric luminosity may be reduced by a factor of 2–3 when omitted, the spectra remain very similar (Kasen, Thomas & Nugent 2006; Shen et al. 2021). As such, we do not make any predictions for KN LCs at early times when

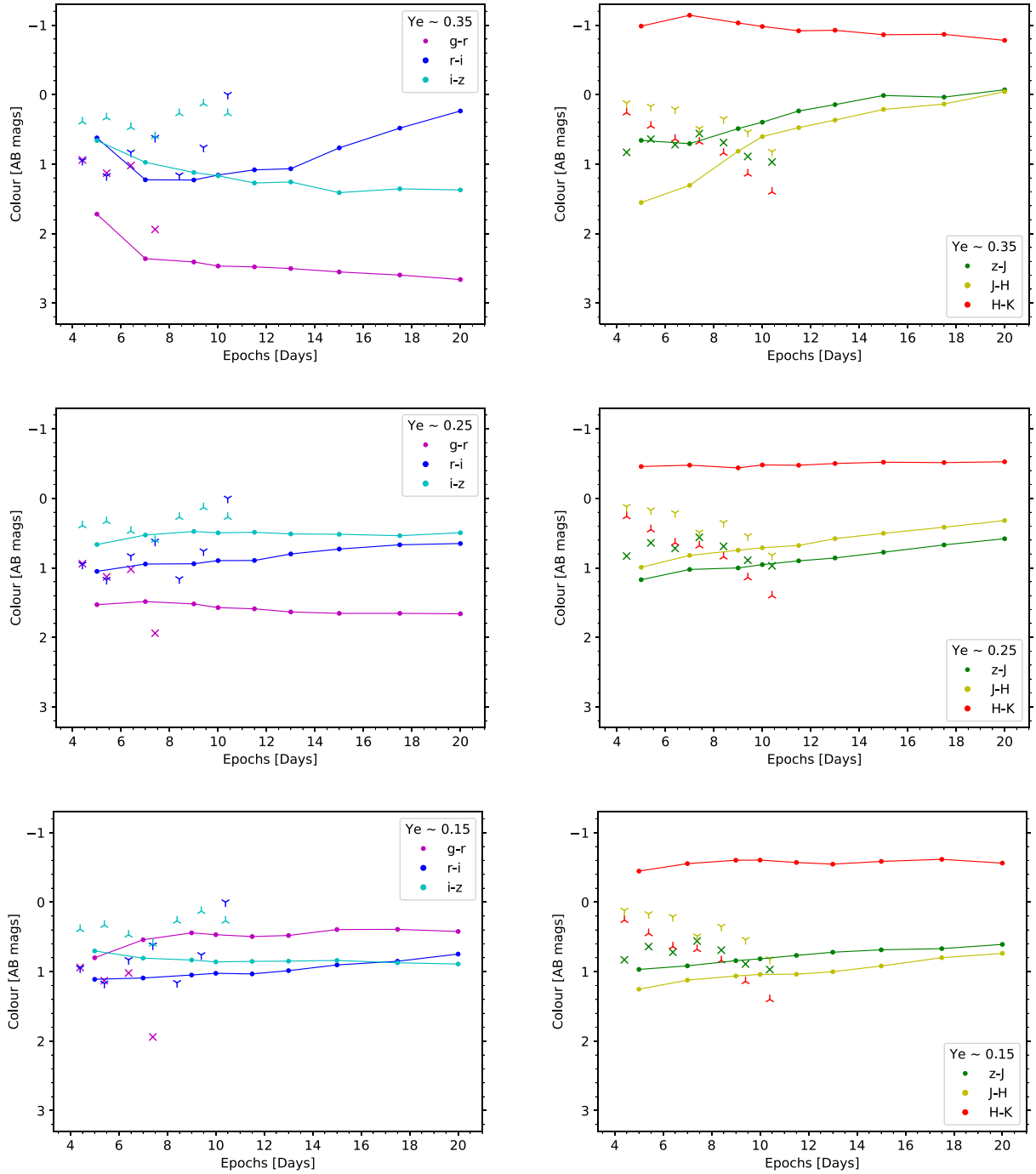

Figure 13. Colour evolution of our models (points) in optical and NIR colours on the left-hand and right-hand sides, respectively, compared to the observed colour evolution of AT2017gfo (crosses and Y-shapes) in the first 20 d after merger. We note that AT2017gfo is missing observations in several photometric bands after 10 d, so we limit ourselves to the first 10 d which have reliable photometric measurements in most bands, aside from g band which stops after 7.4 d.

diffusion may still be playing a role, but expect that the general SED shape, and thus the colours of our models, remain accurate.

6.2 Colours

We compare the colour evolution of our models to that of AT2017gfo in Fig. 13. Optical colours $g - r$, $r - i$, and $i - z$ are shown in the left-hand panels, while NIR colours $z - J$, $J - H$, and $H - K$ are shown in the right-hand panels. We note that the observed g-band photometry for AT2017gfo was limited to upper limits past 7.4 d (e.g. Villar et al. 2017), and so the $g - r$ colour for AT2017gfo is only shown up to that epoch. We see a relatively flat colour evolution for our models, with the exception of the $Y_e \sim 0.35$ model in the first few epochs. While the NIR colours of AT2017gfo show a marked

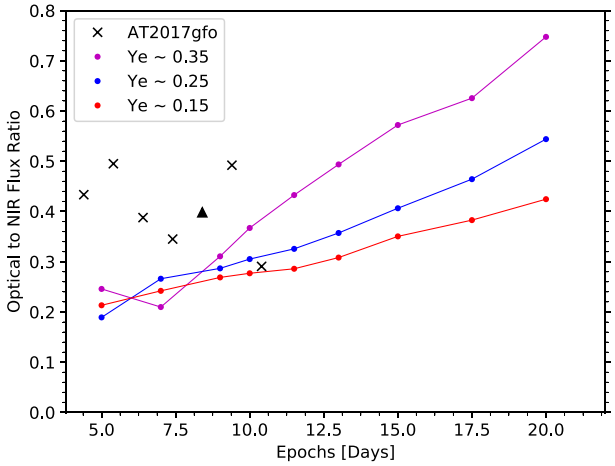

Figure 14. The ratio of flux in the optical ($3000 \geq \lambda \geq 10\,000$ Å) to the NIR ($10\,000 \geq \lambda \geq 24\,000$ Å) for our models (solid lines) and from the spectra of AT2017gfo (crosses). The triangle at 8.4 d for AT2017gfo is a lower limit due to the X-Shooter spectrum lacking data below $\lambda = 6000$ Å.

reddening with time, our models instead tend to get slightly bluer over time in the NIR colours.

Although the colour evolution of both our models and AT2017gfo do not immediately appear to present a marked blue to red evolution in the 5–10 d regime, these colours are taken between adjacent bands in which the evolution may depend on the (dis)-appearance of individual features. In order to provide a 'colour' evolution with a larger perspective, we calculate the ratio of flux in the optical (3000–10 000 Å) to that in the NIR (10 000–24 000 Å), shown in Fig. 14. There, we see a clear trend for our models, where more flux is present in the optical regime as time goes on, i.e. the models get 'bluer'. The lightest model ($Y_e \sim 0.35$) evolves the fastest, while the $Y_e \sim 0.15$ model, with the highest lanthanide abundance, evolves the slowest. AT2017gfo, conversely, shows a large spread in its flux ratio values, consistent with a constant ratio over time, with the exception of the 10.4 d value which indicates transfer from optical to NIR (note that the point at 8.4 d is missing flux below 6000 Å and so is a lower limit).

The increasing optical flux of our models is explained by the increasing temperatures (Fig. 2) combined with the decreasing optical depths in the optical regime (Figs 4, 6, and 8). As time progresses, the radiation field therefore generally becomes bluer, and is also able to escape at these wavelengths. At early times, blue photons are forced to scatter/fluoresce to redder wavelengths in order to escape, particularly for our heavier composition models. Considering models at 5 d (top panels of Figs 4, 6, and 8), we see many optically thick lines throughout the whole ejecta at wavelengths $\lambda \lesssim 10\,000$ Å. Taking the lowest temperature of our ejecta yielding the reddest photons, $T \sim 2500$ K in the innermost layer at the earliest epoch, to be representative of characteristic photon energies, we find, using Wien's law, a peak photon wavelength of $\lambda \sim 11\,500$ Å, well within the optically thick regime for this inner layer. As outer layers have higher temperatures, the representative photon wavelength is pushed to bluer, and more optically thick wavelengths. Therefore, we find that scattering/fluorescence play a critical role in the spectral formation of KNe, and are expected to continue doing so until the optical depth has dropped sufficiently such that the KN enters a truly optically thin regime.

The only exception to the increasing optical flux trend in our models arises in the transition of the $Y_e \sim 0.35$ model from 5 to 7 d after merger, where we see comparatively more flux in the NIR. This does not arise due to increased flux in the NIR, but rather a decrease in optical flux. This particular evolution highlights that the SED evolution of KNe in this regime also depends highly on specific features, and not only general temperature and optical depth.

Alongside the complex colour evolution shown in Fig. 13, our results imply that the temperature of the ejecta cannot be reliably inferred from the shape of the SED. As an example, the best-fitting blackbody to the 5 d spectrum of the $Y_e \sim 0.25$ model gives a temperature of ∼2000 K, whereas the ejecta temperature ranges from ∼4000 to 12 000 K. Furthermore, we see that the $Y_e \sim 0.15$ model, which typically has the lowest optical to NIR flux ratio, is actually *hotter* than the other models, as seen in Fig. 2. Since the temperature solution of the gas in NLTE is a balance of radioactive heating and predominantly line cooling, both of which depend heavily on composition, it is not surprising that both the temperature solution and emergent spectra are highly different between these models.

In general, the model spectra generated in this study are not expected or intended to be particularly similar to AT2017gfo given the simplicity of the morphology (1D) and homogeneous compositions, as well as limited accuracy of our atomic data and relatively simplified treatment of several NLTE processes. With respect to the ejecta model, AT2017gfo is believed to have had multiple components with different compositions and complex 3D morphology (see e.g. Perego, Radice & Bernuzzi 2017; Metzger 2019; Shibata & Hotokezaka 2019, for reviews). The apparent lack of a 'continuum'[4] in our spectra may arise from the 1D, homogeneous nature of our models. For a given composition, the same optically thick lines will be blocking similar regions of the spectrum, further blueshifted from their rest wavelength the farther out they are in the ejecta. As such, blue photons are continuously line blocked and cannot escape without relying on scattering and fluorescence.

In a more realistic 3D inhomogeneous model, photons will have access to more escape routes where differing compositions provide different escape windows in the line blocking. The recent study of Shingles et al. (2023) modelled the early-time emission from a purely dynamical ejecta component ($M_{ej} = 0.005\,M_\odot$) also with fluorescence fully considered. There, they found significant dimensional effects on the emergent spectrum, notably that the 1D spectra are less 'continuum' dominated than the 3D spectra. At this point however, it is not fully known to what extent geometrical effects play a role in the total emergent spectrum, since the dominant wind component (typically $\gtrsim$90 per cent of the ejecta mass) is expected to be somewhat more spherically symmetric than the dynamical component (e.g. Kawaguchi et al. 2021, 2023; Neuweiler et al. 2023). As such further studies taking into account key transfer processes such as fluorescence, and comparing geometries and compositions in 3D while also including the disc wind component are required to thoroughly establish the effects of dimensionality.

7 DISCUSSION AND CONCLUSION

We have conducted 1D NLTE radiative transfer simulations with the spectral synthesis code SUMO in order to generate KN spectra from 5 to 20 d after merger. We study three uniform-composition, multizone models of varying characteristic $Y_e \sim 0.35$, 0.25, and 0.15, with compositions including up to 30 different elements in each model, and nuclear decay power from Wanajo et al. (2014).

[4]The 'continuum' in line-emission dominated KNe is technically an overlap of many weak lines, and does not arise from continuous processes.

We determine the temperature profiles of the ejecta, showing that the temperature for the most part increases monotonically outwards, although in some cases the peak is reached at an interior mass coordinate. As has been shown also in previous works (Hotokezaka et al. 2021; Pognan, Jerkstrand & Grumer 2022a), KN temperatures increase with time in the post-diffusion phase. Our model temperatures are 2500–5000 K in the innermost ejecta layers, while outermost layers have a larger range of 5000–35 000 K, depending on model and epoch. The ionization degree correspondingly spans $x_e \sim 0.7$–2.2 (innermost layer) and $x_e \sim 1.6$–2.9 (outermost layer). Thus, neutral, singly ionized, and doubly ionized ions all play a role for 5–20 d KN spectral formation.

We show that KN ejecta are to a large extent still opaque in the optical/NIR due to line blocking, even up to 20 d. Much of the spectral shape and features of our models are determined by the location of optically thin, or reduced optical depth windows in this line blocking. We typically find that wavelengths of $\lambda \lesssim 7000$ Å are completely line-blocked, whereas at longer wavelengths the blocking is partial. The emergent peaks tend to arise in windows of reduced optical depth rather than at the location of e.g. important cooling lines.

We find that for a lanthanide-free composition ($Y_e \sim 0.35$), the neutral and single ionized species of group I–IV elements of the first r-process peak, Rb, Sr, Y, and Zr, dominate the spectral formation. These elements have few valence electrons, with strong transitions between low-lying states giving contributions at distinct wavelengths. This makes these species promising candidates for identification in current and future KN observations. Zr I, which has many closely packed multiplets of the same parity at low energies, also has many (semi)-forbidden transitions at red wavelengths alongside the allowed transitions. This leads to Zr I dominating the NIR regime of the lanthanide-free model; our models indicate that at this Y_e almost the entire NIR spectrum is formed by Zr.

We test in greater detail the effect of Sr on the emergent spectrum by running the $Y_e \sim 0.35$ model with Sr omitted. We find that the presence or absence of Sr significantly impacts the 8000–12 000 Å spectral region, through the Sr II $\lambda_0 = 10\,039$, 10 330, 10 918 Å triplet. Secondary spectral effects also arise from the impact of Sr on the thermodynamic state of the ejecta, which become somewhat hotter and more ionized. Notably, we find that the Sr II doublet at ∼4000 Å is a particularly efficient cooling transition, and its removal leads to higher temperatures. However, we also find that inferring the presence of Sr directly from the spectral shape around 10 000 Å may in general not be straightforward, as we find many optically thick lines from other species at similar wavelengths, and quite complex spectral formation at those wavelengths. Our model gives a peak around 1.1 μm also without any Sr (or He).

We establish that Rb I has an important and active doublet transition at experimentally measured rest wavelength $\lambda_0 = 7802$, 7950 Å (∼8900 Å in our model atom). In our lanthanide-free model ($Y_e \sim 0.35$), we see strong scattering in this transition as it remains optically thick throughout the entire ejecta even to 20 d. This transition may be an alternative to the proposed Y II transitions (Sneppen & Watson 2023) for the ∼7600 Å P-Cygni like feature in the spectrum of AT2017gfo.

In the lanthanide-bearing $Y_e \sim 0.25$ and 0.15 models, we find that the lanthanide species dominate the spectral formation. We identify several specific lanthanides – neodymium (Nd), samarium (Sm), and dysprosium (Dy) – which appear to play particularly important roles, and are thus promising candidates for diagnosis in 5–20 d observations of KNe characterized by low Y_e. Our current model atom wavelengths are unfortunately not accurate enough that we can robustly predict specific features from these, but by identifying that these particular elements are highly active in the spectral formation, we provide impetus for further efforts in better determining their atomic properties. The two actinides we consider, Th and U, make up only 0.003 of the composition by mass fraction even at $Y_e \sim 0.15$ (see Table A1) and have little impact on the spectra in our models; detection of these may plausibly occur only for yet more neutron-rich KNe ($Y_e < 0.15$). In the $Y_e \sim 0.25$ model, we also see the continued presence of the Sr II 10 000 Å triplet, providing support that such a feature may also be observable in lanthanide-bearing ejecta.

We do not see (in our $Y_e \sim 0.15$ model) the emergence of the [Te III] 2.1 μm emission line proposed as the explanation for the feature seen in the spectrum of AT2017gfo at 10 d (Hotokezaka et al. 2023). We find two reasons for this; the first is that our prescription used to calculate collision strengths for forbidden lines (Axelrod 1980) in this case gives a much lower value than the dedicated calculation by Madonna et al. (2018), giving significantly lower emissivity. Secondly, we do not obtain optically thin conditions at 10 d around 2 μm, but instead lines from other species absorb and reprocess much of the emission from [Te III]. The striking difference between the collision strength values, and their key role in accurate spectral modelling of KN is well illustrated by this example, which highlights the need for further high-quality atomic data, in particular pertaining to collision strengths and recombination rates. As the line blocking at low Y_e is dominated by lanthanides, it is also important to develop accurate model atoms for these in terms of energy levels and transitions probabilities.

Recent works on electron impact excitation have found that the Axelrod (1980) treatment may systematically underestimate collision strengths, while the accuracy of the van Regemorter (van Regemorter 1962) approximation varies depending on ion and electron temperature (Bromley et al. 2023, in the context of Pt). While this may lead to underestimated forbidden line emissivities in our models, as for the [Te III] line above, we believe that these lines do not play a dominant role in determining the overall temperature solution of the models and epochs studied here. In our models, we find that allowed transitions dominate both as emission and cooling channels, and thus the accuracy of our temperature solutions will depend mainly on the van Regemorter approximation, and hence on our line wavelengths and transition strengths. When measured values are available, we find that our calculated A-values are within an order of magnitude of these. The accuracy of the transition wavelengths is more variable, but we believe our theoretical values to be broadly accurate enough to yield reasonable temperature results. It is likely that forbidden lines play larger roles at later times when the ejecta become more optically thin, and such lines are expected to emit strongly (see e.g. Hotokezaka et al. 2022, 2023).

The increasing temperature, and the diminishing line blocking, leads to an overall 'red-to-blue' SED time evolution in the models during the 5–20 d period. However, the SED changes are quite mild, and the regular photometric colours stay relatively constant over this time period. We find that the AT2017gfo colour curves are similarly quite flat between 5 and 10 d (the last epoch at which colours are available), with only the NIR colours showing a noticeable reddening trend. Considering the broader spectral evolution by comparing the model fluxes in the optical to the NIR, we find this ratio to be monotonically increasing by a factor of ∼2–3 in the 5–20 d range depending on the model. The observations of AT2017gfo show a flat evolution between 5 and 10 d, and possibly a hint of decreasing trend from the last 10.4 d observation. Discrepancy in this trend may imply that single composition models (as used here) are not suitable of AT2017gfo, as many light-curve analyses have previously

indicated (e.g. Perego, Radice & Bernuzzi 2017; Rosswog et al. 2018; Tanaka et al. 2018; Waxman et al. 2018). However, verification of the accuracy of stationary radiation field models, as used here, at 5–10 d still needs to be firmly demonstrated, as diffusion may not have fully ended yet at these epochs.

We establish that time-dependent recombination and adiabatic cooling effects on our models are relatively minor, both with respect to the thermodynamic state, as well as the emergent spectra. The exception is the $Y_e \sim 0.35$ model, which obtains lower temperatures and a less ionized gas from 10 d onwards, with impact on the emergent spectra arising from 15 d onwards. The combination of low-power and low-density conditions previously identified in Pognan, Jerkstrand & Grumer (2022a) as maximizing time-dependent effects is thus confirmed here in a spectral context. Therefore, accurate modelling of an early, fast-moving, lanthanide-free ejecta component likely requires the inclusion of time-dependent effects in the NLTE calculations. We find that a few key spectral features may be significantly affected in the case of strong time-dependent effects, which may lead to incorrect deductions on the abundance of certain prominent species.

By combining several arguments and model properties, we can conclude that KN ejecta are not optically thin at least up to 20 d after merger, and that resonance scattering and fluorescence play key roles in KN spectral formation throughout the first weeks. The temperatures, which increase with time, and the high degree of line blocking in the blue, signify that much of the cooling emission cannot directly escape. Instead, the cooling emission experiences resonance scattering and fluorescence. One consequence of this is that the KN SED bears little relation to the gas temperature, implying that blackbody fits to the emergent spectrum have little physical meaning. These results also suggest that KNe evolve qualitatively differently to SNe, which have a clear transition to a thermal emission dominated nebular phase, followed by a much later fluorescence dominated phase. It is not yet completely clear how KNe evolve, whether they move directly to this fluorescence phase, or reach the thermal nebular phase later on. Further theoretical studies combined with late-time observations of nebular phase KNe are still required in order to fully elucidate the evolution of these transients.

ACKNOWLEDGEMENTS

We acknowledge funding from the European Research Council (ERC) under the European Union's Horizon 2020 Research and Innovation Program (ERC Starting Grant 803189 – SUPERSPEC, PI: Jerkstrand). JG thanks the Swedish Research Council for the individual starting grant with contract no. 2020-05467. The computations were enabled by resources provided by the National Academic Infrastructure for Supercomputing in Sweden (NAISS), and the Swedish National Infrastructure for Computing (SNIC), at the Parallelldatorcentrum (PDC) Center for High Performance Computing, Royal Institute of Technology (KTH), partially funded by the Swedish Research Council through grant agreements no. 2022-06725 and no. 2018-05973. We acknowledge also computing funding by the Swedish Research Council (grant 2018-03799, PI: Jerkstrand).

DATA AVAILABILITY

The data underlying this article will be shared on reasonable request to the corresponding author.

REFERENCES

Abbott B. P. et al., 2017, ApJ, 848, L12
Arcones A., Thielemann F.-K., 2023, A&AR, 31, 1
Axelrod T. S., 1980, PhD thesis, California University, Santa Cruz
Banerjee S., Tanaka M., Kawaguchi K., Kato D., Gaigalas G., 2020, ApJ, 901, 29
Banerjee S., Tanaka M., Kato D., Gaigalas G., Kawaguchi K., Domoto N., 2022, ApJ, 934, 117
Barnes J., Kasen D., Wu M.-R., Martínez-Pinedo G., 2016, ApJ, 829, 110
Barnes J., Zhu Y. L., Lund K. A., Sprouse T. M., Vassh N., McLaughlin G. C., Mumpower M. R., Surman R., 2021, ApJ, 918, 44
Biémont E., Palmeri P., Quinet P., 1999, Ap&SS, 269, 635
Blondin S. et al., 2022, A&A, 668, A163
Botyánszki J., Kasen D., 2017, ApJ, 845, 176
Bromley S. J. et al., 2020, ApJS, 250, 19
Bromley S. J., McCann M., Loch S. D., Ballance C. P., 2023, ApJS, 268, 22
Bulla M., 2019, MNRAS, 489, 5037
Bulla M., 2023, MNRAS, 520, 2558
Carvajal Gallego H., Palmeri P., Quinet P., 2021, MNRAS, 501, 1440
Carvajal Gallego H., Deprince J., Palmeri P., Quinet P., 2023, MNRAS, 522, 312
Collins C. E., Bauswein A., Sim S. A., Vijayan V., Martínez-Pinedo G., Just O., Shingles L. J., Kromer M., 2023, MNRAS, 521, 1858
Côté B. et al., 2019, ApJ, 875, 106
Deprince J., Carvajal Gallego H., Godefroid M., Goriely S., Palmeri P., Quinet P., 2023, Eur. Phys. J. D, 77, 93
Domoto N., Tanaka M., Wanajo S., Kawaguchi K., 2021, ApJ, 913, 26
Domoto N., Tanaka M., Kato D., Kawaguchi K., Hotokezaka K., Wanajo S., 2022, ApJ, 939, 8
Eichler D., Livio M., Piran T., Schramm D. N., 1989, Nature, 340, 126
Finstad D., De S., Brown D. A., Berger E., Biwer C. M., 2018, ApJ, 860, L2
Flörs A. et al., 2023, MNRAS, 524, 3083
Fontes C. J., Fryer C. L., Hungerford A. L., Wollaeger R. T., Korobkin O., 2020, MNRAS, 493, 4143
Fontes C. J., Fryer C. L., Wollaeger R. T., Mumpower M. R., Sprouse T. M., 2023, MNRAS, 519, 2862
Freiburghaus C., Rosswog S., Thielemann F. K., 1999, ApJ, 525, L121
Gaigalas G., Kato D., Rynkun P., Radžiūtė L., Tanaka M., 2019, ApJS, 240, 29
Gaigalas G., Rynkun P., Radžiūtė L., Kato D., Tanaka M., Jönsson P., 2020, ApJS, 248, 13
Gillanders J. H., McCann M., Sim S. A., Smartt S. J., Ballance C. P., 2021, MNRAS, 506, 3560
Gillanders J. H., Smartt S. J., Sim S. A., Bauswein A., Goriely S., 2022, MNRAS, 515, 631
Gillanders J. H., Sim S. A., Smartt S. J., Goriely S., Bauswein A., 2023, preprint (arXiv:2306.15055)
Gu M. F., 2008, Can. J. Phys., 86, 675
Hotokezaka K., Nakar E., 2020, ApJ, 891, 152
Hotokezaka K., Tanaka M., Kato D., Gaigalas G., 2021, MNRAS, 506, 5863
Hotokezaka K., Tanaka M., Kato D., Gaigalas G., 2022, MNRAS, 515, L89
Hotokezaka K., Tanaka M., Kato D., Gaigalas G., 2023, MNRAS, 526, L155
Jerkstrand A., 2011, PhD thesis, Department of Astronomy, Stockholm University
Jerkstrand A., 2017, Spectra of Supernovae in the Nebular Phase. Springer, Cham, p. 795
Jerkstrand A., Fransson C., Kozma C., 2011, A&A, 530, A45
Jerkstrand A., Fransson C., Maguire K., Smartt S., Ergon M., Spyromilio J., 2012, A&A, 546, A28
Jerkstrand A., Smartt S. J., Heger A., 2016, MNRAS, 455, 3207
Just O., Kullmann I., Goriely S., Bauswein A., Janka H. T., Collins C. E., 2022, MNRAS, 510, 2820
Kasen D., Barnes J., 2019, ApJ, 876, 128
Kasen D., Thomas R. C., Nugent P., 2006, ApJ, 651, 366
Kasen D., Badnell N. R., Barnes J., 2013, ApJ, 774, 25

Kasen D., Metzger B., Barnes J., Quataert E., Ramirez-Ruiz E., 2017, Nature, 551, 80
Kawaguchi K., Fujibayashi S., Shibata M., Tanaka M., Wanajo S., 2021, ApJ, 913, 100
Kawaguchi K., Fujibayashi S., Domoto N., Kiuchi K., Shibata M., Wanajo S., 2023, MNRAS, 525, 3384
Kozma C., Fransson C., 1992, ApJ, 390, 602
Kramida A., Ralchenko Yu., Reader J., NIST ASD Team, 2020, NIST Atomic Spectra Database (ver. 5.8). National Institute of Standards and Technology, Gaithersburg, MD, available at: https://physics.nist.gov/asd
Lawler J. E., Schmidt J. R., Hartog E. A. D., 2022, J. Quant. Spec. Radiat. Transfer, 289, 108283
Li L.-X., Paczyński B., 1998, ApJ, 507, L59
Lodders K., 2021, Space Sci. Rev., 217, 44
Lodders K., Palme H., Gail H. P., 2009, Solar System, Landolt Börnstein – Group VI Astronomy and Astrophysics, Vol. 4B. Springer-Verlag, Berlin, Heidelberg, p. 712
Longair M. S., 2011, High Energy Astrophysics. Cambridge Univ. Press, Cambridge
Lotz W., 1967, Z. Phys., 206, 205
McCann M., Bromley S., Loch S. D., Ballance C. P., 2022, MNRAS, 509, 4723
Madonna S. et al., 2018, ApJ, 861, L8
Margutti R., Chornock R., 2021, ARA&A, 59, 155
Martínez-Pinedo G. et al., 2007, Prog. Part. Nucl. Phys., 59, 199
Metzger B. D., 2019, Living Rev. Relativ., 23, 1
Metzger B. D. et al., 2010, MNRAS, 406, 2650
Moore C. E., 1971, Atomic Energy Levels as Derived from the Analysis of Optical Spectra – Chromium through Niobium. National Bureau of Standards, Washington, DC
Nedora V. et al., 2021, ApJ, 906, 98
Neuweiler A., Dietrich T., Bulla M., Chaurasia S. V., Rosswog S., Ujevic M., 2023, Phys. Rev. D, 107, 023016
Palmer B. A., 1977, PhD thesis, Purdue University, Indiana
Perego A., Radice D., Bernuzzi S., 2017, ApJ, 850, L37
Perego A. et al., 2022, ApJ, 925, 22
Pian E. et al., 2017, Nature, 551, 67
Pognan Q., Jerkstrand A., Grumer J., 2022a, MNRAS, 510, 3806
Pognan Q., Jerkstrand A., Grumer J., 2022b, MNRAS, 513, 5174
Prantzos N., Abia C., Cristallo S., Limongi M., Chieffi A., 2020, MNRAS, 491, 1832
Radžiūtė L., Gaigalas G., Kato D., Rynkun P., Tanaka M., 2020, ApJS, 248, 17
Rosswog S., Liebendörfer M., Thielemann F. K., Davies M. B., Benz W., Piran T., 1999, A&A, 341, 499
Rosswog S., Sollerman J., Feindt U., Goobar A., Korobkin O., Wollaeger R., Fremling C., Kasliwal M. M., 2018, A&A, 615, A132
Rutten R. J., 2003, Radiative Transfer in Stellar Atmospheres. Sterrekindig Instituut Utrecht, Utrecht, the Netherlands
Ryabchikova T., Piskunov N., Kurucz R. L., Stempels H. C., Heiter U., Pakhomov Y., Barklem P. S., 2015, Phys. Scr., 90, 054005
Rybicki G. B., Lightman A. P., 1979, Radiative Processes in Astrophysics. Wiley VCH, New York
Rynkun P., Banerjee S., Gaigalas G., Tanaka M., Radžiūtė L., Kato D., 2022, A&A, 658, A82
Shen K. J., Blondin S., Kasen D., Dessart L., Townsley D. M., Boos S., Hillier D. J., 2021, ApJ, 909, L18
Shibata M., Hotokezaka K., 2019, Annu. Rev. Nucl. Part. Sci., 69, 41
Shingles L. J. et al., 2020, MNRAS, 492, 2029
Shingles L. J. et al., 2023, ApJ, 954, L41
Shull J. M., van Steenberg M., 1982, ApJS, 48, 95
Simsarian J. E., Orozco L. A., Sprouse G. D., Zhao W. Z., 1998, Phys. Rev. A, 57, 2448
Smartt S. J. et al., 2017, Nature, 551, 75
Sneppen A., Watson D., 2023, A&A, 675, A194
Spencer L. V., Fano U., 1954, Phys. Rev., 93, 1172
Symbalisty E., Schramm D. N., 1982, Astrophys. Lett., 22, 143
Tanaka M., Hotokezaka K., 2013, ApJ, 775, 113
Tanaka M. et al., 2017, PASJ, 69, 102
Tanaka M. et al., 2018, ApJ, 852, 109
Tanaka M., Kato D., Gaigalas G., Kawaguchi K., 2020, MNRAS, 496, 1369
Tanvir N. R. et al., 2017, ApJ, 848, L27
Tarumi Y., Hotokezaka K., Domoto N., Tanaka M., 2023, preprint (arXiv:2302.13061)
Troja E. et al., 2017, Nature, 551, 71
van Regemorter H., 1962, ApJ, 136, 906
Vieira N., Ruan J. J., Haggard D., Ford N., Drout M. R., Fernández R., Badnell N. R., 2023, ApJ, 944, 123
Villar V. A. et al., 2017, ApJ, 851, L21
Volz U., Schmoranzer H., 1996, Phys. Scr., T65, 48
Wanajo S., 2018, ApJ, 868, 65
Wanajo S., Sekiguchi Y., Nishimura N., Kiuchi K., Kyutoku K., Shibata M., 2014, ApJ, 789, L39
Watson D. et al., 2019, Nature, 574, 497
Waxman E., Ofek E. O., Kushnir D., Gal-Yam A., 2018, MNRAS, 481, 3423
Waxman E., Ofek E. O., Kushnir D., 2019, ApJ, 878, 93
Wollaeger R. T. et al., 2018, MNRAS, 478, 3298
Wollaeger R. T. et al., 2021, ApJ, 918, 10

APPENDIX A: MODEL COMPOSITION AND ENERGY DEPOSITION

In this appendix, we present the exact compositions of our three models, as well as the $Y_e \sim 0.35$ model without Sr in Table A1. We also show the equations used for the thermalization of the radioactive decay products in equations (A1)–(A8), taken from Barnes et al. (2016), Kasen & Barnes (2019), and Waxman, Ofek & Kushnir (2019). The additional consideration to β-decay from Waxman, Ofek & Kushnir (2019) is reflected in the exponent of -1.5 for the thermalization fraction of β-decay electrons (equation A2). The total energy depositions by model, with each product's contribution can be visualized in Fig. A1.

$$f_\alpha = \left(1 + \frac{t}{t_\alpha}\right)^{-1.5}, \tag{A1}$$

$$f_\beta = \left(1 + \frac{t}{t_e}\right)^{-1.5}, \tag{A2}$$

$$f_\gamma = \left(1 - e^{-\left(\frac{t_\gamma}{t}\right)^2}\right), \tag{A3}$$

$$f_{\rm SF} = \frac{\ln\left(1+2\left(\frac{t}{t_{\rm SF}}\right)^2\right)}{2\left(\frac{t}{t_{\rm SF}}\right)^2}, \tag{A4}$$

$$t_\alpha = 38.7 \left(\frac{M_{\rm zone}}{0.01 {\rm M}_\odot}\right)^{2/3} \left(\frac{v_{\rm zone}}{0.2{\rm c}}\right)^{-2} {\rm d}, \tag{A5}$$

$$t_\beta = 12.9 \left(\frac{M_{\rm zone}}{0.01\,{\rm M}_\odot}\right)^{2/3} \left(\frac{v_{\rm zone}}{0.2{\rm c}}\right)^{-2} {\rm d}, \tag{A6}$$

$$t_\gamma = 0.3 \left(\frac{M_{\rm zone}}{0.01\,{\rm M}_\odot}\right)^{1/2} \left(\frac{v_{\rm zone}}{0.2{\rm c}}\right)^{-1} {\rm d}, \tag{A7}$$

$$t_{\rm SF} = 16.77 \left(\frac{M_{\rm zone}}{0.005\,{\rm M}_\odot}\right)^{1/2} \left(\frac{v_{\rm zone}}{0.2{\rm c}}\right)^{-1.5} {\rm d}. \tag{A8}$$

Table A1. Model compositions by mass fractions. The horizontal lines indicate separations between groups of elements, e.g. light elements, first r-process peak, second r-process peak, lanthanides, third r-process peak, and actinides.

Element	$Y_e \sim 0.35$	$Y_e \sim 0.35$, no Sr	$Y_e \sim 0.25$	$Y_e \sim 0.15$
^{22}Ti	0.0006	0.0007	–	–
^{23}V	0.0005	0.0006	–	–
^{24}Cr	0.0119	0.0147	–	–
^{25}Mn	0.0009	0.0011	–	–
^{26}Fe	0.0258	0.0319	–	–
^{27}Co	0.0004	0.0005	–	–
^{28}Ni	0.0240	0.0297	–	–
^{29}Cu	0.0079	0.0098	–	–
^{30}Zn	0.0106	0.0131	0.0249	–
^{31}Ga	0.0025	0.0032	0.0112	–
^{32}Ge	0.0095	0.0118	0.0519	–
^{33}As	0.0008	0.0010	–	–
^{34}Se	0.1272	0.1570	0.1269	–
^{35}Br	0.0241	0.0298	0.0207	–
^{36}Kr	0.2638	0.3256	0.0909	–
^{37}Rb	0.1033	0.1276	0.0304	–
^{38}Sr	0.1898	–	0.0375	–
^{39}Y	0.0261	0.0322	0.0058	–
^{40}Zr	0.1105	0.1364	0.0749	0.0151
^{41}Nb	0.0007	0.0009	–	–
^{42}Mo	0.0220	0.0271	0.0235	–
^{44}Ru	0.0252	0.0311	0.0395	0.0099
^{45}Rh	0.0007	0.0008	–	–
^{46}Pd	0.0059	0.0073	0.0283	–
^{47}Ag	0.0008	0.0010	0.0096	–
^{48}Cd	0.0023	0.0029	0.0542	0.0125
^{49}In	0.0003	0.0003	0.0077	–
^{50}Sn	0.0013	0.0016	0.1749	0.0937
^{51}Sb	0.0003	0.0003	0.0424	0.0216
^{52}Te	–	–	0.0573	0.0730
^{53}I	–	–	0.0428	0.0388
^{54}Xe	–	–	0.0179	0.0551
^{55}Cs	–	–	0.0092	0.0338
^{56}Ba	–	–	0.0018	–
^{58}Ce	–	–	0.0029	0.0179
^{60}Nd	–	–	0.0039	0.0289
^{62}Sm	–	–	0.0022	0.0218
^{63}Eu	–	–	0.0016	0.0204
^{64}Gd	–	–	0.0023	0.0365
^{65}Tb	–	–	–	0.0148
^{66}Dy	–	–	0.0019	0.0430
^{68}Er	–	–	0.0010	0.0334
^{69}Tm	–	–	–	0.0132
^{70}Yb	–	–	–	0.0221
^{72}Hf	–	–	–	0.0228
^{73}Ta	–	–	–	0.0925
^{75}Re	–	–	–	0.0343
^{76}Os	–	–	–	0.1573
^{77}Ir	–	–	–	0.0361
^{78}Pt	–	–	–	0.0368
^{79}Au	–	–	–	0.0088
^{82}Pb	–	–	–	0.0023
^{83}Bi	–	–	–	0.0008
^{90}Th	–	–	–	0.0013
^{92}U	–	–	–	0.0015

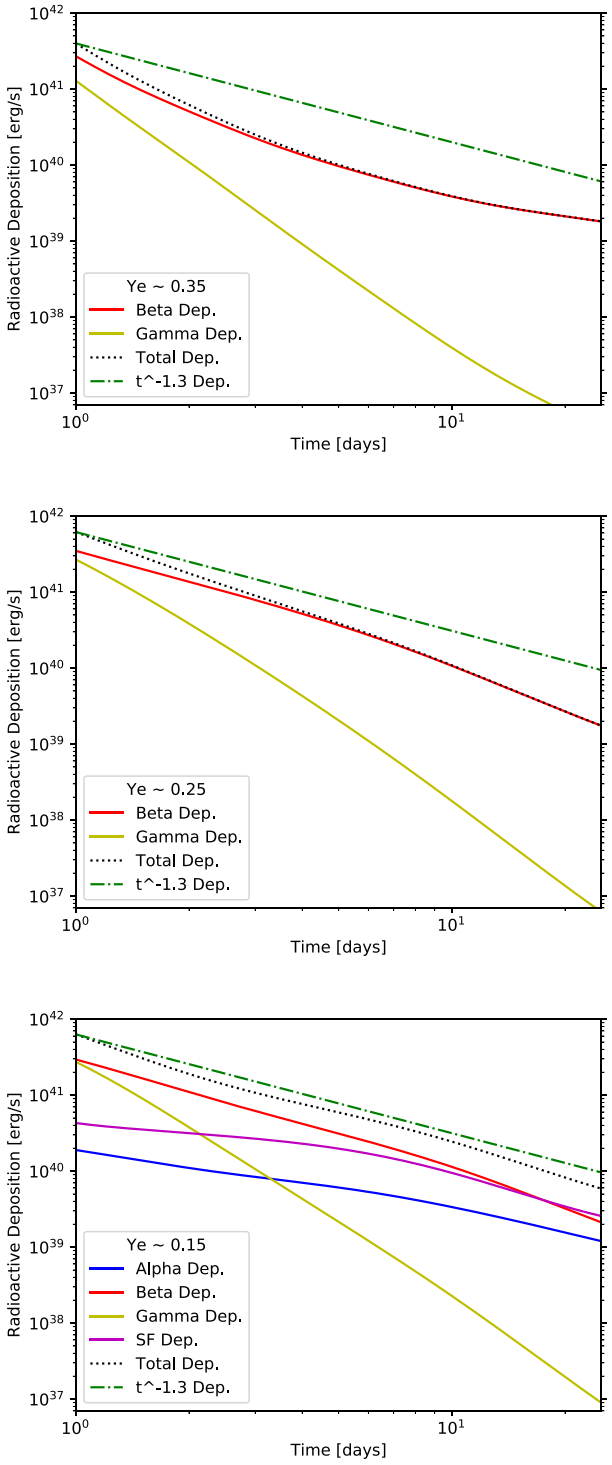

Figure A1. The energy deposition to the spectral simulation separated by decay product, and calculated consistently with the evolution of composition shown in Fig. 1. The canonical $t^{-1.3}$ power law is shown to illustrate the importance of thermalization and the thermalization break. We note that only the $Y_e \sim 0.15$ model has significant alpha decay and spontaneous fission contributions.

APPENDIX B: ADDITIONAL PLOTS

This appendix collects additional plots of auxiliary utility to the main body of the paper. In Fig. B1, we show the thermodynamic evolution of our models in terms of profiles, e.g. layer slices. This provides an alternative visualization to Fig. 2, and notably shows the changes in stratification of the ejecta in the $Y_e \sim 0.35$, 0.25 models as time progresses.

We also show a detailed visualization of time-dependent effects on the individual species of the $Y_e \sim 0.35$ model at 20 d after merger, when the time-dependent effects are strongest, in Fig. B2.

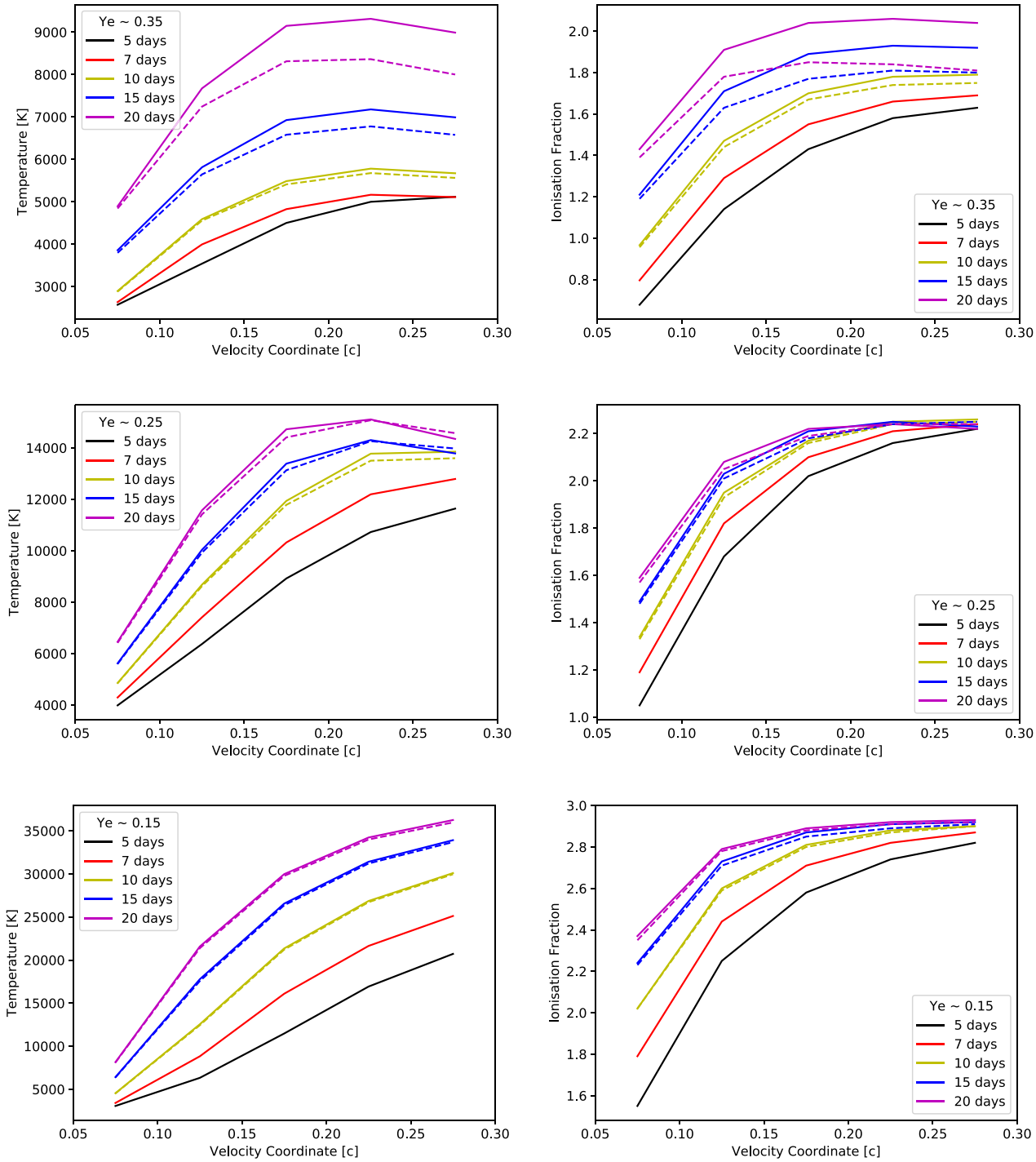

Figure B1. The temperature and ionization structure profiles of the models. The time-dependent solutions are indicated by the dashed lines. Note that time-dependent mode is only run from 10 d onwards.

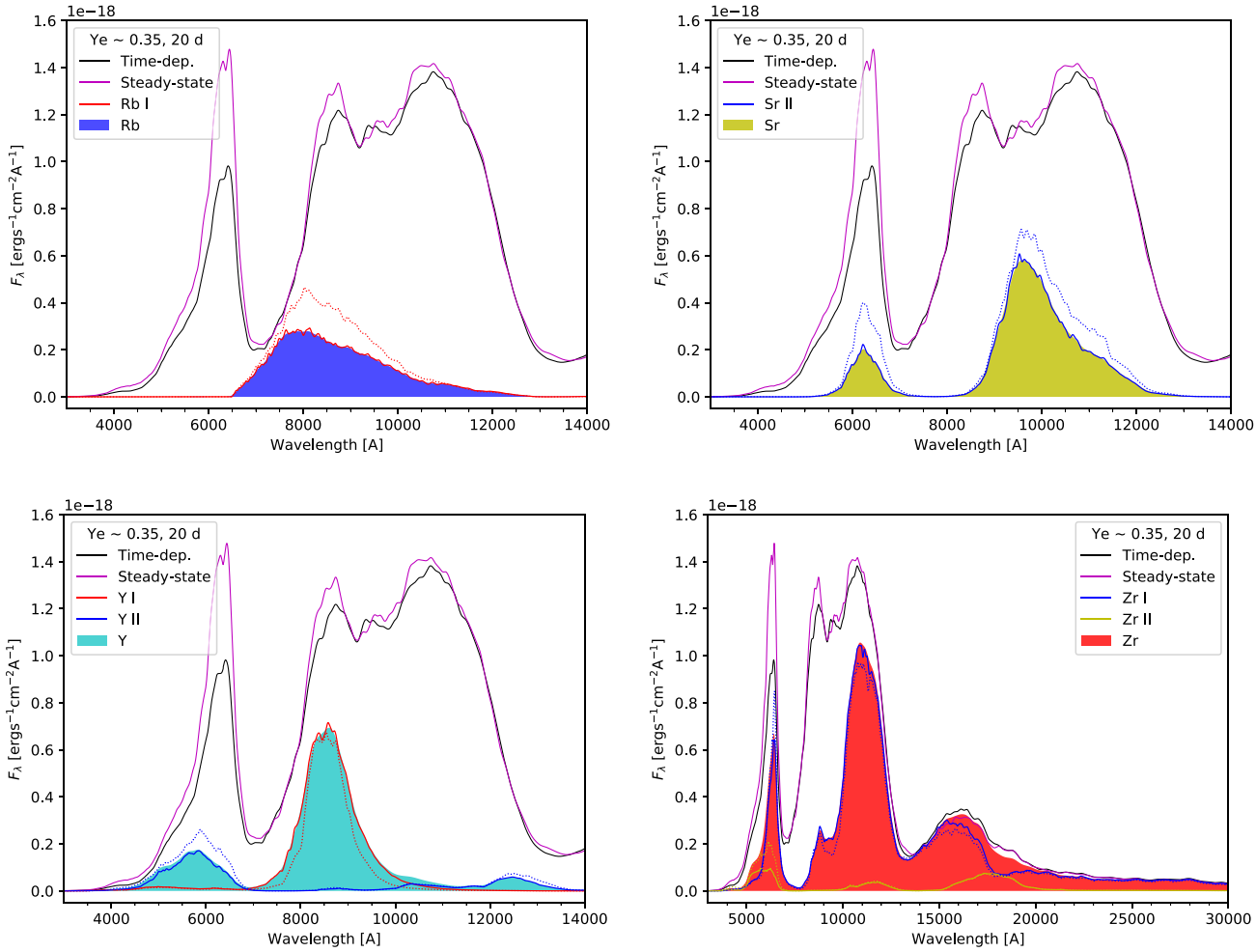

Figure B2. Individual contributions of Rb, Sr, Y, and Zr for the high Y_e model at 20 d. Time-dependent effects are shown by comparing the time-dependent spectrum (black) to the steady-state spectrum (magenta), as well as the effect on the individual species (solid for time-dependent, dotted for steady-state). The filled areas are the total elemental contribution in the time-dependent solution. Note that the x-axis is scaled differently for each element, to focus on the wavelength ranges where they contribute the most to the spectrum.

APPENDIX C: ATOMIC DATA

This part of the appendix gives information on the fundamental parameters used in the atomic structure calculations, most importantly the scope of included spectroscopic configurations. The information is summarized in Table C1. The first to third columns (Z, El, and Sp) define the atomic number, the element name, and the ionic spectrum designation. The fourth ($E_{\rm i}^{\rm NIST}$) gives the (first) ionization energy as listed by the NIST ASD (Kramida et al. 2020) in units of eV. The fifth to seventh ($n_{\rm lev}$, $n_{\rm lev}^{\rm red}$, and $n_{\rm trans}$) specify the number of computed fine-structure levels, the number of such levels below the $E_{\rm i}^{\rm NIST}$ ionization energy, and, finally, the total number of allowed and forbidden transitions between the $n_{\rm trans}$ levels (with different multipole contributions summed up for each line). The eighth column ($n_{\rm opt}^{\rm cfg}$) specifies how many configurations that were included in the Dirac–Fock–Slater optimization of the common central, screening potential in the order of the configurations in the following columns (i.e. a '2' implies that the ground configuration and the first excited configuration was used in the optimization). Finally, columns 9 and 10 ('Ground conf.' and 'Additional configurations') contains the ground and excited configurations included in the atomic model applied to each ion.

Table C1. Fundamental atomic parameters defining the atomic structure calculations. See Appendix C for further information and definitions.

Z	El	Sp	E_i^{NIST} (eV)	n_{lev}	n_{lev}^{red}	n_{trans}	n_{opt}^{cfg}	Ground conf.	Additional configurations
26	Fe	I	7.9024681	3195	667	153526	1	3d6 4s2	3d8, 3d7 4s1, 3d6 4s1 4p1, 3d7 4p1, 3d5 4s2 4p1, 3d6 4s1 5s1, 3d7 5s1, 3d6 4s1 5p1, 3d6 4s1 4d1, 3d7 5p1, 3d7 4d1, 3d6 4s1 6s1, 3d7 6s1, 3d6 4s1 6p1, 3d6 4s1 5d1
		II	16.1992	3467	1647	901922	2	3d6 4s1	3d7, 3d5 4s2, 3d6 4p1, 3d5 4s1 4p1, 3d6 5s1, 3d6 4d1, 3d6 5p1, 3d6 6s1, 3d6 4f1, 3d5 4s1 5s1, 3d6 5d1, 3d6 6p1, 3d5 4p2, 3d5 4s1 4d1, 3d6 7s1
		III	30.651	2338	1853	1108723	1	3d6	3d5 4s1, 3d5 4p1, 3d5 4d1, 3d5 5s1, 3d5 5p1, 3d5 4f1, 3d4 4s1 4p1, 3d5 5d1, 3d5 6s1, 3d5 6p1
		IV	54.91	736	730	190780	1	3d5	3d4 4s1, 3d4 4p1, 3d3 4s1 4p1, 3d4 5s1, 3d4 5p1
27	Co	I	7.88101	778	423	64859	3	3p6 3d7 4s2	3p6 3d8 4s1, 3p6 3d9, 3p6 3d7 4s1 4p1, 3p6 3d8 4p1, 3p6 3d8 5s1, 3p6 3d7 4s1 5s1, 3p6 3d8 4d1, 3p6 3d7 4s1 4d1
		II	17.0844	905	721	177823	1	3p6 3d8	3p6 3d7 4s1, 3p6 3d6 4s2, 3p6 3d7 4p1, 3p6 3d6 4s1 4p1, 3p6 3d7 5s1, 3p6 3d7 4d1, 3p6 3d7 5p1, 3p6 3d7 6s1
		III	33.5	601	596	122474	1	3p6 3d7	3p6 3d6 4s1, 3p6 3d6 4p1, 3p6 3d6 4d1, 3p6 3d6 5s1
		IV	51.27	1088	975	318197	1	3p6 3d6	3p6 3d5 4s1, 3p6 3d5 4p1, 3p6 3d4 4s1 4p1, 3p6 3d5 4d1, 3p6 3d5 5s1
28	Ni	I	7.639878	236	156	9661	3	3p6 3d8 4s2	3p6 3d9 4s1, 3p6 3d9 4p1, 3p6 3d10, 3p6 3d8 4s1 4p1, 3p6 3d9 5s1, 3p6 3d8 4s1 5s1, 3p6 3d9 5p1, 3p6 3d9 4d1, 3p6 3d9 6s1, 3p6 3d9 6p1, 3p6 3d9 5d1, 3p6 3d9 4f1
		II	18.168838	587	519	97570	1	3p6 3d9	3p6 3d8 4s1, 3p6 3d7 4s2, 3p6 3d8 4p1, 3p6 3d7 4s1 4p1, 3p6 3d8 5s1, 3p6 3d8 4d1, 3p6 3d8 5p1, 3p6 3d8 6s1, 3p6 3d8 4f1, 3p6 3d8 5d1
		III	35.187	867	825	235160	1	3p6 3d8	3p6 3d7 4s1, 3p6 3d7 4p1, 3p6 3d6 4s2, 3p6 3d7 4d1, 3p6 3d7 5s1, 3p6 3d7 5p1, 3p6 3d6 4s1 4p1
		IV	54.92	818	818	232957	1	3p6 3d7	3p6 3d6 4s1, 3p6 3d6 4p1, 3p6 3d5 4s2, 3p6 3d6 4d1, 3p6 3d6 5s1, 3p6 3d6 5p1
29	Cu	I	7.72638	38	32	449	3	3p6 3d10 4s1	3p6 3d9 4s2, 3p6 3d10 4p1, 3p6 3d9 4s1 4p1, 3p6 3d10 5s1, 3p6 3d10 5p1, 3p6 3d10 4d1, 3p6 3d10 6s1, 3p6 3d10 6p1, 3p6 3d10 5d1
		II	20.29239	204	193	14480	1	3p6 3d10	3p6 3d9 4s1, 3p6 3d9 4p1, 3p6 3d8 4s2, 3p6 3d8 4s1 4p1, 3p6 3d9 5s1, 3p6 3d9 4d1, 3p6 3d9 5p1, 3p6 3d9 6s1, 3p6 3d9 4f1, 3p6 3d9 5d1, 3p6 3d9 6p1
		III	36.841	587	565	116015	1	3p6 3d9	3p6 3d8 4s1, 3p6 3d8 4p1, 3p6 3d7 4s2, 3p6 3d8 5s1, 3p6 3d8 4d1, 3p6 3d8 5p1, 3p6 3d7 4s1 4p1, 3p6 3d8 4f1, 3p6 3d8 6s1, 3p6 3d8 5d1
		IV	57.38	397	397	54954	1	3p6 3d8	3p6 3d7 4s1, 3p6 3d7 4p1, 3p6 3d7 4d1, 3p6 3d6 4s2, 3p6 3d7 5s1
30	Zn	I	9.394197	29	29	348	1	3p6 3d10 4s2	3p6 3d10 4s1 4p1, 3p6 3d10 4s1 5s1, 3p6 3d10 4s1 5p1, 3p6 3d10 4s1 4d1, 3p6 3d10 4s1 6s1, 3p6 3d10 4s1 6p1, 3p6 3d10 4s1 5d1, 3p6 3d10 4s1 4f1
		II	17.96439	40	36	564	1	3p6 3d10 4s1	3p6 3d10 4p1, 3p6 3d9 4s2, 3p6 3d10 5s1, 3p6 3d10 4d1, 3p6 3d10 5p1, 3p6 3d9 4s1 4p1, 3p6 3d10 6s1, 3p6 3d10 4f1, 3p6 3d10 5d1, 3p6 3d10 6p1
		III	39.7233	150	149	8624	1	3p6 3d10	3p6 3d9 4s1, 3p6 3d9 4p1, 3p6 3d8 4s2, 3p6 3d9 4d1, 3p6 3d9 5s1, 3p6 3d9 5p1, 3p6 3d8 4s1 4p1
		IV	59.573	382	382	52015	1	3p6 3d9	3p6 3d8 4s1, 3p6 3d8 4p1, 3p6 3d8 4d1, 3p6 3d8 5p1, 3p6 3d8 4f1, 3p6 3d8 6p1, 3p6 3d8 5f1
31	Ga	I	5.999302	22	17	130	1	3d10 4s2 4p1	3d10 4s2 5s1, 3d10 4s2 5p1, 3d10 4s2 4d1, 3d10 4s2 6s1, 3d10 4s1 4p2, 3d10 4s2 6p1, 3d10 4s2 5d1, 3d10 4s2 4f1
		II	20.51514	26	26	290	1	3d10 4s2	3d10 4s1 4p1, 3d10 4s1 5s1, 3d10 4p2, 3d10 4s1 4d1, 3d10 4s1 5p1, 3d10 4s1 6s1, 3d10 4s1 5d1
		III	30.72576	12	12	62	1	3d10 4s1	3d10 4p1, 3d9 4s2, 3d10 5s1, 3d10 4d1, 3d10 5p1, 3d10 4f1
		IV	63.241	51	51	1087	1	3d10	3d9 4s1, 3d9 4p1, 3d9 4d1, 3d9 5s1, 3d9 5p1
32	Ge	I	7.899435	79	72	2182	2	3d10 4s2 4p2	3d10 4s1 4p3, 3d10 4s2 4p1 5s1, 3d10 4s2 4p1 5p1, 3d10 4s2 4p1 4d1, 3d10 4s2 4p1 6s1, 3d10 4s2 4p1 6p1, 3d10 4s2 4p1 5d1, 3d10 4s2 4p1 4f1
		II	15.93461	22	22	223	1	3d10 4s2 4p1	3d10 4s1 4p2, 3d10 4s2 5s1, 3d10 4s2 5p1, 3d10 4s2 4d1, 3d10 4s2 6s1, 3d10 4s2 5d1, 3d10 4s2 4f1, 3d10 4s2 6p1
		III	34.0576	32	32	412	1	3d10 4s2	3d10 4s1 4p1, 3d10 4p2, 3d10 4s1 5s1, 3d10 4s1 4d1, 3d10 4s1 5p1, 3d10 4s1 4f1, 3d10 4s1 6s1, 3d10 4s1 5d1, 3d10 4s1 7s1
		IV	45.7155	15	15	100	1	3d10 4s1	3d10 4p1, 3d10 4d1, 3d10 5s1, 3d10 5p1, 3d10 4f1, 3d9 4s2, 3d10 5d1, 3d10 6s1
33	As	I	9.78855	99	78	2757	1	3d10 4s2 4p3	3d10 4s2 4p2 5s1, 3d10 4s1 4p4, 3d10 4s2 4p2 5p1, 3d10 4s2 4p2 4d1, 3d10 4s2 4p2 6s1, 3d10 4s2 4p2 6p1
		II	18.5892	67	67	1989	1	3d10 4s2 4p2	3d10 4s1 4p3, 3d10 4s2 4p1 5s1, 3d10 4s2 4p1 4d1, 3d10 4s2 4p1 5p1, 3d10 4s2 4p1 6s1, 3d10 4s2 4p1 5d1, 3d10 4s2 4p1 6p1
		III	28.349	25	25	290	1	3d10 4s2 4p1	3d10 4s1 4p2, 3d10 4s2 5s1, 3d10 4s2 4d1, 3d10 4s2 5p1, 3d10 4p3, 3d10 4s2 6s1, 3d10 4s2 4f1, 3d10 4s2 5d1
		IV	50.15	30	30	365	1	3d10 4s2	3d10 4s1 4p1, 3d10 4s1 4d1, 3d10 4p2, 3d10 4s1 5s1, 3d10 4s1 5p1, 3d10 4s1 4f1, 3d10 4s1 5d1, 3d10 4s1 6s1
34	Se	I	9.752392	157	120	6030	1	4s2 4p4	4s2 4p3 5s1, 4s2 4p3 5p1, 4s2 4p3 4d1, 4s2 4p3 6s1, 4s2 4p3 6p1, 4s2 4p3 5d1
		II	21.196	78	78	2758	1	4s2 4p3	4s1 4p4, 4s2 4p2 5s1, 4s2 4p2 5p1, 4s2 4p2 6s1, 4s2 4p2 5d1
		III	31.697	57	57	1432	1	4s2 4p2	4s1 4p3, 4s2 4p1 4d1, 4s2 4p1 5s1, 4s2 4p1 5p1, 4s2 4p1 6s1, 4s2 4p1 5d1
		IV	42.947	20	20	190	1	4s2 4p1	4s1 4p2, 4s2 4d1, 4s2 5s1, 4p3, 4s2 5p1
35	Br	I	11.81381	117	109	5256	1	4s2 4p5	4s2 4p4 5s1, 4s2 4p4 5p1, 4s2 4p4 4d1, 4s2 4p4 6s1, 4s1 4p6, 4s2 4p4 6p1, 4s2 4p4 5d1
		II	21.591	173	172	11816	1	4s2 4p4	4s2 4p3 5s1, 4s1 4p5, 4s2 4p3 4d1, 4s2 4p3 5p1, 4s2 4p3 6s1, 4s2 4p3 5d1, 4s2 4p3 4f1
		III	34.871	106	106	5005	1	4s2 4p3	4s1 4p4, 4s2 4p2 4d1, 4s2 4p2 5s1, 4s2 4p2 5p1, 4s2 4p2 5d1, 4s2 4p2 6s1
		IV	47.782	45	45	898	1	4s2 4p2	4s1 4p3, 4s2 4p1 4d1, 4s2 4p1 5s1, 4s2 4p1 5p1, 4s2 4p1 6s1
36	Kr	I	13.9996053	53	53	1216	1	4s2 4p6	4s2 4p5 5s1, 4s2 4p5 5p1, 4s2 4p5 4d1, 4s2 4p5 6s1, 4s2 4p5 6p1, 4s2 4p5 5d1
		II	24.35984	147	147	9115	1	4s2 4p5	4s1 4p6, 4s2 4p4 5s1, 4s2 4p4 4d1, 4s2 4p4 5p1, 4s2 4p4 6s1, 4s2 4p4 5d1, 4s2 4p4 6p1, 4s2 4p4 4f1
		III	35.838	172	171	12169	1	4s2 4p4	4s1 4p5, 4s2 4p3 4d1, 4s2 4p3 5s1, 4s2 4p3 5p1, 4s2 4p3 6s1, 4s2 4p3 5d1, 4s2 4p3 6d1, 4p6
		IV	50.85	106	106	5005	1	4s2 4p3	4s1 4p4, 4s2 4p2 4d1, 4s2 4p2 5s1, 4s2 4p2 5p1, 4s2 4p2 5d1, 4s2 4p2 6s1
37	Rb	I	4.177128	17	17	130	1	4s2 4p6 5s1	4s2 4p6 5p1, 4s2 4p6 4d1, 4s2 4p6 6s1, 4s2 4p6 6p1, 4s2 4p6 5d1, 4s2 4p6 7s1, 4s2 4p6 4f1, 4s2 4p6 7p1, 4s2 4p6 6d1
		II	27.28954	93	93	3564	1	4s2 4p6	4s2 4p5 5s1, 4s2 4p5 4d1, 4s2 4p5 5p1, 4s2 4p5 6s1, 4s2 4p5 5d1, 4s2 4p5 6p1, 4s2 4p5 4f1, 4s2 4p5 7s1, 4s2 4p5 6d1, 4s2 4p5 5f1
		III	39.247	96	96	4052	1	4s2 4p5	4s1 4p6, 4s2 4p4 4d1, 4s2 4p4 5s1, 4s2 4p4 5p1, 4s2 4p4 6s1, 4s2 4p4 5d1
		IV	52.2	133	133	7422	1	4s2 4p4	4s1 4p5, 4s2 4p3 4d1, 4s2 4p3 5s1, 4s2 4p3 5p1, 4s2 4p3 5d1, 4s2 4p3 6s1
38	Sr	I	5.6948674	50	46	907	1	4s2 4p6 5s2	4s2 4p6 5s1 5p1, 4s2 4p6 5s1 4d1, 4s2 4p6 5s1 6s1, 4s2 4p6 4d1 5p1, 4s2 4p6 5s1 6p1, 4s2 4p6 5s1 5d1, 4s2 4p6 5p2, 4s2 4p6 5s1 7s1, 4s2 4p6 5s1 4f1, 4s2 4p6 5s1 7p1, 4s2 4p6 5s1 6d1

Table C1 – *continued*

Z	El	Sp	E_i^{NIST} (eV)	n_{lev}	n_{lev}^{red}	n_{trans}	n_{opt}^{cfg}	Ground conf.	Additional configurations
		II	11.0302764	27	27	190	1	4s2 4p6 5s1	4s2 4p6 4d1, 4s2 4p6 5p1, 4s2 4p6 6s1, 4s2 4p6 5d1, 4s2 4p6 6p1, 4s2 4p6 4f1, 4s2 4p6 7s1, 4s2 4p6 6d1, 4s2 4p6 7p1, 4s2 4p6 5f1, 4s2 4p6 5g1
		III	42.88353	65	65	1749	1	4s2 4p6	4s2 4p5 4d1, 4s2 4p5 5s1, 4s2 4p5 5p1, 4s2 4p5 5d1, 4s2 4p5 6s1, 4s2 4p5 4f1, 4s2 4p5 6p1
		IV	56.28	118	118	5765	1	4s2 4p5	4s1 4p6, 4s2 4p4 4d1, 4s2 4p4 5s1, 4s2 4p4 5p1, 4s2 4p4 5d1, 4s2 4p4 4f1
39	Y	I	6.21726	128	111	5423	1	4p6 4d1 5s2	4p6 5s2 5p1, 4p6 4d2 5s1, 4p6 4d1 5s1 5p1, 4p6 4d2 5p1, 4p6 4d3, 4p6 5s2 6s1, 4p6 4d1 5s1 6s1, 5p2 4p6 5s1, 4p6 5s2 5d1, 4p6 5s2 6p1
		II	12.2236	99	99	3800	1	4p6 5s2	4p6 4d1 5s1, 4p6 4d2, 4p6 5s1 5p1, 4p6 4d1 5p1, 4p6 4d1 6s1, 4p6 5s1 6s1, 4p6 4d1 5d1, 4p6 5p2, 4p6 4d1 6p1, 4p6 5s1 5d1, 4p6 5s1 6p1, 4p6 4d1 4f1
		III	20.52441	17	17	126	1	4p6 4d1	4p6 5s1, 4p6 5p1, 4p6 6s1, 4p6 5d1, 4p6 6p1, 4p6 4f1, 4p6 7s1, 4p6 6d1, 4p6 5f1
		IV	60.6072	65	65	1749	1	4p6	4p5 4d1, 4p5 5s1, 4p5 5p1, 4p5 5d1, 4p5 4f1, 4p5 6s1, 4p5 6p1
40	Zr	I	6.63412	788	599	131460	1	4p6 4d2 5s2	4p6 4d3 5s1, 4p6 4d2 5s1 5p1, 4p6 4d1 5s2 5p1, 4p6 4d4, 4p6 4d3 5p1, 4p6 4d2 5s1 6s1, 4p6 4d2 5s1 6p1, 4p6 4d2 5s1 5d1, 4p6 4d3 6s1, 4p6 4d2 5p2, 4p6 4d2 5s1 7p1
		II	13.13	188	188	13747	1	4p6 4d2 5s1	4p6 4d3, 4p6 4d1 5s2, 4p6 4d2 5p1, 4p6 4d1 5s1 5p1, 4p6 4d2 6s1, 4p6 4d2 5d1
		III	23.17	84	84	2728	1	4p6 4d2	4p6 4d1 5s1, 4p6 5s2, 4p6 4d1 5p1, 4p6 5s1 5p1, 4p6 4d1 5d1, 4p6 4d1 6s1, 4p6 4d1 6p1, 4p6 4d1 4f1
		IV	34.41836	14	14	87	1	4p6 4d1	4p6 5s1, 4p6 5p1, 4p6 5d1, 4p6 6s1, 4p6 4f1, 4p6 6p1, 4p6 6d1
41	Nb	I	6.75885	649	513	93849	3	4d4 5s1	4d3 5s2, 4d5, 4d3 5s1 5p1, 4d4 5p1, 4d4 6s1, 4d3 5s1 6s1
		II	14.32	487	486	83641	3	4d4	4d3 5s1, 4d2 5s2, 4d3 5p1, 4d2 5s1 5p1, 4d3 6s1, 4d3 5d1
		III	25.04	188	188	13747	1	4d3	4d2 5s1, 4d2 5p1, 4d1 5s2, 4d1 5s1 5p1, 4d2 5d1, 4d2 6s1
		IV	37.611	52	52	1086	1	4d2	4d1 5s1, 4d1 5p1, 5s2, 5s1 5p1, 4d1 5d1, 4d1 6s1
42	Mo	I	7.09243	1654	401	54542	1	4d5 5s1	4d4 5s2, 4d6, 4d5 5p1, 4d4 5s1 5p1, 4d5 6s1, 4d5 5d1, 4d5 7s1, 4d4 5s1 6s1, 4d5 6d1
		II	16.16	851	832	242182	1	4d5	4d4 5s1, 4d4 5p1, 4d3 5s2, 4d3 5s1 5p1, 4d4 6s1, 4d4 5d1
		III	27.13	487	487	83833	1	4d4	4d3 5s1, 4d3 5p1, 4d2 5s2, 4d2 5s1 5p1, 4d3 6s1, 4d3 5d1
		IV	40.33	188	188	13747	1	4d3	4d2 5s1, 4d2 5p1, 4d1 5s2, 4d1 5s1 5p1, 4d2 6s1, 4d2 5d1
43	Tc	I	7.11938	2026	486	81950	1	4d5 5s2	4d6 5s1, 4d7, 4d5 5s1 5p1, 4d6 5p1, 4d5 5s1 6s1, 4d6 6s1, 4d5 5s1 5d1, 4d6 5d1, 4d6 6p1
		II	15.26	1122	993	331124	2	4d5 5s1	4d6, 4d5 5p1, 4d4 5s2, 4d4 5s1 5p1, 4d5 6s1, 4d5 5d1
		III	29.55	851	851	253888	1	4d5	4d4 5s1, 4d4 5p1, 4d3 5s2, 4d3 5s1 5p1, 4d4 6s1, 4d4 5d1
		IV	41	487	487	83833	1	4d4	4d3 5s1, 4d3 5p1, 4d2 5s2, 4d2 5s1 5p1, 4d3 6s1, 4d3 5d1
44	Ru	I	7.3605	1545	630	133998	3	4d7 5s1	4d6 5s2, 4d8, 4d6 5s1 5p1, 4d7 5p1, 4d7 6s1, 4d7 6p1, 4d7 5d1, 4d6 5s1 6s1, 4d6 5s1 5d1
		II	16.76	1472	1006	350226	1	4d7	4d6 5s1, 4d5 5s2, 4d6 5p1, 4d5 5s1 5p1, 4d6 6s1, 4d6 5d1, 4d5 5s1 6p1
		III	28.47	728	727	177431	1	4d6	4d5 5s1, 4d5 5p1, 4d5 5d1, 4d5 6s1
		IV	45	851	851	253887	1	4d5	4d4 5s1, 4d4 5p1, 4d3 5s2, 4d3 5s1 5p1, 4d4 6s1, 4d4 5d1
45	Rh	I	7.4589	98	94	3494	3	4d8 5s1	4d9, 4d8 5p1, 4d7 5s2, 4d8 6s1
		II	18.08	339	339	41465	1	4d8	4d7 5s1, 4d7 5p1, 4d6 5s2, 4d7 6s1, 4d7 6p1
		III	31.06	818	816	231952	1	4d7	4d6 5s1, 4d6 5p1, 4d5 5s2, 4d6 5d1, 4d6 6s1, 4d6 6p1
		IV	42	976	976	321490	1	4d6	4d5 5s1, 4d5 5p1, 4d4 5s2, 4d5 5d1, 4d5 6s1, 4d5 6p1
46	Pd	I	8.336839	150	114	5098	2	4d10	4d9 5s1, 4d8 5s2, 4d9 5p1, 4d9 6s1, 4d8 5s1 5p1, 4d9 6p1, 4d9 5d1
		II	19.43	423	402	59830	1	4d9	4d8 5s1, 4d8 5p1, 4d7 5s2, 4d7 5s1 5p1, 4d8 6s1, 4d8 5d1, 4d8 6p1
		III	32.93	555	548	104876	1	4d8	4d7 5s1, 4d7 5p1, 4d7 6s1, 4d6 5s1 5p1
		IV	46	781	781	211678	1	4d7	4d6 5s1, 4d6 5p1, 4d6 5d1, 4d6 6s1, 4d6 6p1
47	Ag	I	7.576234	18	18	146	3	4d10 5s1	4d10 5p1, 4d9 5s2, 4d10 6s1, 4d10 6p1, 4d10 5d1, 4d10 7s1, 4d10 7p1, 4d10 6d1, 4d10 4f1, 4d10 8s1
		II	21.4844	150	143	7956	1	4d10	4d9 5s1, 4d9 5p1, 4d8 5s2, 4d9 6s1, 4d9 5d1, 4d8 5s1 5p1, 4d9 6p1
		III	34.8	210	210	17001	1	4d9	4d8 5s1, 4d8 5p1, 4d7 5s2, 4d8 6s1, 4d8 5d1, 4d8 6p1
		IV	49	507	507	90263	1	4d8	4d7 5s1, 4d7 5p1, 4d6 5s2, 4d7 6s1, 4d7 5d1, 4d7 6p1
48	Cd	I	8.99382	29	29	348	1	4d10 5s2	4d10 5s1 5p1, 4d10 5s1 6s1, 4d10 5s1 6p1, 4d10 5s1 5d1, 4d10 5s1 7s1, 4d10 5s1 7p1, 4d10 5s1 6d1, 4d10 5s1 4f1
		II	16.908313	40	34	505	1	4d10 5s1	4d10 5p1, 4d9 5s2, 4d10 6s1, 4d10 5d1, 4d10 6p1, 4d9 5s1 5p1, 4d10 7s1, 4d10 4f1, 4d10 6d1, 4d10 7p1
		III	37.468	48	48	926	1	4d10	4d9 5s1, 4d9 5p1, 4d8 5s2, 4d9 5d1, 4d9 6s1
		IV	51	165	165	10423	1	4d9	4d8 5s1, 4d8 5p1, 4d7 5s2, 4d8 5d1, 4d8 6s1
49	In	I	5.7863556	22	17	130	1	4d10 5s2 5p1	4d10 5s2 6s1, 4d10 5s2 6p1, 4d10 5s2 5d1, 4d10 5s1 5p2, 4d10 5s2 7s1, 4d10 5s2 7p1, 4d10 5s2 6d1, 4d10 5s2 4f1
		II	18.87041	34	34	477	1	4d10 5s2	4d10 5s1 5p1, 4d10 5s1 6s1, 4d10 5s1 5d1, 4d10 5p2, 4d10 5s1 6p1, 4d10 5s1 7s1, 4d10 5s1 4f1, 4d10 5s1 6d1, 4d10 5s1 7p1
		III	28.04415	35	35	536	1	4d10 5s1	4d10 5p1, 4d9 5s2, 4d10 6s1, 4d10 5d1, 4d10 6p1, 4d9 5s1 5p1, 4d10 4f1
		IV	55.45	48	48	926	1	4d10	4d9 5s1, 4d9 5p1, 4d8 5s2, 4d9 5d1, 4d9 6s1
50	Sn	I	7.343918	95	86	3123	1	4d10 5s2 5p2	4d10 5s2 5p1 6s1, 4d10 5s1 5p3, 4d10 5s2 5p1 6p1, 4d10 5s2 5p1 5d1, 4d10 5s2 5p1 7s1, 4d10 5s2 5p1 7p1, 4d10 5s2 5p1 6d1, 4d10 5s2 5p1 4f1, 4d10 5s2 5p1 8s1, 4d10 5s2 5p1 7d1
		II	14.63307	25	25	282	1	4d10 5s2 5p1	4d10 5s1 5p2, 4d10 5s2 6s1, 4d10 5s2 5d1, 4d10 5s2 6p1, 4d10 5s2 7s1, 4d10 5s2 4f1, 4d10 5s2 6d1, 4d10 5s2 7p1, 4d10 5s2 8s1, 4d10 5s2 5f1
		III	30.506	34	34	477	1	4d10 5s2	4d10 5s1 5p1, 4d10 5p2, 4d10 5s1 6s1, 4d10 5s1 5d1, 4d10 5s1 6p1, 4d10 4f1 5s1, 4d10 5s1 7s1, 4d10 5s1 6d1, 4d10 5s1 7p1
		IV	40.74	40	40	682	1	4d10 5s1	4d10 5p1, 4d10 5d1, 4d9 5s2, 4d10 6s1, 4d10 6p1, 4d10 4f1, 4d10 6d1, 4d10 7s1, 4d10 5g1, 4d9 5s1 5p1
51	Sb	I	8.608389	206	114	5865	1	5s2 5p3	5s2 5p2 6s1, 5s2 5p2 6p1, 5s2 5p2 5d1, 5s2 5p2 7s1, 5s2 5p2 6d1, 5s2 5p2 7p1, 5s2 5p2 4f1, 5s2 5p2 8s1, 5s2 5p2 8p1, 5s2 5p2 7d1
		II	16.626	74	69	2006	1	5s2 5p2	5s1 5p3, 5s2 5p1 6s1, 5s2 5p1 5d1, 5s2 5p1 6p1, 5s2 5p1 7s1, 5s2 5p1 6d1, 5s2 5p1 4f1, 5p4
		III	25.3235	21	21	202	1	5s2 5p1	5s1 5p2, 5s2 6s1, 5s2 5d1, 5s2 6p1, 5s2 4f1, 5s2 7s1, 5s2 6d1, 5s2 8s1
		IV	43.804	30	30	365	1	5s2	5s1 5p1, 5p2, 5s1 5d1, 5s1 6s1, 5s1 6p1, 5s1 4f1, 5s1 6d1, 5s1 7s1
52	Te	I	9.00966	245	99	4077	1	5s2 5p4	5s2 5p3 6s1, 5s2 5p3 6p1, 5s2 5p3 5d1, 5s2 5p3 7s1, 5s2 5p3 7p1, 5s2 5p3 6d1, 5s2 5p3 4f1, 5s2 5p3 8s1, 5s2 5p3 7d1
		II	18.6	165	158	10651	1	5s2 5p3	5s1 5p4, 5s2 5p2 6s1, 5s2 5p2 5d1, 5s2 5p2 6p1, 5s2 5p2 7s1, 5s2 5p2 6d1, 5s2 5p2 4f1, 5s2 5p2 7p1, 5s2 5p2 8s1
		III	27.84	57	57	1432	1	5s2 5p2	5s1 5p3, 5s2 5p1 5d1, 5s2 5p1 6s1, 5s2 5p1 6p1, 5s2 5p1 6d1, 5s2 5p1 7s1
		IV	37.4155	18	18	153	1	5s2 5p1	5s1 5p2, 5s2 5d1, 5s2 6s1, 5s2 6p1, 5s2 6d1, 5s2 7s1

Table C1 – *continued*

Z	El	Sp	E_i^{NIST} (eV)	n_{lev}	n_{lev}^{red}	n_{trans}	n_{opt}^{cfg}	Ground conf.	Additional configurations
53	I	I	10.45126	203	141	8605	1	5s2 5p5	5s2 5p4 6s1, 5s2 5p4 6p1, 5s2 5p4 5d1, 5s2 5p4 7s1, 5s2 5p4 7p1, 5s2 5p4 6d1, 5s2 5p4 4f1, 5s2 5p4 8s1, 5s2 5p4 8p1, 5s2 5p4 7d1
		II	19.13126	289	247	24237	1	5s2 5p4	5s2 5p3 6s1, 5s1 5p5, 5s2 5p3 5d1, 5s2 5p3 6p1, 5s2 5p3 7s1, 5s2 5p3 6d1, 5s2 5p3 4f1, 5s2 5p3 7p1, 5s2 5p3 8s1, 5s2 5p3 7d1, 5s2 5p3 5f1
		III	29.57	121	121	6438	1	5s2 5p3	5s1 5p4, 5s2 5p2 5d1, 5s2 5p2 6s1, 5s2 5p2 7s1, 5s2 5p2 6d1, 5s2 5p2 8s1, 5s2 5p2 7d1
		IV	40.357	63	63	1740	1	5s2 5p2	5s1 5p3, 5s2 5p1 5d1, 5s2 5p1 6s1, 5s2 5p1 6d1, 5s2 5p1 7s1, 5s2 5p1 7d1, 5s2 5p1 8s1
54	Xe	I	12.1298436	81	70	2043	1	5s2 5p6	5s2 5p5 6s1, 5s2 5p5 6p1, 5s2 5p5 5d1, 5s2 5p5 7s1, 5s2 5p5 7p1, 5s2 5p5 6d1, 5s2 5p5 8s1, 5s2 5p5 4f1, 5s2 5p5 7d1
		II	20.975	155	148	9251	1	5s2 5p5	5s1 5p6, 5s2 5p4 6s1, 5s2 5p4 5d1, 5s2 5p4 6p1, 5s2 5p4 7s1, 5s2 5p4 6d1, 5s2 5p4 4f1, 5s2 5p4 7p1, 5s2 5p4 8s1
		III	31.05	214	213	17769	1	5s2 5p4	5s1 5p5, 5s2 5p3 5d1, 5s2 5p3 6s1, 5s2 5p3 6p1, 5s2 5p3 4f1, 5s2 5p3 6d1, 5s2 5p3 7s1, 5s2 5p3 5f1, 5p6
		IV	42.2	100	100	4148	1	5s2 5p3	5s1 5p4, 5s2 5p2 5d1, 5s2 5p2 6s1, 5s2 5p2 4f1, 5s2 5p2 6p1
55	Cs	I	3.893905695	17	17	130	1	5s2 5p6 6s1	5s2 5p6 6p1, 5s2 5p6 5d1, 5s2 5p6 7s1, 5s2 5p6 7p1, 5s2 5p6 6d1, 5s2 5p6 8s1, 5s2 5p6 4f1, 5s2 5p6 8p1, 5s2 5p6 7d1
		II	23.15745	103	103	4393	1	5s2 5p6	5s2 5p5 6s1, 5s2 5p5 5d1, 5s2 5p5 6p1, 5s2 5p5 7s1, 5s2 5p5 6d1, 5s2 5p5 4f1, 5s2 5p5 7p1, 5s2 5p5 8s1, 5s2 5p5 5f1, 5s2 5p5 7d1, 5s2 5p5 8p1
		III	33.195	185	184	13980	1	5s2 5p5	5s1 5p6, 5s2 5p4 5d1, 5s2 5p4 6s1, 5s2 5p4 6p1, 5s2 5p4 4f1, 5s2 5p4 6d1, 5s2 5p4 7s1, 5s2 5p4 7p1, 5s2 5p4 5f1, 5s2 5p4 8s1
		IV	43	153	153	9720	1	5s2 5p4	5s1 5p5, 5s2 5p3 5d1, 5s2 5p3 6s1, 5s2 5p3 6d1, 5s2 5p3 7s1, 5s2 5p3 7d1, 5s2 5p3 8s1
56	Ba	I	5.2116646	59	58	1431	1	5s2 5p6 6s2	5s2 5p6 6s1 5d1, 5s2 5p6 6s1 6p1, 5s2 5p6 5d2, 5s2 5p6 5d1 6p1, 5s2 5p6 6s1 7s1, 5s2 5p6 6s1 6d1, 5s2 5p6 6s1 7p1, 5s2 5p6 5d1 7s1, 5s2 5p6 6s1 8s1, 5s2 5p6 6p2, 5s2 5p6 6s1 4f1, 5s2 5p6 6s1 7d1
		II	10.003826	19	19	159	1	5s2 5p6 6s1	5s2 5p6 5d1, 5s2 5p6 6p1, 5s2 5p6 7s1, 5s2 5p6 6d1, 5s2 5p6 4f1, 5s2 5p6 7p1, 5s2 5p6 5f1, 5s2 5p6 8s1, 5s2 5p6 7d1, 5s2 5p6 8p1
		III	35.8438	93	93	3564	1	5s2 5p6	5s2 5p5 5d1, 5s2 5p5 6s1, 5s2 5p5 4f1, 5s2 5p5 6p1, 5s2 5p5 6d1, 5s2 5p5 7s1, 5s2 5p5 5f1, 5s2 5p5 7p1, 5s2 5p5 7d1, 5s2 5p5 8s1
		IV	47	60	60	1586	1	5s2 5p5	5s1 5p6, 5s2 5p4 5d1, 5s2 5p4 6s1, 5s2 5p4 6p1
57	La	I	5.5769	414	286	31674	1	5p6 5d1 6s2	5p6 5d2 6s1, 5p6 5d3, 5p6 5d1 6s1 6p1, 5p6 4f1 6s2, 5p6 6s2 6p1, 5p6 5d2 6p1, 5p6 4f1 5d1 6s1, 5p6 4f1 6s1 6p1, 5p6 5d2 7s1, 5p6 5d1 6s1 7s1, 5p6 5d2 6d1, 5p6 5d2 7p1, 5p6 4f1 5d2, 5p6 5d1 6s1 7p1, 5p6 6s2 8p1
		II	11.18496	66	66	1663	2	5p6 5d2	5p6 5d1 6s1, 5p6 4f1 6s1, 5p6 4f1 5d1, 5p6 6s2, 5p6 5d1 6p1, 5p6 6s1 6p1, 5p6 4f1 6p1
		III	19.1773	15	15	95	2	5p6 5d1	5p6 4f1, 5p6 6s1, 5p6 6p1, 5p6 7s1, 5p6 6d1, 5p6 5f1, 5p6 7p1, 5p6 8s1
		IV	49.95	55	55	1239	1	5p6	5p5 4f1, 5p5 5d1, 5p5 6s1, 5p5 6p1, 5p5 6d1, 5p5 7s1
58	Ce	I	5.5386	1920	1236	478223	1	5p6 4f1 5d1 6s2	5p6 4f1 5d2 6s1, 5p6 4f2 6s2, 5p6 4f2 5d1 6s1, 5p6 4f1 5d1 6s1 6p1, 5p6 4f1 5d3, 5p6 4f1 6s2 6p1, 5p6 4f2 6s1 6p1, 5p6 4f1 5d2 6p1, 5p6 4f2 5d2
		II	10.956	459	459	69999	2	5p6 5d2 4f1	5p6 4f1 5d1 6s1, 5p6 4f2 6s1, 5p6 4f2 5d1, 5p6 4f1 6s2, 5p6 4f1 5d1 6p1, 5p6 4f2 6p1, 5p6 4f1 6s1 6p1
		III	20.1974	237	235	18710	1	5p6 4f2	5p6 4f1 5d1, 5p6 4f1 6s1, 5p6 5d2, 5p6 4f1 6p1, 5p6 5d1 6s1, 5p6 4f1 6d1, 5p6 4f1 7s1, 5p6 5d1 6p1, 5p6 5d2, 5p6 4f1 7p1, 5p6 4f1 8s1, 5p6 4f1 7d1, 5p6 4f1 6f1, 5p6 4f1 5g1, 5p6 6p2, 5p6 5d1 6d1
		IV	36.906	10	10	42	1	5p6 4f1	5p6 5d1, 5p6 6s1, 5p6 6p1, 5p6 6d1, 5p6 7s1
59	Pr	I	5.4702	6516	3396	3237939	5	4f3 6s2	4f3 6s1 5d1, 4f3 6s1 6p1, 4f3 6s1 7s1, 4f3 6s1 8s1, 4f2 6s2 5d1, 4f2 6s2 6p1, 4f2 5d2 6s1, 4f2 5d2 6p1, 4f2 5d1 6s1 6p1
		II	10.631	2007	1983	1121572	1	4f3 6s1	4f3 5d1, 4f2 5d2, 4f2 5d1 6s1, 4f3 6p1, 4f2 5d1 6p1
		III	21.6237	653	653	131500	1	4f3	4f2 5d1, 4f2 6s1, 4f2 6p1, 4f1 5d2, 4f1 5d1 6s1, 4f2 7s1, 4f2 6d1, 4f2 5f1, 4f2 8s1
		IV	38.981	90	90	2941	1	4f2	4f1 5d1, 4f1 6s1, 4f1 6p1, 5d2, 4f1 6d1, 5d1 6p1
60	Nd	I	5.525	12215	3405	2932375	5	4f4 6s2	4f4 6s1 5d1, 4f4 6s1 6p1, 4f4 6s1 7s1, 4f4 6s1 8s1, 4f3 5d1 6s2, 4f3 5d2 6s1, 4f3 5d1 6s1 6p1
		II	10.783	6888	6052	9633647	1	4f4 6s1	4f4 5d1, 4f3 5d2, 4f3 5d1 6s1, 4f4 6p1, 4f3 5d1 6p1, 4f3 6s1 6p1
		III	22.09	2252	2185	1363594	1	4f4	4f3 5d1, 4f3 6s1, 4f3 6p1, 4f2 5d2, 4f2 5d1 6s1, 4f2 5d1 6p1, 4f2 6s1 6p1
		IV	40.6	474	474	72924	1	4f3	4f2 5d1, 4f2 6s1, 4f2 6p1, 4f1 5d2, 4f1 5d1 6s1, 4f1 5d1 6p1
61	Pm	I	5.577	16294	2870	1913953	1	4f5 6s2	4f5 6s1 5d1, 4f5 6s1 6p1, 4f5 6s1 7s1, 4f4 6s2 5d1, 4f4 6s1 5d2
		II	10.938	12372	7697	14408362	1	4f5 6s1	4f5 5d1, 4f5 6p1, 4f4 6s1 6p1, 4f4 6s1 5d1, 4f4 5d1 6p1
		III	22.44	1994	1992	1044907	1	4f5	4f4 5d1, 4f4 6s1, 4f4 6p1
		IV	41.17	817	817	185068	1	4f4	4f3 5d1, 4f3 6s1, 4f3 6p1
62	Sm	I	5.64371	28221	1821	757867	2	4f6 6s2	4f6 6s1 5d1, 4f6 6s1 6p1, 4f6 6s1 7s1, 4f5 5d1 6s2, 4f5 5d2 6s1
		II	11.078	9030	3793	3418712	2	4f6 6s1	4f7, 4f6 5d1, 4f6 6p1, 4f5 5d1 6s1
		III	23.55	3737	3717	3441421	1	4f6	4f5 5d1, 4f5 6s1, 4f5 6p1
		IV	41.64	1994	1994	1046409	1	4f5	4f4 5d1, 4f4 6s1, 4f4 6p1
63	Eu	I	5.670385	103229	519	79073	1	4f7 6s2	4f7 5d1 6s1, 4f7 6s1 6p1, 4f6 5d1 6s2, 4f7 5d1 6p1, 4f7 6s1 7s1, 4f6 5d2 6s1, 4f7 5d2, 4f7 6s1 7p1, 4f7 6s1 6d1, 4f7 6s1 8s1, 4f7 6s1 5f1, 4f7 6s1 8p1, 4f7 6s1 7d1, 4f7 6p2
		II	11.24	22973	4379	4350550	1	4f7 6s1	4f7 5d1, 4f7 6p1, 4f6 5d1 6s1, 4f6 5d2
		III	24.84	5323	5245	6757496	1	4f7	4f6 5d1, 4f6 6s1, 4f6 6p1
		IV	42.94	3737	3737	3481004	1	4f6	4f5 5d1, 4f5 6s1, 4f5 6p1
64	Gd	I	6.1498	103013	553	84153	1	4f7 5d1 6s2	4f7 5d2 6s1, 4f8 6s2, 4f7 6s2 6p1, 4f7 5d1 6s1 6p1, 4f7 5d3
		II	12.076	46733	9207	18705963	3	4f7 5d1 6s1	4f7 6s2, 4f7 5d2, 4f8 6s1, 4f8 5d1, 4f7 6s1 6p1, 4f7 5d1 6p1, 4f8 6p1
		III	20.54	6637	4976	5864629	1	4f7 5d1	4f8, 4f7 6s1, 4f7 6p1, 4f7 7s1
		IV	44.44	5323	5317	6959526	1	4f7	4f6 5d1, 4f6 6s1, 4f6 6p1
65	Tb	I	5.8638	65817	3984	3778522	1	4f9 6s2	4f8 5d1 6s2, 4f8 5d2 6s1, 4f8 6s2 6p1, 4f9 6s1 6p1, 4f8 5d1 6s1 6p1, 4f9 5d1 6s1
		II	11.513	19854	11561	29940347	1	4f9 6s1	4f8 5d1 6s1, 4f8 6s2, 4f8 5d2, 4f9 5d1
		III	21.82	5194	4995	6119561	1	4f9	4f8 5d1, 4f8 6s1, 4f8 6p1
		IV	39.33	5983	5951	8562557	1	4f8	4f7 5d1, 4f7 6s1, 4f7 6p1
66	Dy	I	5.93905	44669	2627	1690259	1	4f10 6s2	4f9 5d1 6s2, 4f10 6s1 6p1, 4f10 5d1 6s1, 4f9 5d2 6s1, 4f9 6s2 6p1, 4f9 5d1 6s1 6p1, 4f10 6s1 7s1
		II	11.647	16034	11034	28683287	2	4f10 6s1	4f10 5d1, 4f9 5d1 6s1, 4f9 6s2, 4f9 5d2, 4f10 6p1, 4f9 6s1 6p1

Table C1 – *continued*

Z	El	Sp	E_i^{NIST} (eV)	n_{lev}	n_{lev}^{red}	n_{trans}	n_{opt}^{cfg}	Ground conf.	Additional configurations
		III	22.89	3549	3510	3073722	1	4f10	4f9 5d1, 4f9 6s1, 4f9 6p1
		IV	41.23	5194	5188	6628942	1	4f9	4f8 5d1, 4f8 6s1, 4f8 6p1
67	Ho	I	6.0215	23182	1425	512211	1	4f11 6s2	4f10 5d1 6s2, 4f11 6s1 6p1, 4f10 6s2 6p1, 4f11 5d1 6s1, 4f10 5d2 6s1, 4f10 5d1 6s1 6p1, 4f11 6s1 7s1, 4f11 6s1 7p1
		II	11.781	9640	6379	10019305	2	4f11 6s1	4f11 5d1, 4f11 6p1, 4f10 6s1 6p1, 4f10 6s1 5d1, 4f10 5d1 6p1
		III	22.79	1837	1826	880639	1	4f11	4f10 5d1, 4f10 6s1, 4f10 6p1
		IV	42.52	3549	3549	3146149	1	4f10	4f9 5d1, 4f9 6s1, 4f9 6p1
68	Er	I	6.1077	1303	516	83524	5	4f12 6s2	4f12 6s1 6p1, 4f12 6s1 7s1, 4f12 6s1 6d1, 4f12 6s1 8s1, 4f11 5d1 6s2, 4f11 6s2 6p1, 4f12 5d1 6s1
		II	11.916	5333	4565	5519756	2	6s1 4f12	4f12 6p1, 4f12 5d1, 4f11 6s2, 4f11 5d1 6s1, 4f11 5d2, 4f11 6s1 6p1, 4f11 5d1 6p1
		III	22.7	723	723	145774	1	4f12	4f11 5d1, 4f11 6s1, 4f11 6p1
		IV	42.42	1837	1837	890171	1	4f11	4f10 6s1, 4f10 6p1, 4f10 5d1
69	Tm	I	6.18431	1716	302	34629	5	4f13 6s2	4f13 6s1 6p1, 4f13 5d1 6s1, 4f13 6s1 7s1, 4f13 6s1 8s1, 4f12 5d1 6s2, 4f12 6s2 6p1, 4f13 6s1 7p1, 4f13 5d1 6p1, 4f13 6s1 6d1, 4f12 5d1 6s1 6p1, 4f13 6p2, 4f13 6s1 8p1
		II	12.065	1484	1399	573865	2	4f13 6s1	4f12 6s2, 4f13 5d1, 4f13 6p1, 4f12 5d1 6s1, 4f12 5d2, 4f12 6s1 6p1, 4f12 5d1 6p1
		III	23.66	3666	2474	1639827	1	4f13	4f12 5d1, 4f12 6s1, 4f12 6p1, 4f11 5d1 6s1, 4f11 5d1 6p1, 4f11 6s1 6p1
		IV	42.41	723	723	145774	1	4f12	4f11 5d1, 4f11 6s1, 4f11 6p1
70	Yb	I	6.25416	446	26	290	5	4f14 6s2	4f14 6s1 6p1, 4f14 6s1 5d1, 4f14 6s1 7s1, 4f14 6s1 6d1, 4f14 6s1 7p1, 4f14 6s1 8s1, 4f13 6s2 5d1, 4f13 6s2 6p1, 4f13 6s1 5d2, 4f13 5d1 6s1 6p1, 4f14 6p2
		II	12.179185	265	262	23892	2	4f14 6s1	4f13 6s2, 4f14 5d1, 4f14 6p1, 4f14 7s1, 4f13 5d1 6s1, 4f13 5d2, 4f13 6s1 6p1, 4f13 5d1 6p1
		III	25.053	1039	788	187828	1	4f14	4f13 5d1, 4f13 6s1, 4f13 6p1, 4f13 7s1, 4f13 6d1, 4f12 5d1 6s1, 4f12 5d1 6p1, 4f12 6s1 6p1
		IV	43.61	202	202	12679	1	4f13	4f12 5d1, 4f12 6s1, 4f12 6p1
71	Lu	I	5.425871	61	58	1467	1	4f14 5d1 6s2	4f14 6s2 6p1, 4f14 5d1 6s1 6p1, 4f14 5d2 6s1, 4f14 6s2 7s1, 4f14 6s2 6d1, 4f14 6s2 8s1, 4f14 6s2 7p1, 4f14 6s1 6p2, 4f14 6s2 5f1, 4f14 6s2 7d1
		II	14.13	58	58	1365	1	4f14 6s2	4f14 5d1 6s1, 4f14 6s1 6p1, 4f14 5d2, 4f14 5d1 6p1, 4f14 6s1 7s1, 4f14 6s1 6d1, 4f14 5d1 7s1, 4f14 5d1 6d1
		III	20.9594	184	111	4146	1	4f14 6s1	4f14 5d1, 4f14 6p1, 4f14 7s1, 4f14 6d1, 4f13 5d1 6s1, 4f13 5d1 6p1, 4f13 6s1 6p1
		IV	45.249	61	61	1410	1	4f14	4f13 5d1, 4f13 6s1, 4f13 6p1, 4f13 6d1, 4f13 7s1
72	Hf	I	6.82507	313	222	17682	1	4f14 5d2 6s2	4f14 5d2 6s1 6p1, 4f14 5d3 6s1, 4f14 5d4, 4f14 5d3 6p1, 4f14 5d2 6s1 7s1
		II	14.61	129	129	6811	1	4f14 5d1 6s2	4f14 5d2 6s1, 4f14 5d3, 4f14 5d1 6s1 6p1, 4f14 5d2 6p1, 4f14 5d2 7s1, 4f14 5d1 6s1 7s1
		III	22.55	64	64	1680	1	4f14 5d2	4f14 5d1 6s1, 4f14 6s2, 4f14 5d1 6p1, 4f14 6s1 6p1, 4f14 5d1 6d1, 4f14 5d1 7s1, 4f14 5d1 7p1
		IV	33.37	14	14	87	1	4f14 5d1	4f14 6s1, 4f14 6p1, 4f14 6d1, 4f14 7s1, 4f14 5f1, 4f14 7p1, 4f14 7d1
73	Ta	I	7.549571	705	450	72410	2	5d3 6s2	5d5, 5d4 6s1, 5d3 6s1 6p1, 5d2 6s2 6p1, 5d4 6p1, 5d3 6s1 7s1, 5d3 6s1 8s1
		II	16.2	487	486	83641	3	5d3 6s1	5d2 6s2, 5d4, 5d3 6p1, 5d2 6s1 6p1, 5d3 7s1, 5d3 6d1
		III	23.1	188	188	13747	1	5d3	5d2 6s1, 5d2 6p1, 5d1 6s2, 5d1 6s1 6p1, 5d2 6d1, 5d2 7s1
		IV	35	52	52	1086	1	5d2	5d1 6s1, 5d1 6p1, 6s2, 6s1 6p1, 5d1 6d1, 5d1 7s1
74	W	I	7.86403	808	315	33704	1	5d4 6s2	5d5 6s1, 5d4 6s1 6p1, 5d5 6p1, 5d4 6s1 7s1
		II	16.37	851	814	231520	1	5d4 6s1	5d5, 5d3 6s2, 5d3 6s1 6p1, 5d4 6p1, 5d4 7s1, 5d4 6d1
		III	26	487	487	83833	1	5d4	5d3 6s1, 5d2 6s2, 5d3 6p1, 5d2 6s1 6p1, 5d3 7s1, 5d3 6d1
		IV	38.2	188	188	13747	1	5d3	5d2 6s1, 5d2 6p1, 5d1 6s2, 5d1 6s1 6p1, 5d2 7s1, 5d2 6d1
75	Re	I	7.83352	1875	501	87004	2	5d5 6s2	5d6 6s1, 5d5 6s1 6p1, 5d4 6s2 6p1, 5d5 6s1 7s1, 5d6 6p1, 5d5 6s1 6d1, 5d5 6s1 8s1, 5d4 6s2 7s1
		II	16.6	1122	860	246921	2	5d5 6s1	5d4 6s2, 5d5 6p1, 5d6, 5d4 6s1 6p1, 5d5 7s1, 5d5 6d1
		III	27	851	848	252095	1	5d5	5d4 6s1, 5d4 6p1, 5d3 6s1 6p1, 5d3 6s2, 5d4 7s1, 5d4 6d1
		IV	39.1	487	487	83833	1	5d4	5d3 6s1, 5d3 6p1, 5d2 6s2, 5d2 6s1 6p1, 5d3 7s1, 5d3 6d1
76	Os	I	8.43823	984	388	51476	1	5d6 6s2	5d7 6s1, 5d6 6s1 6p1, 5d6 6s1 7s1, 5d7 6p1, 5d7 7s1, 5d7 7p1, 5d7 6d1
		II	17	1435	960	316620	1	5d6 6s1	5d6 6p1, 5d7, 5d5 6s1 6p1, 5d6 7s1, 5d6 6d1, 5d5 6s1 7p1
		III	25	1088	1030	356508	1	5d6	5d5 6s1, 5d5 6p1, 5d4 6s1 6p1, 5d5 6d1, 5d5 7s1
		IV	41	851	851	253888	1	5d5	5d4 6s1, 5d4 6p1, 5d3 6s2, 5d3 6s1 6p1, 5d4 7s1, 5d4 6d1
77	Ir	I	8.96702	385	185	12521	2	5d7 6s2	5d9, 5d8 6s1, 5d7 6s1 6p1, 5d7 6s1 7s1, 5d8 6p1, 5d8 7s1
		II	17	699	580	115707	1	5d7 6s1	5d8, 5d6 6s2, 5d7 6p1, 5d6 6s1 6p1, 5d7 7s1, 5d7 7p1
		III	28	818	803	224115	1	5d7	5d6 6s1, 5d6 6p1, 5d5 6s2, 5d6 6d1, 5d6 7s1, 5d6 7p1
		IV	40	976	976	321490	1	5d6	5d5 6s1, 5d5 6p1, 5d4 6s2, 5d5 6d1, 5d5 7s1, 5d5 7p1
78	Pt	I	8.95883	152	110	4726	3	5d9 6s1	5d10, 5d9 6p1, 5d9 7s1, 5d8 6s2, 5d8 6s1 6p1, 5d8 6s1 7s1
		II	18.56	248	232	20285	1	5d9	5d8 6s1, 5d7 6s2, 5d8 6p1, 5d8 7s1, 5d8 6d1, 5d8 8s1, 5d8 7d1
		III	29	555	551	105890	1	5d8	5d7 6s1, 5d7 6p1, 5d7 7s1, 5d6 6s1 6p1
		IV	43	781	780	211123	1	5d7	5d6 6s1, 5d6 6p1, 5d6 6d1, 5d6 7s1, 5d6 7p1
79	Au	I	9.225554	36	33	472	1	5d10 6s1	5d9 6s2, 5d10 6p1, 5d9 6s1 6p1, 5d10 7s1, 5d10 7p1, 5d10 6d1, 5d10 8s1, 5d10 8p1
		II	20.203	60	60	1479	1	5d10	5d9 6s1, 5d8 6s2, 5d9 6p1, 5d9 7s1, 5d9 6d1, 5d9 7p1
		III	30	210	209	16830	1	5d9	5d8 6s1, 5d8 6p1, 5d7 6s2, 5d8 7s1, 5d8 6d1, 5d8 7p1
		IV	45	507	507	90263	1	5d8	5d7 6s1, 5d7 6p1, 5d6 6s2, 5d7 7s1, 5d7 6d1, 5d7 7p1
80	Hg	I	10.437504	41	31	404	1	5d10 6s2	5d10 6s1 6p1, 5d10 6s1 7s1, 5d9 6s2 6p1, 5d10 6s1 7p1, 5d10 6s1 6d1, 5d10 6s1 8s1, 5d10 6s1 8p1, 5d10 6s1 7d1, 5d10 6s1 5f1
		II	18.75687	38	38	637	1	5d10 6s1	5d9 6s2, 5d10 6p1, 5d9 6s1 6p1, 5d10 7s1, 5d10 6d1, 5d10 7p1, 5d10 8s1, 5d10 5f1, 5d10 7d1
		III	34.46	138	138	7316	1	5d10	5d9 6s1, 5d8 6s2, 5d9 6p1, 5d8 6s1 6p1, 5d9 7s1, 5d9 6d1
		IV	48.55	165	165	10423	1	5d9	5d8 6s1, 5d8 6p1, 5d7 6s2, 5d8 6d1, 5d8 7s1
81	Tl	I	6.1082873	12	12	66	3	5d10 6s2 6p1	5d10 6s2 7s1, 5d10 6s2 7p1, 5d10 6s2 6d1, 5d10 6s2 8s1, 5d10 6s2 8p1, 5d10 6s2 7d1
		II	20.4283	46	46	890	1	5d10 6s2	5d10 6s1 6p1, 5d10 6s1 7s1, 5d9 6s2 6p1, 5d10 6s1 6d1, 5d10 6p2, 5d10 6s1 7p1, 5d10 6s1 8s1, 5d10 6s1 5f1, 5d10 6s1 7d1, 5d10 6s1 8p1
		III	29.852	40	40	707	1	5d10 6s1	5d10 6p1, 5d9 6s2, 5d9 6s1 6p1, 5d10 7s1, 5d10 6d1, 5d10 7p1, 5d10 5f1, 5d10 8s1, 5d10 7d1, 5d10 8p1
		IV	51.14	43	43	773	1	5d10	5d9 6s1, 5d9 6p1, 5d9 6d1, 5d9 7s1, 5d9 8s1
82	Pb	I	7.4166799	95	41	730	6	5d10 6s2 6p2	5d10 6s2 6p1 7s1, 5d10 6s2 6p1 7p1, 5d10 6s2 6p1 6d1, 5d10 6s2 6p1 8s1, 5d10 6s2 6p1 8p1, 5d10 6s2 6p1 7d1, 5d10 6s2 6p1 5f1, 5d10 6s2 6p1 9s1, 5d10 6s2 6p1 9p1, 5d10 6s2 6p1 8d1
		II	15.032499	27	27	333	1	5d10 6s2 6p1	5d10 6s1 6p2, 5d10 6s2 7s1, 5d10 6s2 6d1, 5d10 6s2 7p1, 5d10 6s2 8s1, 5d10 6s2 5f1, 5d10 6s2 7d1, 5d10 6s2 8p1, 5d10 6s2 9s1, 5d10 6s2 6f1, 5d10 6s2 8d1

Table C1 – *continued*

Z	El	Sp	E_i^{NIST} (eV)	n_{lev}	n_{lev}^{red}	n_{trans}	n_{opt}^{cfg}	Ground conf.	Additional configurations
		III	31.9373	50	50	1039	1	5d10 6s2	5d10 6s1 6p1, 5d10 6p2, 5d10 6s1 7s1, 5d10 6s1 6d1, 5d9 6s2 6p1, 5d10 6s1 7p1, 5d10 6s1 5f1, 5d10 6s1 8s1, 5d10 6s1 7d1, 5d10 6s1 8p1, 5d10 6s1 6f1
		IV	42.33256	68	67	1956	1	5d10 6s1	5d10 6p1, 5d9 6s2, 5d9 6s1 6p1, 5d10 6d1, 5d10 7s1, 5d10 7p1, 5d10 5f1, 5d10 8s1, 5d10 7d1, 5d9 6p2, 5d10 8p1
83	Bi	I	7.285516	176	25	300	2	5d10 6s2 6p3	5d10 6s2 6p2 7s1, 5d10 6s2 6p2 7p1, 5d10 6s2 6p2 6d1, 5d10 6s2 6p2 8s1, 5d10 6s2 6p2 8p1, 5d10 6s2 6p2 7d1, 5d10 6s2 6p2 9s1, 5d10 6s2 6p2 9p1, 5d10 6s2 6p2 8d1
		II	16.703	107	85	3067	2	5d10 6s2 6p2	5d10 6s2 6p1 7s1, 5d10 6s1 6p3, 5d10 6s2 6p1 6d1, 5d10 6s2 6p1 7p1, 5d10 6s2 6p1 8s1, 5d10 6s2 6p1 5f1, 5d10 6s2 6p1 7d1, 5d10 6s2 6p1 8p1, 5d10 6s2 6p1 9s1, 5d10 6s2 6p1 6f1, 5d10 6s2 6p1 8d1
		III	25.563	24	24	260	1	5d10 6s2 6p1	5d10 6s1 6p2, 5d10 6s2 7s1, 5d10 6s2 6d1, 5d10 6s2 7p1, 5d10 6s2 5f1, 5d10 6s2 8s1, 5d10 6s2 7d1, 5d10 6s2 8p1, 5d10 6s2 6f1
		IV	45.37	42	42	737	1	5d10 6s2	5d10 6s1 6p1, 5d10 6p2, 5d10 6s1 6d1, 5d10 6s1 7s1, 5d9 6s2 6p1, 5d10 6s1 7p1, 5d10 6s1 5f1, 5d10 6s1 8s1, 5d10 6s1 7d1
84	Po	I	8.414	251	61	1614	5	6s2 6p4	6s2 6p3 7s1, 6s2 6p3 7p1, 6s2 6p3 6d1, 6s2 6p3 8s1, 6s2 6p3 8p1, 6s2 6p3 7d1, 6s2 6p3 9p1, 6s2 6p3 8d1, 6s2 6p3 10p1
		II	19.3	165	139	8209	1	6s2 6p3	6s1 6p4, 6s2 6p2 7s1, 6s2 6p2 6d1, 6s2 6p2 7p1, 6s2 6p2 8s1, 6s2 6p2 7d1, 6s2 6p2 5f1, 6s2 6p2 8p1, 6s2 6p2 9s1
		III	27.3	57	57	1432	1	6s2 6p2	6s1 6p3, 6s2 6p1 6d1, 6s2 6p1 7s1, 6s2 6p1 7p1, 6s2 6p1 7d1, 6s2 6p1 8s1
		IV	36	18	18	153	1	6s2 6p1	6s1 6p2, 6s2 6d1, 6s2 7s1, 6s2 7p1, 6s2 7d1, 6s2 8s1
85	At	I	9.31751	116	48	1000	1	6s2 6p5	6s2 6p4 7s1, 6s2 6p4 7p1, 6s2 6p4 6d1, 6s2 6p4 8s1, 6s2 6p4 8p1, 6s2 6p4 7d1
		II	17.88	289	138	7857	1	6s2 6p4	6s2 6p3 7s1, 6s1 6p5, 6s2 6p3 6d1, 6s2 6p3 7p1, 6s2 6p3 8s1, 6s2 6p3 7d1, 6s2 6p3 5f1, 6s2 6p3 8p1, 6s2 6p3 9s1, 6s2 6p3 8d1, 6s2 6p3 6f1
		III	26.58	121	93	3824	1	6s2 6p3	6s1 6p4, 6s2 6p2 6d1, 6s2 6p2 7s1, 6s2 6p2 8s1, 6s2 6p2 7d1, 6s2 6p2 9s1, 6s2 6p2 8d1
		IV	39.65	63	63	1740	1	6s2 6p2	6s1 6p3, 6s2 6p1 6d1, 6s2 6p1 7s1, 6s2 6p1 7d1, 6s2 6p1 8s1, 6s2 6p1 8d1, 6s2 6p1 9s1
86	Rn	I	10.7485	65	41	678	1	6s2 6p6	6s2 6p5 7s1, 6s2 6p5 7p1, 6s2 6p5 6d1, 6s2 6p5 8p1, 6s2 6p5 7d1, 6s2 6p5 9s1, 6s2 6p5 5f1
		II	21.4	155	144	8755	1	6s2 6p5	6s1 6p6, 6s2 6p4 7s1, 6s2 6p4 6d1, 6s2 6p4 7p1, 6s2 6p4 8s1, 6s2 6p4 7d1, 6s2 6p4 5f1, 6s2 6p4 8p1, 6s2 6p4 9s1
		III	29.4	214	193	14481	1	6s2 6p4	6s1 6p5, 6s2 6p3 6d1, 6s2 6p3 7s1, 6s2 6p3 7p1, 6s2 6p3 5f1, 6s2 6p3 7d1, 6s2 6p3 8s1, 6s2 6p3 6f1, 6p6
		IV	36.9	100	100	4148	1	6s2 6p3	6s1 6p4, 6s2 6p2 6d1, 6s2 6p2 7s1, 6s2 6p2 5f1, 6s2 6p2 7p1
87	Fr	I	4.072741	5	5	10	1	6s2 6p6 7s1	6s2 6p6 7p1, 6s2 6p6 6d1
		II	22.4	103	78	2484	1	6s2 6p6	6s2 6p5 7s1, 6s2 6p5 6d1, 6s2 6p5 7p1, 6s2 6p5 8s1, 6s2 6p5 7d1, 6s2 6p5 5f1, 6s2 6p5 8p1, 6s2 6p5 9s1, 6s2 6p5 6f1, 6s2 6p5 8d1, 6s2 6p5 9p1
		III	33.5	185	177	12894	1	6s2 6p5	6s1 6p6, 6s2 6p4 6d1, 6s2 6p4 7s1, 6s2 6p4 7p1, 6s2 6p4 5f1, 6s2 6p4 7d1, 6s2 6p4 8s1, 6s2 6p4 8p1, 6s2 6p4 6f1, 6s2 6p4 9s1
		IV	39.1	153	127	6626	1	6s2 6p4	6s1 6p5, 6s2 6p3 6d1, 6s2 6p3 7s1, 6s2 6p3 7d1, 6s2 6p3 8s1, 6s2 6p3 8d1, 6s2 6p3 9s1
88	Ra	I	5.2784239	26	23	221	1	6s2 6p6 7s2	6s2 6p6 7s1 7p1, 6s2 6p6 6d1 7s1, 6s2 6p6 6d1 7p1, 6s2 6p6 7p2
		II	10.14718	5	5	10	1	6s2 6p6 7s1	6s2 6p6 6d1, 6s2 6p6 7p1
		III	31	93	78	2487	1	6s2 6p6	6s2 6p5 6d1, 6s2 6p5 7s1, 6s2 6p5 5f1, 6s2 6p5 7p1, 6s2 6p5 7d1, 6s2 6p5 8s1, 6s2 6p5 6f1, 6s2 6p5 8p1, 6s2 6p5 8d1, 6s2 6p5 9s1
		IV	41	60	60	1586	1	6s2 6p5	6s1 6p6, 6s2 6p4 6d1, 6s2 6p4 7s1, 6s2 6p4 7p1
89	Ac	I	5.380226	170	112	4830	3	6p6 6d1 7s2	6p6 6d2 7s1, 6p6 6d1 7s1 7p1, 6p6 7s2 7p1, 6p6 6d2 7p1, 6p6 6d3, 6p6 5f1 6d1 7s1, 6p6 5f1 7s1 7p1
		II	11.75	68	68	1743	3	6p6 7s2	6p6 6d1 7s1, 6p6 6d2, 6p6 7s1 7p1, 6p6 6d1 7p1, 6p6 7s1 5f1, 6p6 6d1 5f1, 6p6 7s1 8s1, 6p6 5f1 7p1
		III	17.431	12	12	60	1	6p6 7s1	6p6 6d1, 6p6 5f1, 6p6 7p1, 6p6 8s1, 6p6 7d1, 6p6 6f1
		IV	44.8	55	55	1239	1	6p6	6p5 5f1, 6p5 6d1, 6p5 7s1, 6p5 7p1, 6p5 7d1, 6p5 8s1
90	Th	I	6.3067	822	590	114716	3	6p6 6d2 7s2	6p6 6d3 7s1, 6p6 5f1 6d2 7s1, 6p6 5f1 6d1 7s2, 6p6 6d1 7s2 7p1, 6p6 6d2 7s1 7p1, 6p6 5f1 7s2 7p1, 6p6 6d4, 6p6 5f1 6d1 7s1 7p1, 6p6 5f2 7s2, 6p6 5f1 6d3
		II	12.1	343	343	41678	7	6p6 6d1 7s2	6p6 6d2 7s1, 6p6 5f1 7s2, 6p6 5f1 6d1 7s1, 6p6 6d3, 6p6 5f1 6d2, 6p6 6d1 7s1 7p1, 6p6 5f2 7s1, 6p6 5f1 7s1 7p1, 6p6 5f1 6d1 7p1
		III	18.32	79	79	2269	1	6p6 5f1 6d1	6p6 6d2, 6p6 6d1 7s1, 6p6 7s2, 6p6 5f2, 6p6 5f1 7p1, 6p6 6d1 7p1, 6p6 7s1 7p1, 6p6 5f1 8s1
		IV	28.648	15	15	97	9	6p6 5f1	6p6 6d1, 6p6 7s1, 6p6 7p1, 6p6 7d1, 6p6 8s1, 6p6 6f1, 6p6 8d1, 6p6 9s1
91	Pa	I	5.89	6192	1990	1115150	3	5f2 6d1 7s2	5f3 7s2, 5f2 6d2 7s1, 5f3 6d1 7s1, 5f3 7s1 7p1, 5f2 6d1 7s1 7p1, 5f2 7s2 7p1, 5f2 6d2 7p1
		II	11.9	2020	2000	1141645	1	5f2 7s2	5f3 7s1, 5f3 6d1, 5f2 6d2, 5f2 6d1 7s1, 5f3 7p1, 5f2 6d1 7p1
		III	18.6	653	653	131500	1	5f2 6d1	5f3, 5f2 7s1, 5f2 7p1, 5f1 6d2, 5f1 6d1 7s1, 5f2 8s1, 5f2 7d1, 5f2 6f1, 5f2 9s1
		IV	30.9	90	90	2941	1	5f2	5f1 6d1, 5f1 7s1, 5f1 7p1, 6d2, 5f1 7d1, 6d1 7p1
92	U	I	6.19405	11383	2286	1315448	1	5f3 6d1 7s2	5f4 7s2, 5f4 7s1 6d1, 5f3 6d2 7s1, 5f4 7s1 7p1, 5f3 6d1 7s1 7p1
		II	11.6	6929	6101	9847373	1	5f3 7s2	5f4 7s1, 5f4 6d1, 5f3 6d2, 5f3 6d1 7s1, 5f4 7p1, 5f3 6d1 7p1, 5f3 7s1 7p1
		III	19.8	2252	2246	1441511	1	5f4	5f3 6d1, 5f3 7s1, 5f3 7p1, 5f2 6d2, 5f2 6d1 7s1, 5f2 6d1 7p1, 5f2 7s1 7p1
		IV	36.7	474	474	72924	1	5f3	5f2 6d1

This paper has been typeset from a TEX/LATEX file prepared by the author.